university of groningen

faculty of science and engineering

Comparison of Effectiveness of Various Roughness Elements for Coastal Dikes using ComFLOW.

Master Project Applied Mathematics
April 28, 2025

Student: Maria Ewelina Wasiljew
First Supervisor: Dr. Ir. Roel Luppes
Second Supervisor: Prof. Dr. Julian Koellermeier

Abstract

Floods are natural disasters that can cause tremendous destruction and loss of life. The risk of occurrence increases every year due to environmental changes, such as rising sea levels and more severe and unpredictable weather conditions. As such, coastal defense is crucial to ensure the safety of the population. Roughness elements are placed on dikes to absorb the wave energy and reduce the amount of overtopping. The efficiency of this component of the dike is studied through numerical simulations performed with ComFLOW, a software tool that has been developed at the University of Groningen to simulate complex fluid flow. With this tool, various characteristics of roughness elements are studied in order to improve the efficiency of the design. It is found that increasing the size of the elements and the height difference between them is beneficial. Further results suggest that to reduce the overtopping, roughness elements have to induce a high amount of turbulence in the flow, as well as redirect the trajectory of the wave. The first is attained by incorporating a 'free passage' into the design of the elements. To redirect the wave, a rounded incision is applied to the last block. The optimal roughness elements added on top of a smooth dike reduced the overtopping by a factor of 5. Furthermore, through the study of numerical errors, a suitable simulation setting is found, which ensures a high accuracy of the results while lowering the computational time. It can be concluded that ComFLOW is a satisfactory tool for simulations of coastal dynamics, incorporating wave collisions with various designs of roughness elements.

Contents

1 Introduction **3**

2 ComFLOW: mathematical and numerical model **5**
2.1 Governing equations 5
2.2 Cell labeling 6
2.3 Discretization 7
2.4 Numerical methods 8

3 Waves: explanation of parameters and mathematical theory **12**
3.1 Wave terminology and physical explanation 12
3.2 5th Order Stokes Wave theory 13
3.3 Choice of wave event 15

4 Dikes: common build, terminology **17**

5 Simulation setup **19**
5.1 Domain 19
5.2 Data gathering 22
5.3 Grid stretching and local refinement 22
5.4 Validation of the shorter domain and grid modifications 25

6 Simulations of roughness elements **33**
6.1 General design and strategy 33
6.2 Size of the block 34
6.3 Slope of upper part of the dike 39
6.4 Height difference between the blocks 42
6.5 Width of blocks 46
6.6 Distance between the blocks 51
6.7 Placement of the middle block 56
6.8 Relevance of first two blocks 61
6.9 First block 67
6.10 Last block 76

7 Observations of numerical errors **83**
7.1 Line of vertical droplets 83
7.2 Droplets acting as bullets 84

8 Discussion and conclusion **89**

1 Introduction

The term 'natural disaster' makes one think about very cinematic events such as tournedos, tsunamis or erupting volcanoes. However, when living in the Netherlands, these are not the main concerns due to geographic location. Instead, floods are a serious natural threat that can result in an equally frightful scenario.

A reminder of how devastating such events can be is the Great Flood of 1953, known in dutch as *Watersnoodramp* [21]. At the time of spring tide, when the water levels significantly increased, a severe storm hit the North Sea [11]. The combination of these two events resulted in a breach of coastal defenses in the province of Zeeland. As the first flood wave hit at night, many citizens did not receive the warning in time and as such did not manage to evacuate. They had to climb up onto the rooftops and other higher ground, and wait for the rescue from there [3]. A month later, an unforeseen second flood wave took place, as numerous dams broke, unable to sustain the large quantity of water. An example of the severity of this natural disaster can be seen in Figure 1, which depicts the flooded village of Rilland. The total casualties reached 1836 people, 43000 houses drowned, and 150 000 hectares of farmland were destroyed [21].

Figure 1: Image of the flooded village Rilland as a result of the Great Flood of 1953, adopted from [23].

The importance of coastal defense in the Netherlands is further emphasized by the landscape of the country. Not only is 26% of the land below sea level, but it is 59% of the territory that is prone to floods. Furthermore, it is estimated that 70% of the Dutch population resides in those areas. Due to the growth of urban and rural areas, if a tragedy similar to the Great Flood of 1953 happened today, the fatalities would be much greater [2].

Each year the risk of floods increases due to environmental changes. One of the key factors is the rising sea level, with the average annual rise of 2.9 millimeters each year [8]. Additionally, severe weather conditions, such as strong winds and rainfall, are becoming more frequent and less predictable [1] [14]. As such, to ensure the safety of people in the future, it is crucial to further research and improve the coastal defenses.

For that reason, in this thesis the design of dikes is studied, which are the most common choice for coastal defense in the Netherlands [18]. To concise the area of research, the main focus lies in roughness elements. These are structures added on the slope of the dike, that are meant to dissipate wave energy and reduce the amount of water getting over the dike, which is referred to as overtopping. The main goal of this thesis is to find realistic designs and characteristics of such elements, that minimize the amount of overtopping.

Real life experimentation of coastal dike designs tends to be expensive and time consuming. As such, for this project the alternative approach is considered, namely that of conducting a series of numerical simulations. The software used is ComFLOW, which was developed at the University of Groningen. This tool allows for a variety of methods to be used to model and simulate fluid flow. Throughout the research the optimal settings for simulations of coastal dikes are to be found. Thus, the additional goal of the thesis is to determine whether ComFLOW is a suitable tool for simulations of coastal dikes. The possible areas for further improvement of the software are to be identified and discussed.

An important source of information for this project is *EurOtop Manual* [18]. It includes vast information on wave overtopping of coastal defenses. The manual includes data and research from around the world, as well as recordings of previous real life experiments. The motivation behind this work is to assist governments and other institutes of interest in reducing flood risk. This manual is considered a part of standard literature for those in coastal engineering. For this project, it has been used as a general source of information on various aspects of coastal dikes.

2 ComFLOW: mathematical and numerical model

In this research, the efficiency of different roughness elements on dikes has been studied through numerical simulations of fluid flow. The program used for this purpose is ComFLOW, which has been developed at the University of Groningen. Originally, the purpose of this software was to model the sloshing of liquid fuel in spacecraft. However, with time it has been enhanced further by inclusion of green water dynamics. Currently, ComFLOW can be used for simulations of complex free-surface flows. For the visualization of pre- and post processing data the MATLAB software is used [16].

In this section, the mathematical and numerical methods used for simulations are introduced. As the ComFLOW software allows for a variety of options regarding the methods used, only the ones applied in this project are discussed along the reasoning for the choice.

2.1 Governing equations

The fluid flow dynamics is described with the Navier-Stokes equations, through the conservation of mass and momentum. For this project, we consider water as an incompressible and viscous fluid, which simplifies the original equations [16].

Consider an arbitrary two dimensional domain Ω, with a domain boundary $\partial\Omega$. Let $\mathbf{u} = (u, w)$ denote the velocity vector. Then the conservation of mass is described as

$$\nabla \cdot \mathbf{u} = 0.$$

Similarly, the conservation of momentum can be written as

$$\frac{\partial \mathbf{u}}{\partial t} + \mathbf{u} \cdot \nabla \mathbf{u} = -\frac{1}{\rho}\nabla p + \frac{\mu}{\rho}\nabla \cdot \nabla \mathbf{u} + \mathbf{F},$$

where t stands for time, p is pressure, μ is dynamic viscosity, ρ stands for density and $\mathbf{F}$ denotes an external force (such as gravity).

At solid boundaries of the domain and objects within it, we require that the water cannot pass through them, due to the impenetrability of the material. Additionally, we imply the no-slip condition, which can be understood as the fluid 'sticking' to the walls due to the viscosity.
Both of these conditions, at solid boundaries, can be described as

$$\mathbf{u} = 0.$$

Furthermore, at the inflow and outflow the generating and absorbing boundary conditions (GABC) are used. This is a computationally efficient method of preventing any reflection of waves from the boundaries of the domain [5]. At the inflow the GABC is combined with a prescription of an incoming wave. The wave model used for that purpose is the 5th order Stokes theory, which is discussed in Subsection 3.2.

For this project, the free surface refers to the water that is in contact with the atmosphere. Let us assume that the position of the free surface is $s(\bar{x}, t) = 0$. Then, the dynamic of its displacement is described as

$$\frac{Ds}{Dt} = \frac{\partial s}{\partial t} + (\mathbf{u} \cdot \nabla)s = 0.$$

The boundary conditions for the pressure and the velocity at the free surface are given as

$$-p + 2\mu\frac{\partial u_n}{\partial n} = -p_0 + 2\sigma H,$$

$$\mu\Big(\frac{\partial u_n}{\partial t} + \frac{\partial u_t}{\partial n}\Big) = 0,$$

where u_n and u_t are the normal and tangential components of the velocity respectively, p_0 denotes the atmospheric pressure, σ denotes the surface tension and $2H$ is the total curvature.

The force exerted by the fluid on an object consists of pressure force and shear force. In ComFLOW the shear force is neglected, due to its small scale [16]. As such, the fluid force on the boundary of an object is

$$F_p = \int_S p\bar{n}dS.$$

This concludes the introduction of the governing equations. The mathematical model of wave dynamics used to describe the incoming wave at the inflow is given in Section 3.2.

2.2 Cell labeling

The domain Ω is covered with staggered Cartesian variables. This grid setting implies that the pressure is defined in the center of the computational cell, while velocity components are located on the middle of grid cell faces. [22].

As the grid covers the entire domain, the cells have to be labeled to create a distinction between the fluid, atmosphere and solid objects. ComFLOW uses the edge and volume apertures to determine in which part of the grid fluid flow is possible. With this, the geometry of the cell is set as fluid, solid boundary, or air. Additionally, at every time step the cells open to flow are given additional free-surface labels, which are fluid (F), surface (S) and empty (E). An example of such cell labeling is depicted in Figure 2.

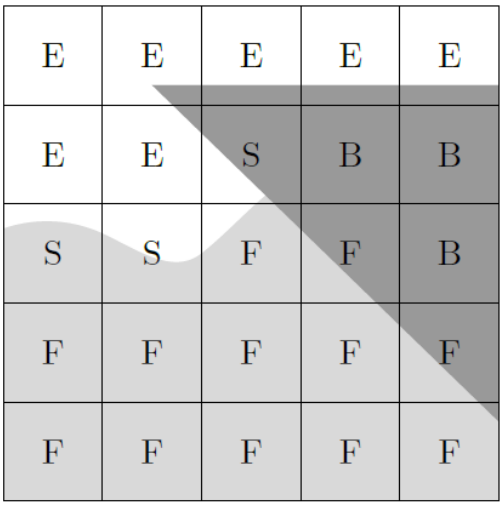

Figure 2: Example of cell labeling. The colors depict the geometry cell labels, where dark grey is solid object, light grey is water and white depicts air. The letters denote if at the current time step the cell is empty (E), the surface (S), mostly fluid (F) or a fixed boundary cell (B), adopted from [16].

2.3 Discretization

In order to perform a numerical simulation, the Navier-Stokes equations have to be discretized in space and time. The ComFLOW software allows for a couple of options regarding the discretizations.

To achieve a high accuracy, the second-order Adams-Basforth method is used for time discretization. For a test problem of the form $\frac{du}{dt} = f(u)$ this explicit multi-step method can be written as

$$u^{(n+1)} = u^{(n)} + \delta t f\Big(\frac{3}{2}u^{(n)} - \frac{1}{2}u^{(n-1)}\Big),$$

where δt denotes the size of the time step and the superscript (n) denotes which time step it is. The new time level is denoted by value $n + 1$.

The spatial discretization in ComFLOW is based on the finite-volume method. For convection the second-order upwind scheme is used. It maintains a high accuracy on both fine and coarse grids [22]. This property is favorable considering the use of local refinement zones, because of which the domain is split into three areas of different grid resolution. The second-order upwind is expected to perform well in all of them. The local refinement zones, which are used in the simulations, are discussed in Subsection 5.3. Another advantage of the second-order upwind method is that it is stable compared to, for example, second-order central discretization. The size of the time step is adjusted throughout the simulation to ensure that the necessary condition for numerical stability is fulfilled, as discussed in Subsection 2.4. Furthermore, note that in general the upwind schemes incorporate the use of artificial diffusion, which can affect the wave dynamics. Fortunately, the second-order upwind increases the diffusion in the system less than the first-order alternative. In addition, on finer grids the effects of artificial diffusion diminish [22]. Therefore, the use of second order upwind on a fine computational mesh should accurately approximate the fluid flow. For an arbitrary time step, the second-order upwind formula in one dimension is

$$\frac{du}{dx} = \frac{\frac{3}{2}u_i - 2u_{i-1} + \frac{1}{2}u_{i-2}}{h},$$

where h is the spatial step size and subscript i denotes the value at the i-th grid point.

However, near the boundaries and free surface, the convection scheme has to be changed to the first-order upwind method [16]. This is because the higher-order method requires more grid points for the discretization, which is not feasible in those areas. The advantage of the first-order upwind scheme is the increased stability, but at the cost of lower accuracy. The formula for first-order upwind discretization is

$$\frac{du}{dx} = \frac{u_i - u_{i-1}}{h}.$$

The default diffusion scheme used in ComFLOW is known as the improved LS-STAG [16]. The LS-STAG method was introduced by Y. Cheny and O. Botella in [6]. This is an immersed boundary (IB) method, which implies that the boundaries of an object do not align with the computational grid. For this method, the object boundaries are approximated by linear line segments [4]. Then, the equations are discretized in the cut cells. An interested reader is referred to [4], for a more detailed description of the method. Note that in wave dynamics diffusion is generally much smaller than convection.

2.4 Numerical methods

The first action for obtaining the solution of the discretized equations for each time step is to find the pressure field. The pressure field follows from the Poisson equation $\Delta p = RHS$, where RHS contains information regarding convection and diffusion.

The pressure field is calculated with the use of the biconjugate gradient stabilized method (BiCGSTAB) with the incomplete LU factorization preconditioner (ILU(0)). The BiCGSTAB method was introduced by van der Vorst in 1992 as an alternative for the Conjugate Gradients-Squared (CG-S) method [20]. The corresponding algorithm for a problem of the form $Ax = b$ is visible below (adopted from [20]).

UNPRECONDITIONED BICGSTAB ALGORITHM

x_0 is an initial guess; $r_0 = b - Ax_0$;
$\hat{r}_0$ is an arbitrary vector, such that
  $(\hat{r}_0, r_0) \neq 0$, e.g., $\hat{r}_0 = r_0$;
$\rho_0 = \alpha = \omega_0 = 1$;
$v_0 = p_0 = 0$;
for $i = 1, 2, 3, ...,$
  $\rho_i = (\hat{r}_0, r_{i-1})$; $\beta = (\rho_i/\rho_{i-1})(\alpha/\omega_{i-1})$;
  $p_i = r_{i-1} + \beta(p_{i-1} - \omega_{i-1} v_{i-1})$;
  $v_i = Ap_i$;
  $\alpha = \rho_i/(\hat{r}_0, v_i)$;
  $s = r_{i-1} - \alpha v_i$;
  $t = As$;
  $\omega_i = (t, s)/(t, t)$;
  $x_i = x_{i-1} + \alpha p_i + \omega_i s$;
  if x_i is accurate enough **then** quit;
  $r_i = s - \omega_i t$;
end

A preconditioner should speed up an iterative algorithm and decrease the computational cost. During an Incomplete LU factorization a matrix A is rewritten as

$$A = LU + R,$$

where L and U are lower and upper triangular matrices and R is a residual matrix than contains small entries. Due to the low significance of R it is neglected. In ILU(0) the sparsity pattern of matrix A is preserved for the L and U matrices [25].

The BiCGSTAB solver with an ILU(0) preconditioner to solve the pressure field is a suitable choice for the project. The reason for it is that out of other methods available in the ComFLOW software, it is the only one that can manage both local grid refinement (discussed in Section 5.3) and GABC boundary conditions. The final accuracy of this Poisson solver is set to 10^{-7} to ensure a high accuracy of the solution.

Once the pressure field at the time step is found, the velocity values are updated and the displacement of the free surface is computed. A Volume-of-fluid (VOF) approach is used for this purpose.

In order to represent the water interface, each computational cell is assigned a volume fraction F. This value represents the percentage of fluid present in the computational cell, as depicted in Figure 105a. To reconstruct the free surface from the volume fractions a Piecewise Linear Interface Calculation (PLIC) is applied. As the name of the approach suggests, in each cell the free surface is approximated by a line [12]. This can be expressed through the equation

$$\mathbf{m} \cdot \mathbf{x} = \alpha,$$

where the vector $\mathbf{m}$ denotes the surface normal, the vector $\mathbf{x}$ denotes the position of a point and α is a constant [12]. An example of a PLIC reconstruction is visible in Figure 105b.

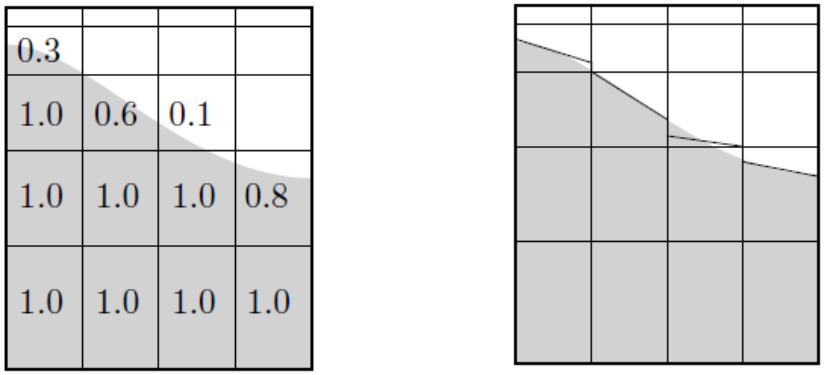

(a) VOF **(b)** PLIC

Figure 3: Free surface reconstruction using Volume of fluid method. Images adopted from [24].

Young's reconstruction method is used to evaluate vector $\mathbf{m}$. Let us consider an arbitrary computational cell (i, j), as depicted in Figure 4. Firstly, the gradients of the volume fractions are calculated at the corners of the considered cell [12]. The equations for the $x-$direction components are

$$\begin{aligned}
m^x_{i+\frac{1}{2},j+\frac{1}{2}} &= \left[\frac{\partial F}{\partial x}\right]_{i+\frac{1}{2},j+\frac{1}{2}} = \frac{1}{2\Delta x}[F_{i+1,j+1} - F_{i,j+1} + F_{i+1,j} - F_{i,j}] \\
m^x_{i+\frac{1}{2},j-\frac{1}{2}} &= \left[\frac{\partial F}{\partial x}\right]_{i+\frac{1}{2},j-\frac{1}{2}} = \frac{1}{2\Delta x}[F_{i+1,j} - F_{i,j} + F_{i+1,j-1} - F_{i,j-1}] \\
m^x_{i-\frac{1}{2},j-\frac{1}{2}} &= \left[\frac{\partial F}{\partial x}\right]_{i-\frac{1}{2},j-\frac{1}{2}} = \frac{1}{2\Delta x}[F_{i,j} - F_{i-1,j} + F_{i,j-1} - F_{i-1,j}] \\
m^x_{i-\frac{1}{2},j+\frac{1}{2}} &= \left[\frac{\partial F}{\partial x}\right]_{i-\frac{1}{2},j+\frac{1}{2}} = \frac{1}{2\Delta x}[F_{i,j+1} - F_{i-1,j+1} + F_{i,j} - F_{i-1,j}].
\end{aligned}$$

Then, the computed values are averaged to determine the x-component of the surface normal for a cell (i, j) [12]. This is expressed through the equation

$$m^x_{i,j} = \frac{1}{4}\left[m^x_{i+\frac{1}{2},j+\frac{1}{2}} + m^x_{i-\frac{1}{2},j+\frac{1}{2}} + m^x_{i-\frac{1}{2},j-\frac{1}{2}} + m^x_{i+\frac{1}{2},j-\frac{1}{2}} \right].$$

The same methodology is used to compute the y-component of the surface normal for the cell. Then, the constant α is determined by ensuring the conservation of volume in the cells [12].

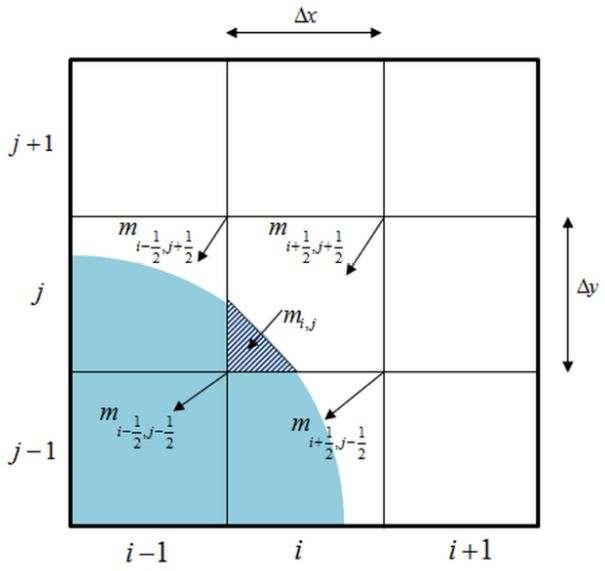

Figure 4: Young's reconstruction method. Image adopted from [12].

Once the reconstruction of the water interface is complete, an advection method is applied to determine the movement of the fluid through the computational cells. For an incompressible flow, this is equivalent to solving the equation

$$\frac{\partial F}{\partial t} + \nabla \cdot (\mathbf{u}F) = 0,$$

where as before F denotes the volume fraction and $\mathbf{u}$ is the velocity vector. In this thesis, the Multidimensional Advective-Conservative Hybrid Operator (MACHO) is used as an advection method. The corresponding scheme, as described in [12], is visible below.

2D MACHO SCHEME

$$F^* = F^n - \Delta t \frac{\partial u F^n}{\partial x} + \Delta t F^n \frac{\partial u}{\partial x}$$
$$F^{n+1} = F^n - \Delta t \left(\frac{\partial u F^n}{\partial x} + \frac{\partial v F^*}{\partial y} \right)$$

The choice of the PLIC-VOF with Young's reconstruction method and MACHO advection scheme was the choice recommended in the ComFLOW manual [16]. A further discussion on the choice of free surface methods can be found in Section 7.

The final action at a time step is the adjustment of the size of the time step δt. It is done based on the CFL-condition, which is a necessary condition for numerical stability [25]. For a two-dimensional

domain the CFL-number is defined as

$$CFL = max_{i,k}\left(\frac{|u_{ik}|\delta t}{h_{x,i}} + \frac{|w_{ik}|\delta t}{h_{z,k}}\right),$$

where as before, δt denotes the time step, u and w are velocity components and h_x, h_z are the corresponding grid dimensions. To ensure that the time steps are not too large, the maximum allowed CFL-number is set to 0.5. If the computed number is greater than that, the time step is halved, after which the condition is re-evaluated. A small CFL-number implies very small time steps, which may overly increase the computational cost. For that reason, if over the duration of 10 time steps the CFL number is smaller than the minimum, which is set as 0.2, the time step is doubled. Additionally, the maximum size of a time step is set to 0.1 and the initial time step at the start of a numerical simulation is equal to 0.01.

This concludes the section on the governing equations and numerical methods. An example of necessary ComFLOW input files, with choices for the numerical methods and simulation settings, is given in Appendix A. A wave model used for the simulations is introduced in Subsection 3.2. Furthermore, a discussion on alternative free surface methods is given in Section 7.

3 Waves: explanation of parameters and mathematical theory

A crucial element of this study are water waves. After all, the goal of coastal defense is to prevent water from passing over the structure and to dissipate its energy. In order to create effective designs, one needs knowledge about the movement of waves. For that reason, this section is an introduction to the topic. Firstly, a physical explanation of the wave phenomena are given. Then, a mathematical theory is briefly introduced. Finally, the statistical data of wave events in the Netherlands is discussed, to justify the choice of parameters used in the numerical simulations.

3.1 Wave terminology and physical explanation

In order to ensure a good understanding some basic wave terminology is introduced. If a body of water is flat, then the position of the surface is known as the still-water level. When there is a disturbance, such as wind, a wave is created. The highest point of the wave is known as crest, and the lowest one is trough. The vertical distance between these two points is known as wave height. The horizontal distance between two consecutive crests (or troughs) is the wavelength. These terms are depicted in Figure 5. A wave period is the time needed for two consecutive crests to pass through the same fixed point.

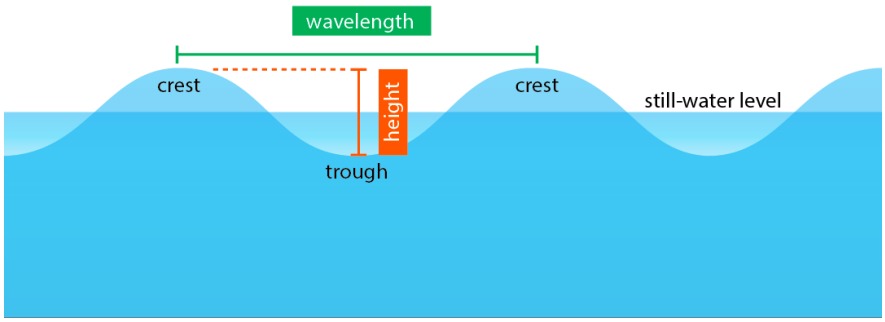

Figure 5: Wave terminology. Image by Byron Inouye adopted from [9].

The wave phenomenon is the transmission of energy over a body of water. What appears to be a crest traveling through the surface, is actually an orbital motion of energy, as depicted in Figure 6. The deeper the energy travels, the more it is dissipated. In a shallow domain, the orbital motion is disrupted by the friction of the seabed, which slows down the bottom layer of the fluid. Because of that, the wave becomes steeper and may reach its breaking point [10].

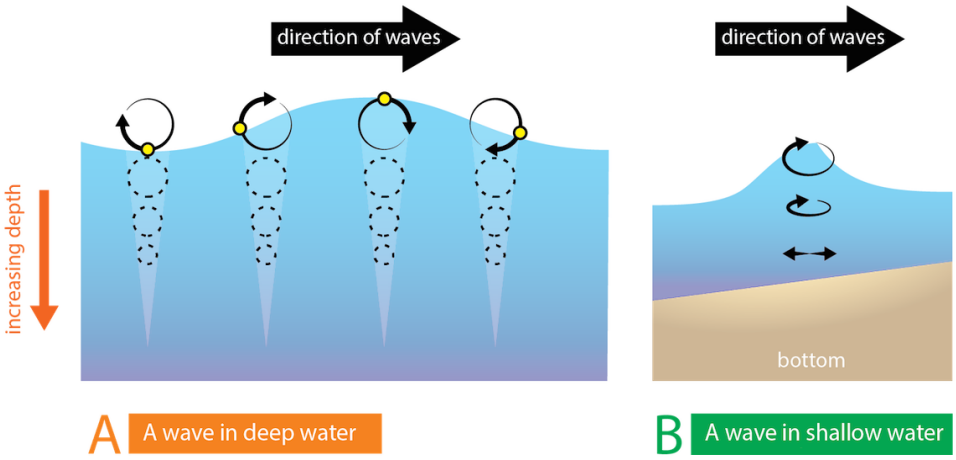

Figure 6: Energy passing through water in orbital motion, creating waves, in deep water (A) and shallow water (B). Picture adapted from [10].

Waves of greater height and longer wave periods transfer more energy [7]. This makes them more dangerous, as high forces exerted on the coastal structures could cause damage, or increase the amount of wave overtopping. For that reason, it is important to ensure that coastal structures are effective during such events [18]. The statistical data regarding the occurrence of high waves in the Netherlands is discussed in Subsection 3.3.

3.2 5th Order Stokes Wave theory

Stokes wave theory has been introduced in 1847 as a solution to the propagation of nonlinear waves on deep water [17]. Due to the nonlinearity of the equations, obtaining a higher order model has proven difficult, which is why there has been many follow-up theories on derivations of such models. In 1985 John D. Fenton has derived a fifth-order accurate model, which is the one used in the numerical simulations in this study. This section is a short introduction to the theory, however due to the complexity and length of the calculations, an interested reader is referred to the original paper written by Fenton [13].

Consider a two-dimensional wave, traveling over a domain with flat surface. It is assumed, that the wave does not change its shape throughout the propagation and that the reference frame moves with the same speed. Additionally, let the considered fluid be incompressible, inviscid and irrotational.

As done in Section 2.1, let (u, w) denote the velocity components in the horizontal x and vertical z direction. The stream-function is given as ψ. Due to the incompressibility it holds that

$$u = \frac{\partial \psi}{\partial z} \quad w = -\frac{\partial \psi}{\partial x}.$$

As it is assumed that the fluid is irrotational, the Laplace's equation must be fulfilled, which can be written as

$$\frac{\partial^2 \psi}{\partial x^2} + \frac{\partial^2 \psi}{\partial z^2} = 0.$$

At the solid bottom $z = 0$ of the domain, the boundary condition is given as

$$\psi(x, 0) = 0.$$

Let η represent the height of the free surface from $z = 0$. Then, the kinematic boundary condition on the free surface is

$$\psi(x, \eta(x)) = -Q,$$

where Q is a positive constant denoting the total volume rate of flow below the wave.

The Bernoulli's equation for an incompressible fluid is

$$p + \frac{1}{2}\rho \mathbf{u}^2 + \rho g \eta = C,$$

where C is a constant and g denotes the gravitational force.

Then, by considering the Bernoulli's equation and assuming that the pressure on the free surface is constant, one can derive the dynamic free surface condition, given as

$$\frac{1}{2}\left[(\frac{\partial \psi}{\partial x})^2 + (\frac{\partial \psi}{\partial z})^2 \right] + g\eta = R,$$

where R is a positive constant.

Let H denote the wave height and λ the wavelength. Then, define the wave number as $k = 2\psi/\lambda$ and a dimensionless wave steepness as $\epsilon = kH/2$. Finally, let $\bar{u}$ denote the mean fluid speed for an arbitrary value of z. Then, according to Stoke wave theory, the stream function ψ can be expanded as

$$\frac{k\psi}{\bar{u}} = -kz + \sum_{i=1}^{\infty} \sum_{j=1}^{i} f_{ij} \epsilon^i sinh(jkz) cos(jkx),$$

where f_{ij} are dimensionless coefficients that depend on wave height H, wavelength λ and mean water depth d.

To derive the 5th order model, Fenton in [13] has performed a Stokes expansion around the wave steepness ϵ. After lengthy computations, the solution to the steady wave problem is given as

$$\phi(x, z) = -\bar{u}x + C_0 \sqrt{\frac{g}{k^3}} \sum_{i=1}^{5} \epsilon^i \sum_{j=1}^{i} A_{ij} cosh(jkz) sin(jkx) + O(\epsilon^6),$$

where ϕ is the velocity potential and dimensionless coefficients are denoted as C_0 and A_{ij}.

The fifth-order Stokes model can accurately represent the dynamics of non-linear waves, which is the reason why it is used in this thesis. The alternative models available in ComFLOW are lower-order. As such, they would result in a less realistic description of the waves. In the simulations, the wave height and velocity at the inflow boundary are determined with the chosen wave model [16]. For further details regarding the 5th order Stokes theory, an interested reader is referred to Fenton's paper [13].

3.3 Choice of wave event

One of the most important choices for this study, is that of the wave event used in the numerical simulations. There are certain aspects that have to be considered before a decision is made, such as the safety standards, statistical data about wave events and computational limitations.

Firstly, let us refer to the Dutch standards for efficiency of coastal dikes. The protection level of a dike is determined by the maximal wave height that the structure is expected to withstand and is denoted by the probability of exceedance of this event. This standard is altered depending on the importance of a region, which is based, for example, on how populated the area is. In the Netherlands, a high level of protection is 1 in 10,000 years. On the other hand, in less important regions, it is 1 in 4000 years, which can still be considered a very high standard [18]. Based on this, a good choice of a wave event to be used in the simulations, is one that has a low probability of occurrence.

Let us consider the probability of certain wave event based on the statistical data included in the European Overtopping manual [18]. The wave height has been measured at the North Sea between the year 1979 and 2002. The data gathered, alongside the extrapolation, is visible in Figure 7. As mentioned, the high protection standard in the Netherlands is a wave event of probability 1 in 10,000 years, which according to this data corresponds to a 10.95m high wave.

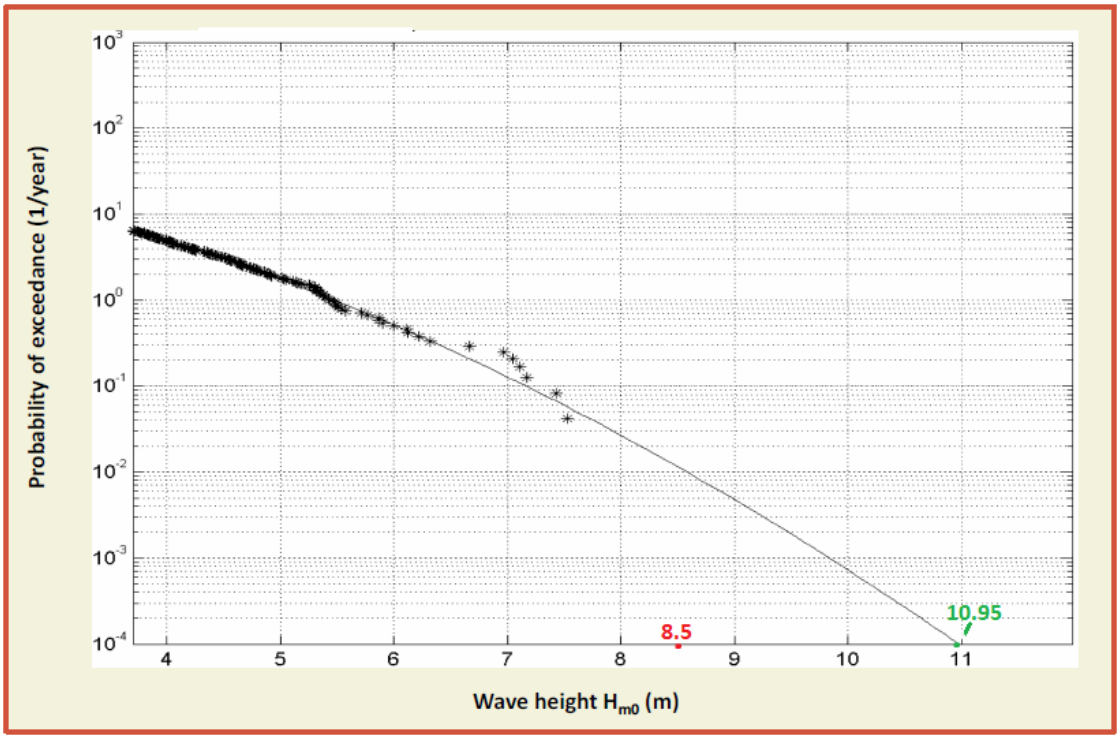

Figure 7: Wave height at the North Sea measure between 1979 and 2002 and the extrapolation of results. The green dot at the end of the extrapolation curve denotes a 10.95m wave, which has a probability of occurring 1 in 10,000 years. The red dot denotes the wave event considered in this thesis, which is 8.5m high. Image adapted from [18].

To decide on the wave event for this study, one should also consider the limitations. Firstly, the focus of this thesis lies in a small part of a dike design, namely the roughness elements. This reduces

the possible changes to the dike design. Finally, a high wave event requires a bigger domain, which increases the computational cost and the computing time of the simulations.

The choice of wave event for this project, is an 8.5m high wave, which has a probability of occurrence 1 in 100 years, as visible in Figure 7. The wave period is chosen as 7.5 seconds, to ensure that a simulation does not take too much time computationally. The wave period is not shortened more, as a longer wave period corresponds to higher energy transmission [7]. Finally, a singular wave event is considered in the simulations. Once more, this is done to shorten the time of each numerical simulation. This concludes the discussion on the choice of wave event.

4 Dikes: common build, terminology

Dikes are the most common type of coastal defense in the Netherlands [18]. An important characteristic of them is that water is only present at one side of the structure. Firstly, let us discuss the main elements of a general dike build, which are foreshore, berm, slope and crest, as visible in Figure 8.

A foreshore is placed in front of a coastal dike and is characterized by a horizontal or mild slope not exceeding 1:10 ratio. This part of the structure incites wave breaking and can reduce the wave height. It is the most effective in shallow water domain [19].

A berm, is a short part of the structure placed at the designated sea level. The slope is either horizontal or very mild, with a maximum ratio of 1:15.

The crucial part of the dike is the seaward slope, which can be located both above or beneath the surface. In comparison to other elements, it has a steeper slope between 1:8 and 1:1. A study on how the angle of the slope affects the wave overtopping has been conducted by G. Lleshi in [15]. It has been found that the steepness reduced the velocity of the wave. However, if the angle is too big, it may negatively affect the wave overtopping.

Finally, the crest may be horizontal or slightly rounded, and it is located on the top of the structure. The water passing the crest cannot return to the sea, and is known as wave overtopping.

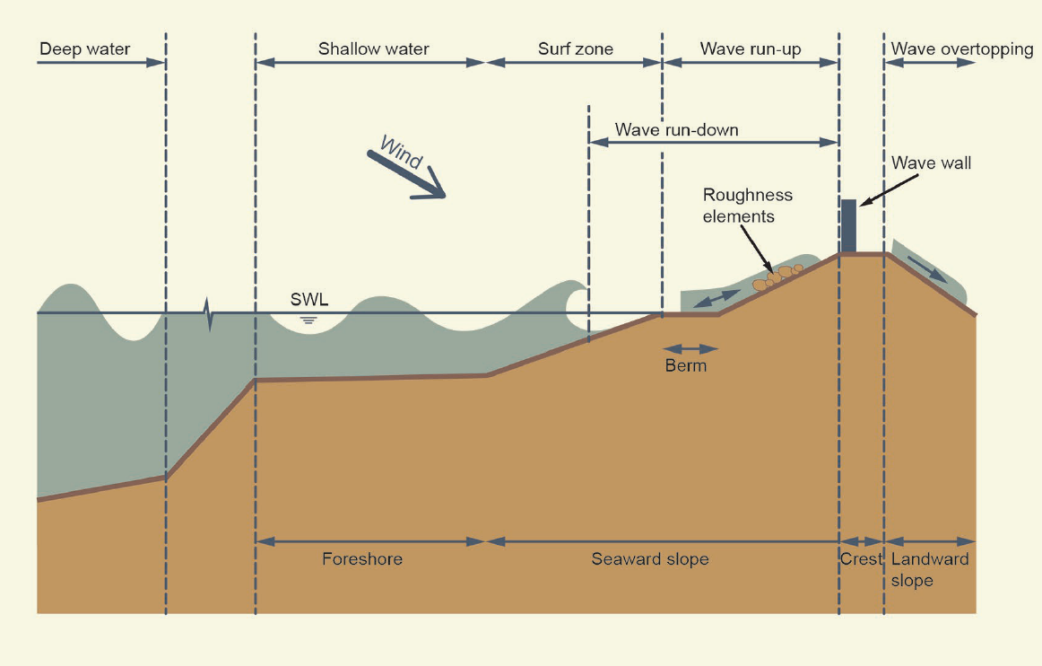

Figure 8: General dike design and wave zones, adopted from [18].

The part of dike that is studied in this project are the roughness elements. These objects can differ in shape and sizes depending on the design. They are usually placed on the seaward slope above the surface level. Their purpose is to dissipate wave energy and reduce wave overtopping. However, it is important to note that they do not only influence the wave run up, but also how the water runs down the dike back to the sea. This influences how the elements should be set up on a structure.

Designs of roughness elements can differ significantly in complexity. Some may be shaped like simple rectangular blocks, while other may be more irregular. They can be placed next to each other like ribs, or spread out more in a chessboard pattern. Most designs include a 'path' that allows the water to flow down more easily. An example of such designs is visible in Figure 9.

Figure 9: Examples of roughness elements: rib setting (left) and chessboard setting (right). Image adopted from [18].

In recent years, the design of roughness elements has significantly improved. One approach that has been considered in the Netherlands, is the use of smaller, more complex block revetments, as depicted in Figure 10. Modern designs often incorporate 'channels' that assist in redirecting the flow. For some of the designs, the blocks are placed next to each other over a large portion of the slope, while other allow for a more spread-out placement.

Figure 10: Hillblocks® 'Basic' revetment block, developed by Deltares. Image from [18].

Finally, it should be noted that there are alternative coastal defenses structures that are not considered, due to time limitation of this project. Some of the more interesting methods could be rubble mounds, or plantation of mangrove forests. An interested reader in referred to the European Overtopping Manual for more information [18].

5 Simulation setup

In this section the aspects related to the simulation setup are discussed. Firstly the geometry of the domain is explored, with inclusion of initial designs. Then, the methods used for data gathering are explained. The final element considered in this section is the construction of the grid. The accuracy of the final setup is justified through comparison of results with a reference solution.

5.1 Domain

The purpose of the numerical simulations is to study the efficiency of the coastal dike design during a singular wave event. As discussed in Subsection 3.3, the considered wave is to be 8.5 meters high, which is a 1 in 100 years event in the Netherlands. The basic geometry is meant to represent a coastal area with a smooth dike. The elements of such a structure are explained in Section 4. The roughness elements will be added at later stage of the study. Moreover, the domain should include a natural looking sea bottom. In real life, the water movement would displace loose materials, such as sand, changing the structure of the sea bottom. However, this sediment dynamics cannot be modeled using ComFLOW. For that reason, in the numerical simulations the sea bottom is considered a solid material with no movement. Finally, the domain should include a less shallow section, to allow the wave to propagate.

The initial trial of the geometry setup is visible in Figure 11. The earliest idea of measuring the overtopping was to include an empty 'tank' past the crest of the dike, where the water could gather. However, this approach turned out to be unsuccessful. The issue was that only part of the water flew into the 'tank', while the rest went past it and outside of the domain. Moreover, due to high velocity of the water, there was a lot of splashing and turbulent flow caused by the water hitting the walls of the tank. This significantly prolonged the computational time. Furthermore, there was a mistake in the initial geometry regarding the orientation of the berm, which was placed vertically instead of horizontally. Finally, the underwater seaward slope was too steep considering the standards discussed in Subsection 4.

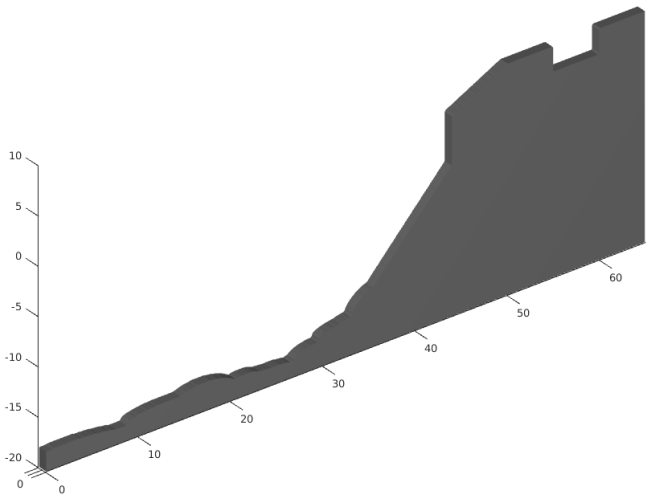

Figure 11: Initial domain geometry.

The domain geometry has been improved, through the modification of the defective elements of the initial design, as visible in Figure 12. The seaward slope underneath the mean water level is less steep, with ratio 1:4. The slope above the water surface has steepness 1:2. A short horizontal berm connects the two seaward slopes. Furthermore, the natural sea bottom, acting as a foreshore, has been prolonged to allow for more deeper water dynamics to occur. Finally, the crest of the dike has been modified and the previously included 'tank' has been removed. In real life, overtopping is the water passing over the dike. However, with this design the water flowing past the initial part of the crest is considered, which can still exit the domain. To counteract that, the crest has been overly prolonged, and the simulation is to end before that occurs. The appropriate end time is determined through numerical experimentation.

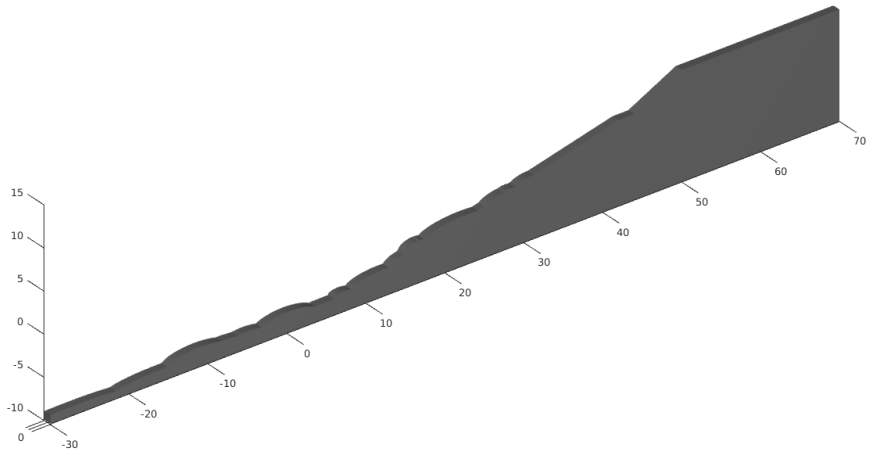

Figure 12: Modified domain geometry, used as reference solution for later simulations.

The disadvantage of the discussed geometry is the extensive computational time, caused by the dimensions of the domain and by a high amount of computational grid cells. In Section 5.3 the grid modification, meant to shorten the computational time and to conserve high accuracy, are discussed in detail. To shorten the computational time, the natural foreshore has been reduced, as visible in Figure 13. The dimensions of this domain are 80 meters horizontally, and 25 meters vertically, with vertical level $z = 0$ denoting the mean surface level. The ComFLOW input file corresponding to this domain is given in Appendix C.

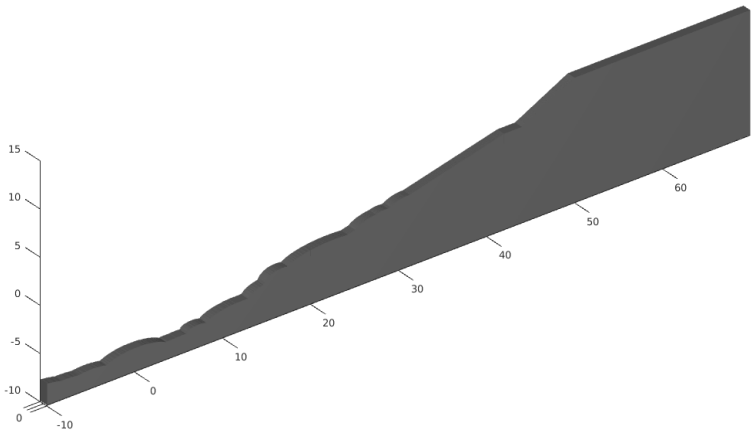

Figure 13: Final domain geometry, referred to as Structure 1.

For this final geometry, referred to as Structure 1, the end time of the simulations has been set to 4.3 seconds, as within that time frame the water does not exit the domain. The comparison regarding the coastal protection efficiency is based on the initial wave overtopping. However the improvement of the design of roughness elements should be visible during the initial collision with the wave.

An example of a simulation snapshot is visible in Figure 14. It depicts the wave running up the smooth dike at time $3.15s$. The coloring of the image is based on the absolute velocity of the water, on a scale from 0 to 30. The main body of water on the left side of the domain is referred to as the seaside. The roughness elements should be placed on the upper seaward slope, which is located between $x = 44$ and $x = 50$. For that reason, the snapshots that are used for the analysis of the fluid flow are zoomed in on that part of the domain.

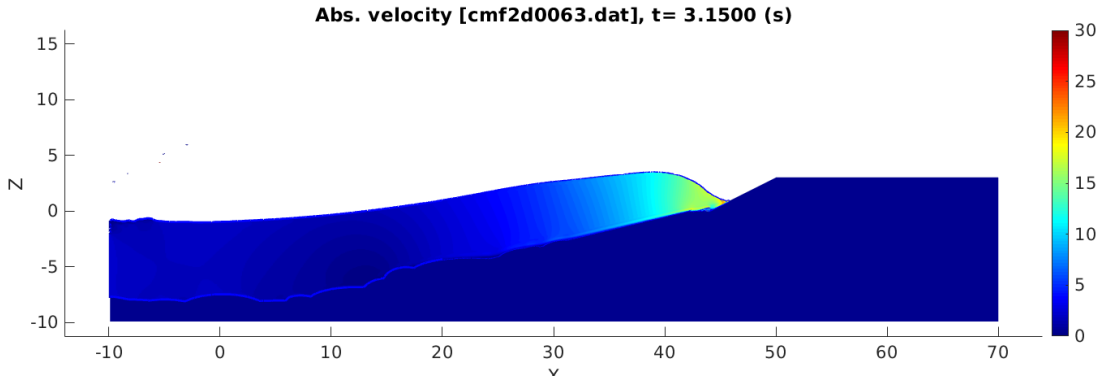

Figure 14: Wave run-up on Structure 1, at time $3.15s$.

The simulation with the smooth dike design, as visible in Figure 13, is used as a reference solution to study how much modification of the structure affects the efficiency. For later simulations, the roughness elements are added on top of the upper seaward slope. The design of these elements is discussed in more detail in Section 4.

5.2 Data gathering

The ComFLOW software allows the user to obtain additional information about the fluid flow, through three components: fill box, force box and monitor points.

The fill box measures the amount of fluid in a given area. As such it is the most important information for this study. For the numerical simulations the fill box is placed on the prolonged part of the crest, as visible in Figure 15 as a blue shaded area.

The force box registers the amount of hydrodynamic forces on structures in a designated area. For the simulations the force box is placed around the seaward slope above the surface level, which is where the roughness elements are placed in later simulations. The placement of the box is visible in Figure 15, where the area is shaded green. The information regarding hydrodynamic forces can be used to analyze the magnitude of stress exerted to the structure.

The monitor points gather the information regarding specific locations in the domain. For this study, they are used to analyze the velocity of the water. Three monitor points are placed slightly above the upper seaward slope. The first one is at the beginning of the roughness elements at position $(44.0, 0.25)$. The second one is in the middle, at position $(47.0, 1.75)$. The last point is at the beginning of the crest at position $(50.5, 3.25)$.

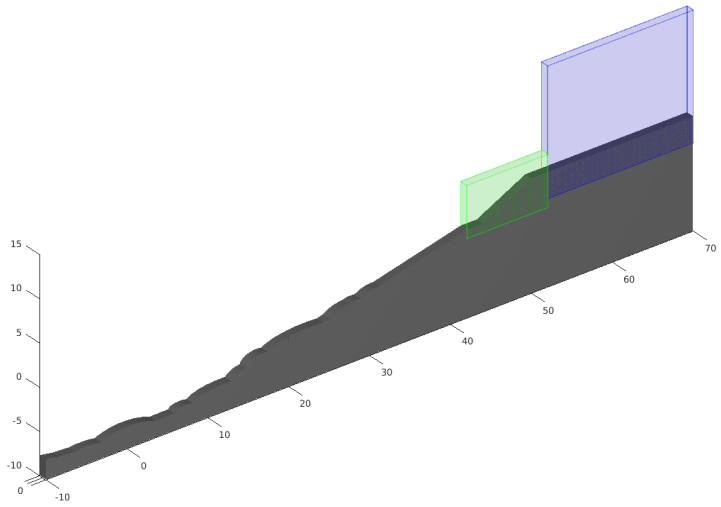

Figure 15: Force box (green) and fill box (blue).

The information gathered through these components is used to analyze the efficiency of each design of roughness elements. The discussion of later results is included in Section 6, alongside the snapshots from the simulations.

5.3 Grid stretching and local refinement

To obtain high accuracy of numerical simulations a fine grid is required. For that reason, an initial trial of a simulation was performed on a fine, uniform grid applied to the whole domain. However, it significantly increased the computational time and expenses. As such, an alternative mesh was necessary to reduce the duration of each simulation.

Throughout the search for the computational grid, the goal was to determine a less excessive mesh, that retained a high precision near the roughness elements. In order to achieve that, two modifications were applied, in the form of grid stretching and local refinement zones.

Grid stretching is a process, in which the dimensions of each cell are increased the further away it is from a specified reference point. In this study the center of stretching is $(50, 1.5)$, which is located on the middle of the upper seaward slope. The stretching is applied in both direction, with the horizontal ratio being 1.0011 and the vertical factor is 1.005.

In local refinement zones the number of grid cells is increased, through reduction of the vertical and horizontal dimensions with a factor of 2. For the numerical simulations two levels of refinement are applied, with the finest grid level in areas where the dynamics of the fluid are more important. The first refined zone is placed in the inner part of the domain, around both of the seaward slopes. The second level is located around the upper seaward slope, which is the area where the roughness elements are to be placed.

The base mesh, without the consideration of the applied refinement zones, has resolution 1200×350. With both refinement zones and stretching modifications, the smallest grid cells, located on the upper seaward slope has length approximately $0.011m$ in both directions. The largest grid cell in the domain, near its border, has size $0.111m$ horizontally and $0.115m$ vertically. The scaled down depiction of the applied grid is visible in Figure 16. Information about this grid is given in Table 1.

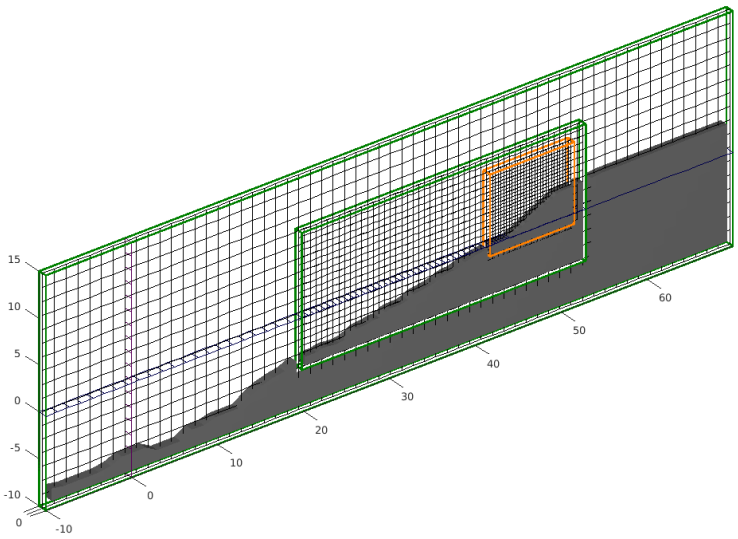

Figure 16: Scaled down grid used for numerical simulations, including two local refinement zones and grid stretching.

Standard grid	
General	
Resolution	1200×350
Smallest grid cell	$0.011m \times 0.011m$
Largest grid cell	$0.111m \times 0.115m$
Grid stretching	
Center	(50.0, 1.5)
Horizontal stretch	1.0011
Vertical stretch	1.005
Local refinement (factor 2)	
Level 1 location	
$xmin$ = 20.0	$xmax$ = 52.5
$zmin$ = -5.0	$zmax$ = 8.5
Level 2 location	
$xmin$ = 42.0	$xmax$ = 51.0
$zmin$ = -1.0	$zmax$ = 7.0

Table 1: Information about the standard grid.

The above mentioned mesh has been used for most of the numerical simulations. However, in case of severe numerical errors, a more refined grid has been applied. The simulations and the reasoning behind this modified grid are discussed in Section 5.3. For the alternative mesh, the first refinement zone has been extended, to include a bigger region of the upper part of the domain. The scaled down version of the modified grid is visible in Figure 17. The summary of the information about this extended grid is given in Table 2. The numerical simulations, where the alternative mesh has been applied, are specified in their corresponding parts in Section 6. The ComFLOW file for the corresponding grid refinement and stretching is given in Appendix B.

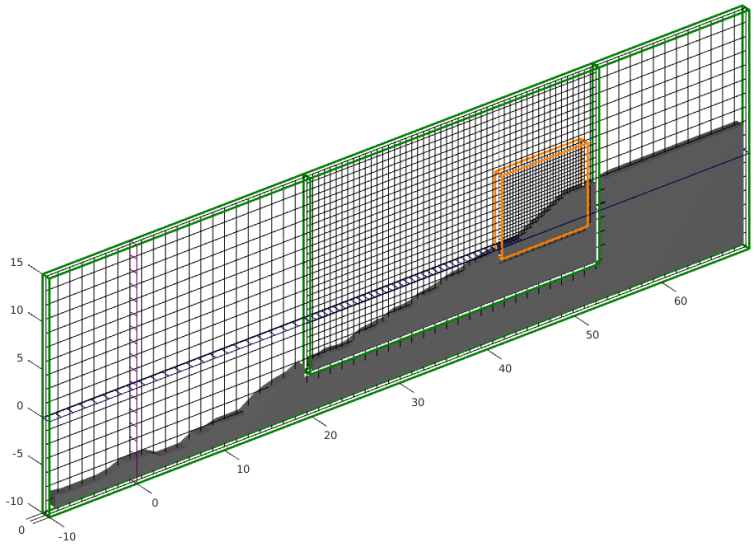

Figure 17: Modified, scaled down grid used for simulations in case of observed significant numerical errors.

Extended grid	
General	
Resolution	1200×350
Smallest grid cell	$0.011m \times 0.011m$
Largest grid cell	$0.111m \times 0.115m$
Grid stretching	
Center	(50.0, 1.5)
Horizontal stretch	1.0011
Vertical stretch	1.005
Local refinement (factor 2)	
Level 1 location	
$xmin$ = 20.0	$xmax$ = 52.5
$zmin$ = -5.0	$zmax$ = 13.5
Level 2 location	
$xmin$ = 42.0	$xmax$ = 51.0
$zmin$ = -1.0	$zmax$ = 7.0

Table 2: Information about the extended grid. Note that the only modification from the standard grid settings is the height of the Level 1 refinement zone, which is extended to $zmax = 13.5$.

5.4 Validation of the shorter domain and grid modifications

The choice of the domain and computational grid can have a large effect on the precision of the obtained results, as well as the computational time. An adequate numerical set up is one that is not exhaustive, yet attains a high level of accuracy. In order to limit the computational time, the length of the domain has been shortened, through the reduction of the natural foreshore, the grid

has been stretched and two local refinement zones have been applied to ensure high precision near the area of interest. This was discussed in more detail in Section 5.3, and is depicted in Figure 16.

In order to validate that these modifications do not significantly lower the accuracy, the simulation results are compared with a reference solution. The reference solution is computed on a larger domain, where the natural foreshore area has not been shortened. The standard mesh applied to that domain has resolution 1875×469. On top of that, two local refinement zones have been applied, as visible in Figure 18. The largest grid cell on that mesh has length $0.053m$ in both directions and the smallest one has $0.013m$. The first local refinement zone is stretched to cover a vast part of the domain, ensuring a higher accuracy of the results. Information about the computational mesh used for the reference domain is given in Table 3.

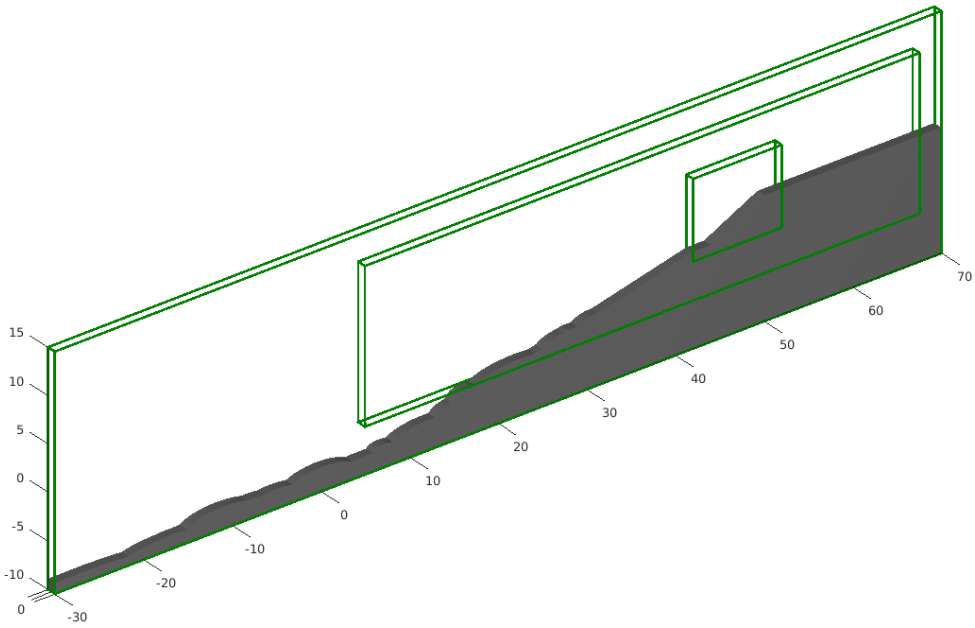

Figure 18: Reference domain and grid, with two local refinement zones denoted with the green rectangles.

The shorter computational time of the reduced domain is the incentive for the choice. A 4.3 second simulation takes only about two and a half days on that domain. While on the larger reference domain, with overall finer computational domain, each simulation takes over a week. Due to the limited time of the project, such an exhaustive setup is not feasible, despite the high accuracy. As such, slightly less precise, yet still adequate results obtained from a shorter simulation are preferred. The comparison of obtained flow dynamics and data is done to ensure that the accuracy is at a sufficient level. To analyze the accuracy, the dynamics of the wave on the seaward slope are considered. The movement of the fluid on the crest is not as crucial. Instead we are interested in the amount of water in that region, which is measured by the fill box. Additionally, the force box readings for both domains should be equivalent. Finally, the data on horizontal velocities at monitor point is compared.

Grid on reference domain	
General	
Resolution	1875×469
Smallest grid cell	$0.013m \times 0.013m$
Largest grid cell	$0.053m \times 0.053m$
No grid stretching	
Local refinement (factor 2)	
Level 1 location	
$xmin = 5.0$	$xmax = 67.5$
$zmin$ = -5.0	$zmax = 11.5$
Level 2 location	
$xmin = 42.0$	$xmax = 52.0$
$zmin$ = -1.0	$zmax = 7.5$

Table 3: Information about the grid used on the reference domain.

Firstly, let us consider the dynamics of the flow. The snapshots from the simulations are zoomed onto the upper seaward slope, as in that area we require a good representation of the fluid movement. The coloring of the images is based on the absolute velocity on a scale 0 to 30. The snapshots for the reference domain, being the one with prolonged foreshore and finer grid, are visible in Figure 19. The images for the domain used in the later simulations, namely the one with reduced foreshore, are depicted in Figure 20. The behavior of the fluid on both domains is very similar. There is a small numerical error, in the form of droplets, visible in Figure 20b. However this does not have an effect on the bulk fluid, as such it can be neglected. At 4 seconds and 4.5 seconds some turbulence is visible in the form of a vortex, located on the beginning of the berm. The absolute velocities of the wave match for both domains. It can be concluded that the reduced domain gives an adequate representation of the fluid flow.

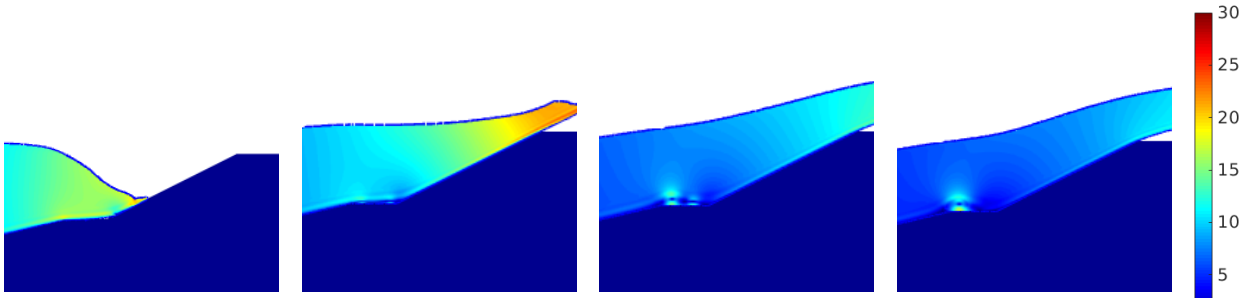

(a) time 3.15 **(b)** time 3.5 **(c)** time 4 **(d)** time 4.25

Figure 19: Wave dynamics on the reference grid. Colors depict the absolute velocity on a scale 1-30.

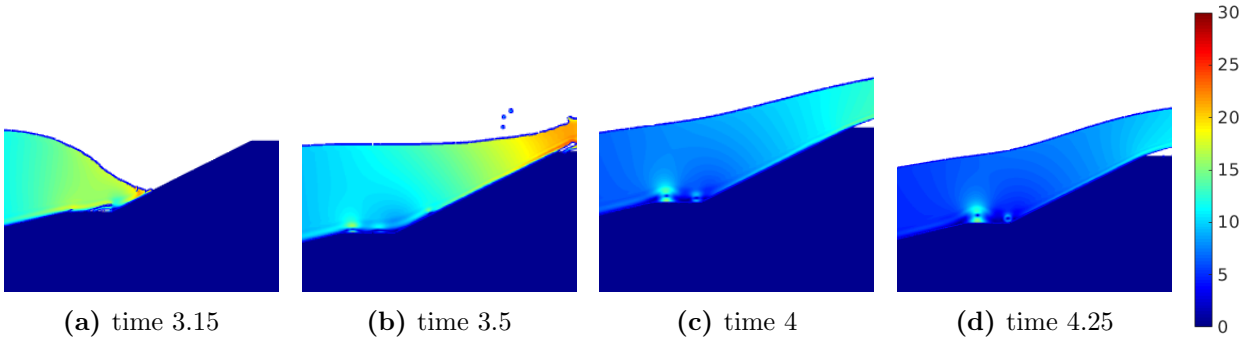

(a) time 3.15 **(b)** time 3.5 **(c)** time 4 **(d)** time 4.25

Figure 20: Wave dynamics on Structure 1. The colors depict the absolute velocity on a scale 1-30.

As mentioned, the accurate representation of the fluid flow after the initial part of the crest is not considered important. Instead, it is the volume of the water in that area that is a crucial parameter. It is measured through a ComFLOW fill box. The results for both domains are visible in Figure 21. The amount of overtopping registered during both simulations is approximately $13.5m^3$. As such it can be concluded that the smaller domain used for later simulations gives an accurate representation of the overtopping parameter.

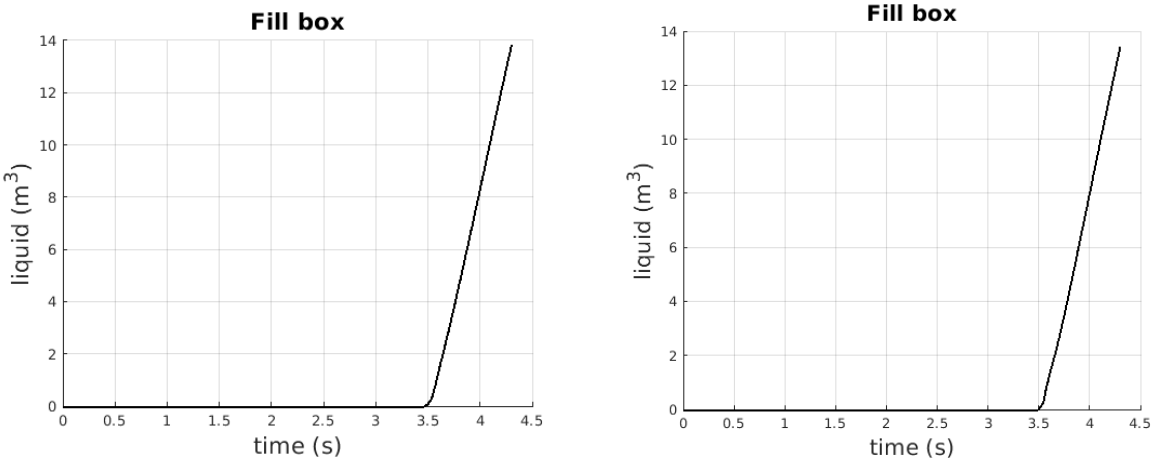

(a) Reference domain **(b)** Considered domain, labeled Structure 1

Figure 21: Overtopping measurement for both domains.

Similarly, the force box measurements, visible in Figure 22, have to be considered. The force is measured in both directions, horizontal one is denoted by (X) and vertical by (Z).

Firstly, let us consider the horizontal force registered, which is depicted in Figure 22a and in Figure 22b. The first peak of the force is visible around time 3.15 seconds for both domains. A high value of the singular peak occurring during a single time-step in Figure 22b can be explained through numerical error, and as such the scale at a single point can be neglected. The second peak of the horizontal force in both cases reaches its maximal value around the time $3.4s$, with magnitude approximately $13 \times 10^4 N$. Then, in both graphs the force diminishes with time, with the value at the end of the simulation being around $8.5 \times 10^4 N$.

The vertical force (Z) of the considered domain resembles the results obtained during the reference

simulation. In both cases, the first singular peak is observed around the 3.15 seconds, with magnitude approximately $-5.5 \times 10^5 N$. The wider peak is observed around $3.4s$, with value of around $-3.5 \times 10^5 N$. At the end of the simulation both readings end at $-2 \times 10^5 N$. It is important to note that the minus sign in vertical measurements is caused by the hydrostatic component pointing in downward direction.

From the analyses of the force box data, it can be concluded that the reduction of the length of the domain and the grid modifications applied do not have a significant effect on the results. Small differences can be spotted, however the overall shape and scale of the functions are in agreement.

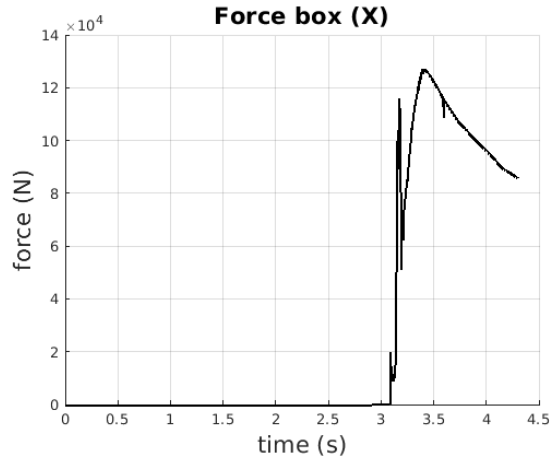

(a) Reference domain, force in horizontal direction.

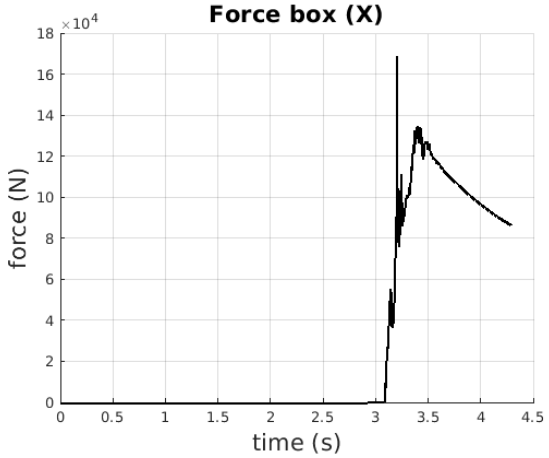

(b) Structure 1, force in horizontal direction.

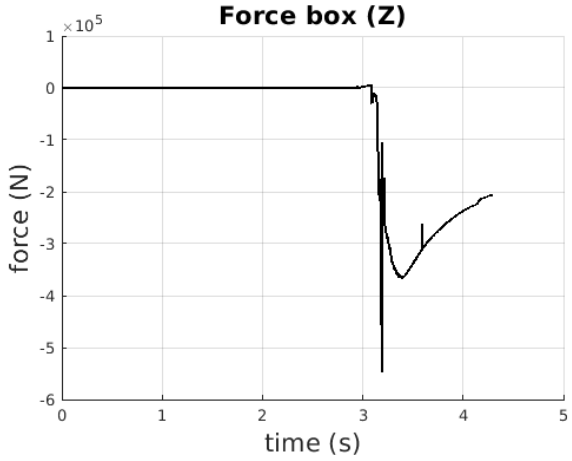

(c) Reference domain, force in vertical direction.

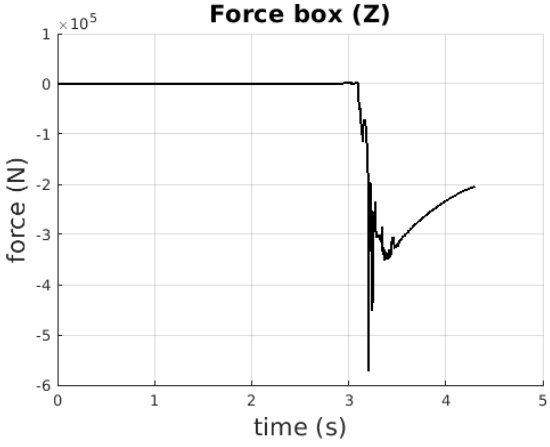

(d) Structure 1, force in vertical direction

Figure 22: Force box measurement for both domains.

Finally, let us consider the data for the horizontal velocity obtained from the monitor points. They are located on the upper seaward slope, the exact positions are given in Section 5.2. The monitor-velocities are given in Figure 23, where the first column represents the reference domain and the second one is the shortened one, which is used for the later numerical simulations.

For the first monitor point both simulations reach the maximal value of approximately $15m/s$, which lessens with time. The shape of the functions slightly differs during the last second of the simulation, where for the reference domain the final velocity is $4m/s$, while the one for the considered domain

stays at approximately $6m/s$.

For the second monitor point the two graphs 23c and 23d are almost identical. Around time $3.7s$ a small disruption can be seen in the measurement for the shorter domain.

The last monitor point is located on the top of the seaward slope. The rough shape of the velocity curves for both domains is very similar. The value of the first peak slightly differs, as the maximal value for the reference domain is approximately $22m/s$, while for Structure 1 it almost reaches $25m/s$. In the reference domain, around time $3.5s$, the velocity values increase until they reach approximately $15m/s$. In the considered domain, around the same time point, the values are also increasing, however starting from a much smaller initial value. After reaching the velocity of approximately $15m/s$, the speed is slowly decreasing. For both simulations, at the final point, the velocity measured is roughly $10m/s$.

From the analyses of the horizontal velocities measured at the monitor points, it can be concluded that for both geometries the shapes and scales of the velocity-curves are very similar. Small differences can be seen, however they do not affect the results in a significant way. The horizontal velocities for Structure 1 are a satisfactory approximation of the results obtained for the reference domain.

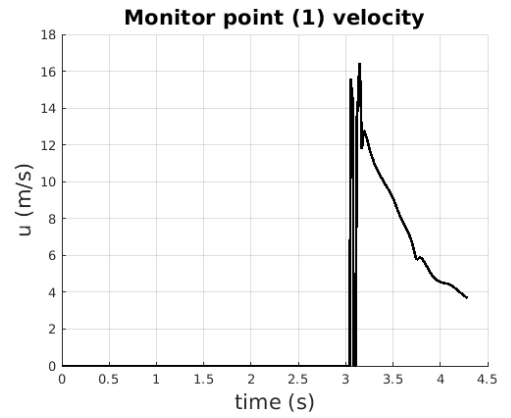

(a) Reference domain

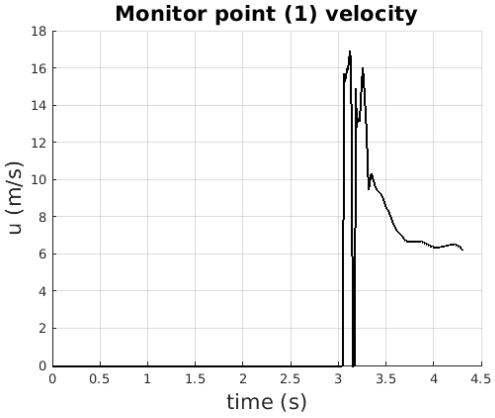

(b) Structure 1

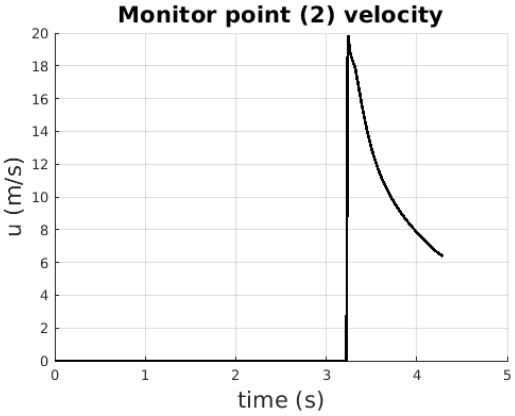

(c) Reference domain

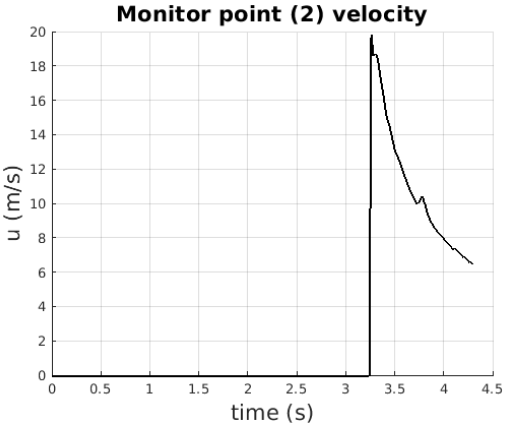

(d) Structure 1

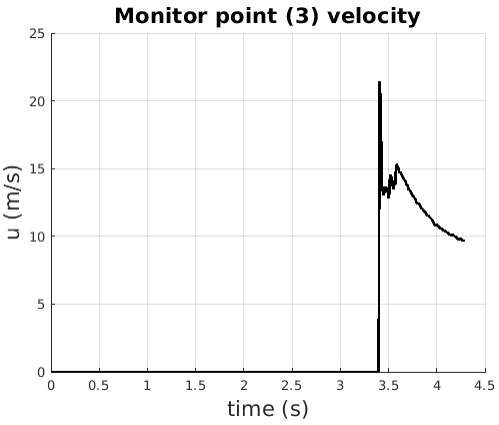

(e) Reference domain

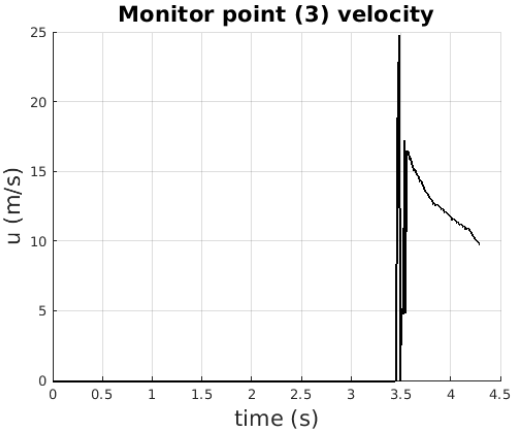

(f) Structure 1

Figure 23: Comparison of the horizontal velocity at the monitor points for the reference domain, and the considered domain, labeled Structure 1.

Summary

The goal of this section was to verify that the domain and computational mesh introduced in Subsection 5.3 gives sufficient accuracy of the results. For that purpose, a larger domain with overall finer mesh was used as a reference solution. The results obtained from both set ups were

compared. It has been shown that the fluid flow on the upper seaward slope is very similar for both numerical simulations. In other parts of the domain, the exact dynamics of the water are not considered as important. Instead, the overtopping parameter, describing the amount of fluid on the crest, is a crucial measurement for this study. For both domains, the fill box data is almost identical. Similarly, the force box functions, indicating hydrodynamic forces in the two simulations, have the same shape and scale. Finally, the monitor points registering the horizontal velocity of fluid, indicated the same dynamics of the flow on both grids. Small dissimilarities can be seen, however they do not have a significant effect on the results. As the computational time of the considered domain is much shorter, and the obtained results depict are adequate, the choice of the computational domain and grid is validated.

6 Simulations of roughness elements

6.1 General design and strategy

To incorporate roughness elements into the simulations, the geometry of the dike is modified. The elements are placed on the upper seaward slope, as that is the usual location for these structures, as discussed in Section 4. Other placement of the roughness elements is not considered, nor other modification of the geometry.

Due to the time limitation of this study, only two dimensional simulations are feasible. Because of that, not every property of the roughness elements can be taken into account. For example, the perpendicular dimension cannot be considered. Consequently one cannot differentiate between cubic blocks and 'rib' blocks, previously depicted in Figure 9. In order to represent certain characteristics, an unrealistic placement of roughness elements is needed in the simulations.

An important property, previously mentioned in Section 4, is that the roughness elements do not only influence the wave run-up, but also how the fluid flows down the dike. In order to allow the water to return to the main body more easily, many designs incorporate an empty 'path' between the roughness elements. To imitate that property in the two dimensional simulations, the roughness elements are placed $0.5m$ above the actual slope of the dike, which gives an appearance of them levitating. An example of such a placement is visible in Figure 24. This design, although not realistic, allows to analyze how the addition of roughness elements can influence the wave dynamics. For example, inducing turbulence in the flow interferes with the wave running up the 'empty path'. Additionally, it is worth noting that the monitor points introduced in subsection 5.2 are located $0.25m$ above the upper seaward slope, which is equivalent to being on the 'empty path'.

Figure 24: General design of roughness elements, with the empty path below.

The goal of the roughness elements is to minimize the amount of overtopping and break down the wave energy. To analyze their efficiency, the results for various designs of these elements are compared with those obtained for a smooth dike, which are given in Subsection 5.4. The type of data gathered for each simulation are introduced in Subsection 5.2.

Firstly, the most important parameter considered is the wave overtopping, which is measured within the specified area. By the end of the smooth dike simulation, the amount of water in the fill box was almost $14m^3$. The more effective a roughness element is, the lower the overtopping parameter.

Secondly, the force in both horizontal and vertical directions is considered. The occurrence of the hydrodynamic forces implies a collision of the wave with the structure. However, an excessive amount can damage the material. The objective for the roughness elements is to create an effective

design that does not significantly increase the magnitude of the forces. For the smooth dike the horizontal force reached approximately $13 \times 10^4 N$, while the vertical one had a singular peak around $-5.5 \times 10^5 N$ and the majority of the force below $-3.5 \times 10^5 N$.

The next aspect of the analyses is the horizontal velocity measured at the monitor points. The interest is in how much the speed of the water changes as it runs up the slope. As the monitor is not always submerged, the gathered data may not be continuous. For the smooth dike, the velocity increased at the points located higher up the seaward slope. For the last monitor point, by the end of the simulation, the water slowed down to $10 m/s$, while the maximum value reached $25 m/s$ at $3.5 s$ (depicted in Figure 23). By inclusion of roughness elements, the intention is to decrease the obtained velocity.

Lastly, the dynamics of the water flow are considered. The snapshots from the simulations, depicting the upper seaward slope, are used to examine the movement of water during the collision with the roughness elements. An overtopping consisting of spray, rather than a compact water mass is a preferable result. As such, a design of roughness elements is considered favorable, if it results in breaking down the wave and incites turbulence in the flow.

In the following subsections, different properties of the roughness elements are studied, such as their dimensions or placement. To properly analyze the effect of each characteristics, several designs may be considered. Based on the obtained results, the geometry of the roughness elements is modified with the incentive of increasing their efficiency.

6.2 Size of the block

The first property of roughness elements that is analyzed is their size. The considered blocks have the same trapezoidal shape, yet differ in their dimensions. The distance between consecutive elements equals their width. Accordingly, the smaller the blocks, the more blocks are placed on the upper seaward slope.

The first design consists of five roughness elements, as depicted in Figure 25a. The dimensions of the blocks are given in Figure 25b, where the width equals $0.5m$ and the height of the block from the water side is $0.75m$. The distance between consecutive blocks is $0.5m$. This design is labeled to as 'Structure 2' for the duration of the thesis.

(a) Design of the roughness elements.

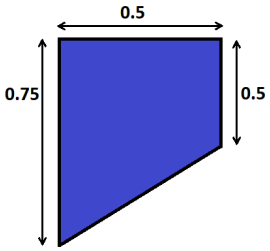

(b) Dimension of the blocks.

Figure 25: Structure 2

The second design has three larger blocks, which are twice as big, as those used in 'Structure 2'. Their width is $1m$ and the height from the water side is $1.5m$, as depicted in Figure 26b. The distance between the blocks equals $1m$, as visible in Figure 26a. The construction is called 'Structure 3'.

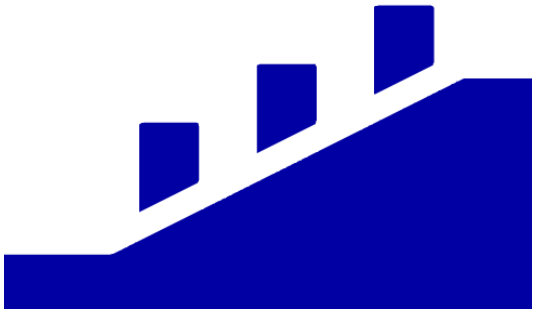

(a) Design of the roughness elements.

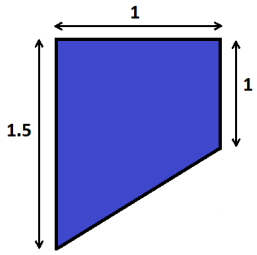

(b) Dimension of the blocks.

Figure 26: Structure 3

To study the efficiency of the designs, let us firstly consider the overtopping measurements. The fill box data for both structures is depicted in Figure 27. As a reminder, for a smooth dike the overtopping reached approximately $14m^3$. The inclusion of both types of the roughness elements reduced that number by a small degree. For Structure 2, the overtopping reached $12m^3$, while for Structure 3 the maximal amount is around $8m^3$. From this, the larger blocks are more efficient in reducing the amount of water reaching the crest of the dike.

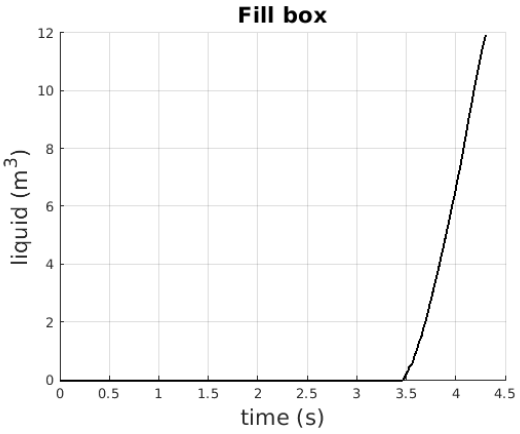

(a) Fill box for Structure 2

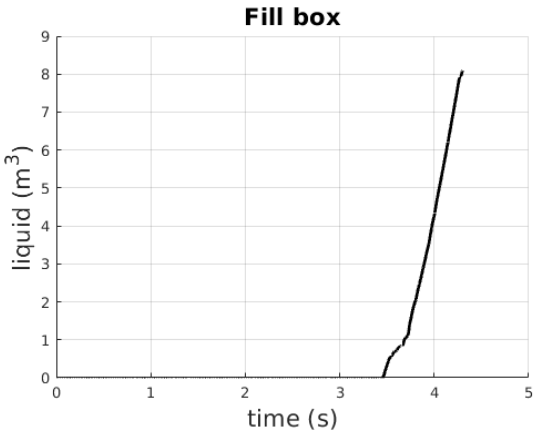

(b) Fill box for Structure 3

Figure 27: Overtopping measurements for Structure 2 and Structure 3.

Secondly, the horizontal force acting on the structures has to be analyzed. They are depicted in Figure 28. For Structure 2 the maximum is obtained at a singular point, at time $3.15s$, reaching $4.7 \times 10^5 N$. Then, another rise in the force is observed around the time $4s$, suggesting another collision of water with the structure. At that time, it reached a lower magnitude of approximately $2.3 \times 10^5 N$. The horizontal force corresponding to Structure 3 has a singular peak of $7 \times 10^5 N$ at

time 3.15s. As expected, for both designs the measurements are higher than those for a smooth dike, caused by a bigger interaction between the modified structures and the incoming wave.

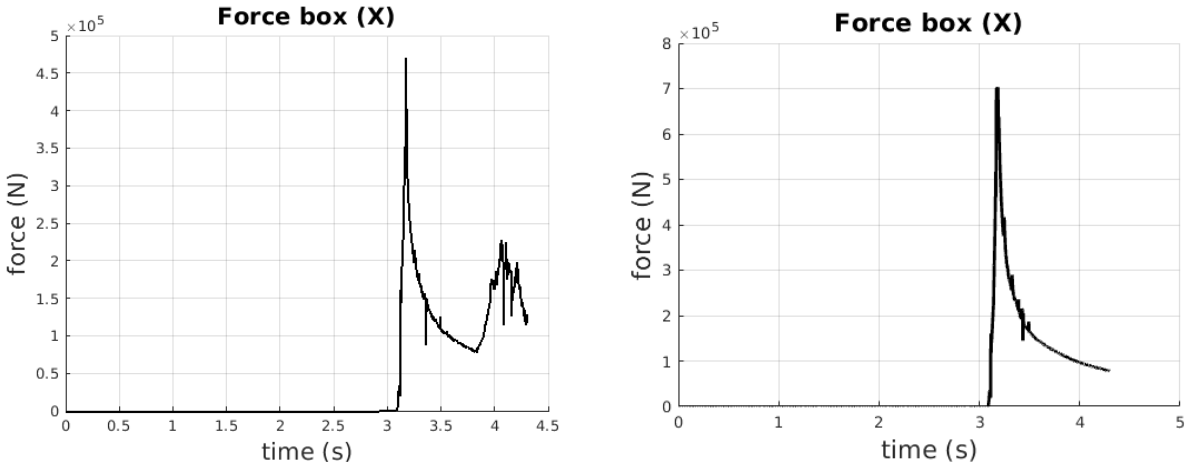

(a) Structure 2 **(b)** Structure 3

Figure 28: Horizontal hydrodynamic force acting on Structure 2 and Structure 3.

In terms of the vertical force, the measurements for both designs are very similar as visible in Figure 29. The maximal value differs by only $2 \times 10^5 N$, being $-16 \times 10^5 N$ for Structure 2, and $-14 \times 10^5 N$ for Structure 3. An additional increase in force can be observed around time $4s$ for the design with smaller blocks. This suggests another collision of the wave with the roughness elements.

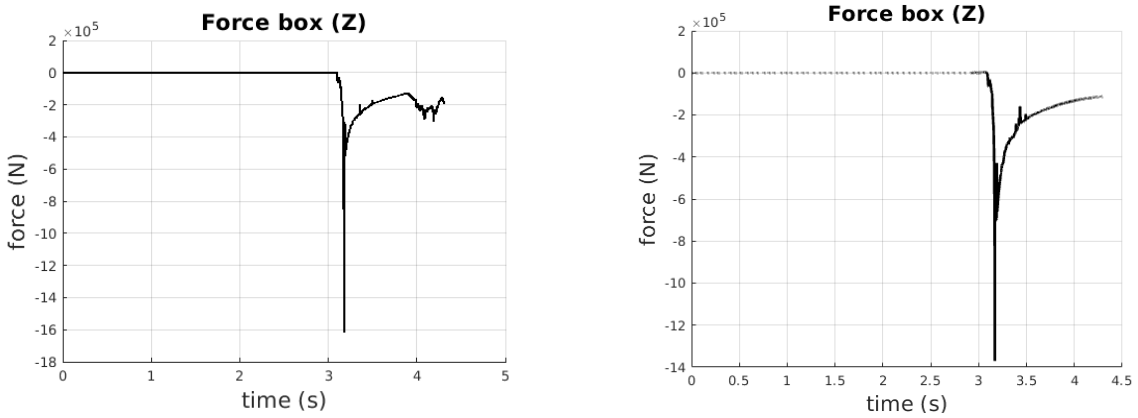

(a) Structure 2 **(b)** Structure 3

Figure 29: Vertical hydrodynamic force acting on Structure 2 and Structure 3.

Next, let us analyze the horizontal velocity registered at the monitor points, given in Figure 30. By eye, at first point both measurements are almost identical, with a minimally higher increase for Structure 2 around time 3.7s. At the second monitor point, up till time $4s$ the velocity for both designs follows the same pattern. After that time, for Structure 3 it continues on slowly decreasing, while for Structure 2 a harsh drop is observed. At the final monitor point, it seems that only droplets of fluid are passing through, causing wiggly signals. For both designs the values registered are between $25m/s$ near the start of the simulation, and drop down to around $10m/s$ at the end.

From the data obtained from the monitor points, it can be concluded that the size of the roughness elements does not have a big influence on the horizontal velocity of particles in the 'free path' of the dike.

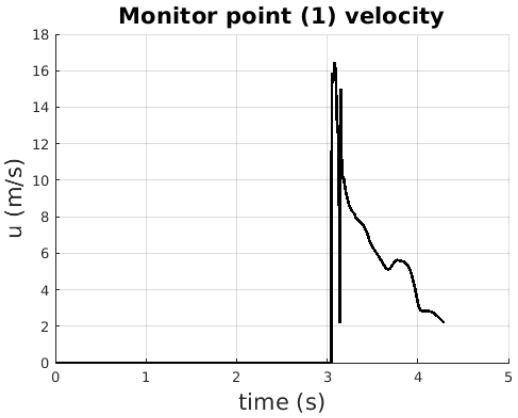

(a) Structure 2

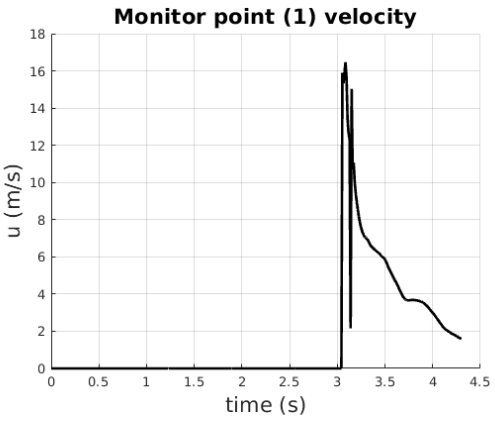

(b) Structure 3

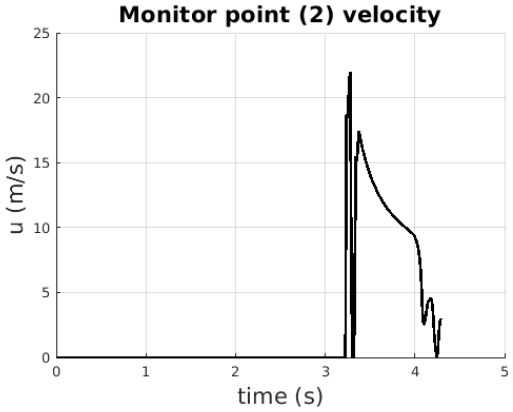

(c) Structure 2

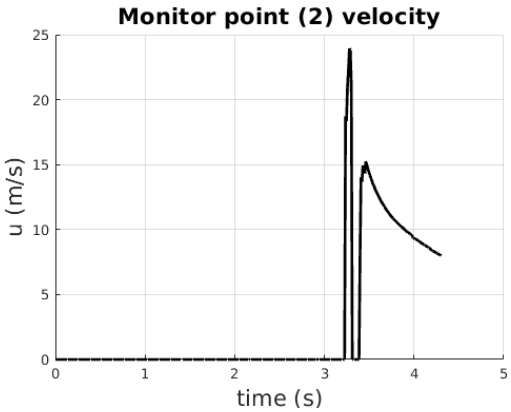

(d) Structure 3

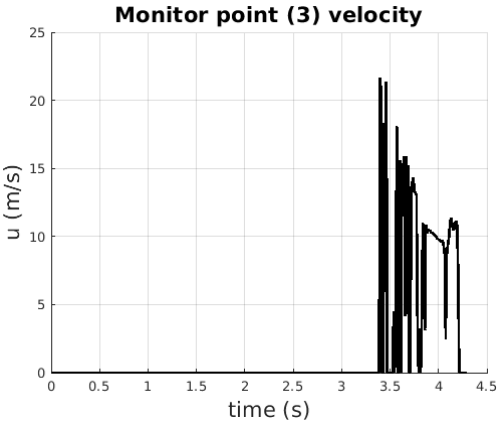

(e) Structure 2

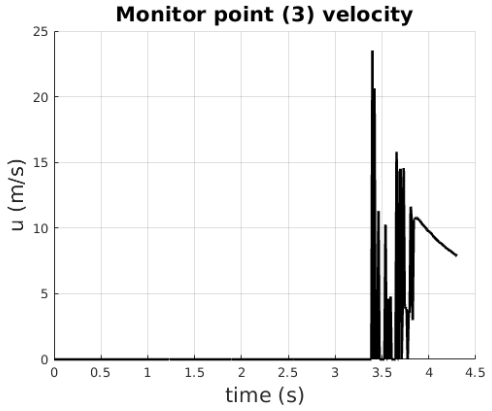

(f) Structure 3

Figure 30: Horizontal velocities at monitor points for Structure 2 and Structure 3.

The final step of the analysis is the study of the water flow dynamics during the collision with the roughness elements. Four time steps are considered for this purpose. The coloring of the plots is

based on the absolute velocity of the water, given on the scale 0 to 30.

The snapshots from the simulation for Structure 2 are given in Figure 31. At time 3.15s the wave collides with the first of the roughness elements. The water shoots around the block, with most of it moving above the elements. Only around time 4s, the fluid drops enough to collide with blocks further ahead. This incites a turbulence of the water between the roughness elements, as visible in Figure 31d. Despite that, most of the water flows above the roughness elements towards the crest. It can be concluded, that due to the small size of the blocks, the efficiency of this design is not much better than that of a smooth dike. However, it can be observed how the blocks may affect the fluid flow, upon a collision with the wave.

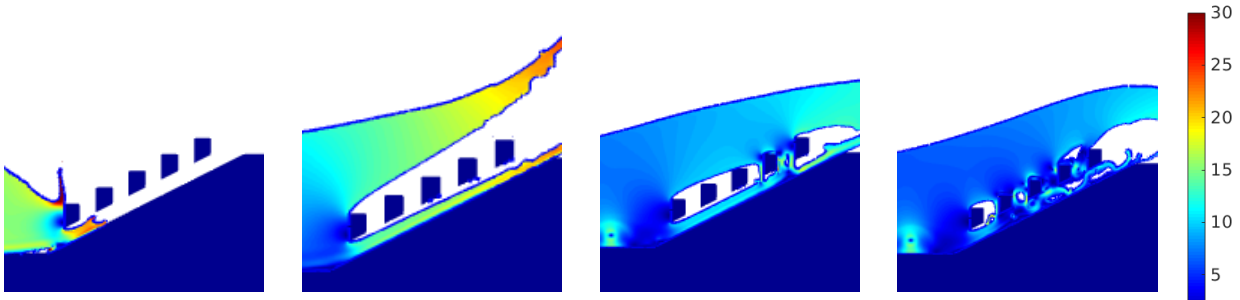

(a) time 3.15 **(b)** time 3.5 **(c)** time 4 **(d)** time 4.25

Figure 31: Structure 2 collision dynamics.

Figure 32 depicts the wave collision with Structure 3. Similar to the other simulation, upon the impact of the wave with the first block, the water travels around the roughness elements. The part above the structure is directed more upward than before, which is caused by the increased hight of the block. Because of that, it takes the water a longer time to fall down towards the other elements. This processed is delayed so much, that it does not occur before the end of the slope. As such, the two latter blocks do not have any effect on the flow, which is a disadvantage. Additionally, there is a minor numerical error spotted at time 3.5, in the form of a small line of droplets connecting the wave with the blocks. A detailed discussion on numerical errors and their relevance is given in Section 7.

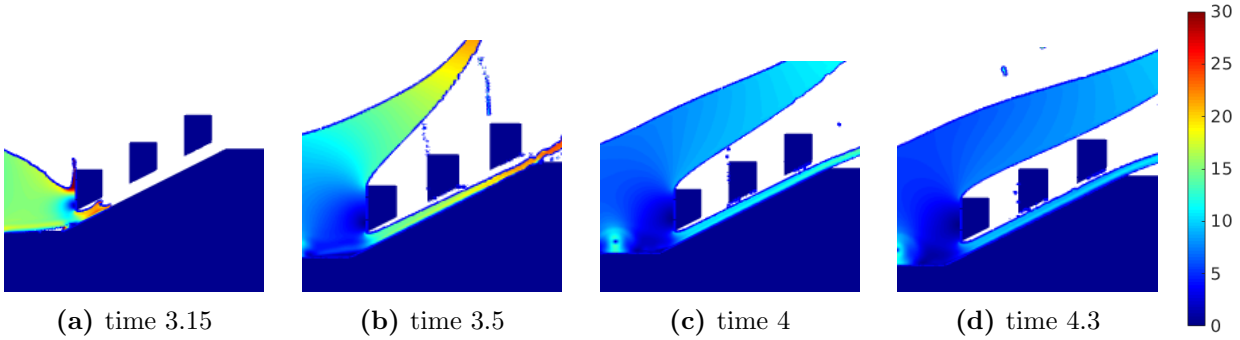

(a) time 3.15 **(b)** time 3.5 **(c)** time 4 **(d)** time 4.3

Figure 32: Structure 3 collision dynamics.

After analysis of the data gathered regarding Structure 2 and Structure 3, it can be deduced that bigger roughness elements are more effective. This can be mainly observed through the reduction of

the overtopping values. A larger block redirects the water more in the upwards direction, changing its trajectory. However, the latter two blocks of Structure 3 did not have any contact with the wave. It is assumed that the more roughness elements the wave collides with, the more efficient the design will be. For that reason, the goal for the next designs is to modify the structure with bigger blocks, such that all of the roughness elements are utilized.

6.3 Slope of upper part of the dike

The second component of the design of the roughness elements considered is the slope of the upper part of the blocks. Previously, in Subsection 6.3, the slope of the top of the blocks was parallel to the horizontal line. In this subsection, an alternative shape of the roughness elements is considered, where the top part is parallel to the upper seaward slope.

The design, referred to as 'Structure 4', is visible in Figure 33a. It consists of three roughness elements, placed $0.5m$ away from each other. The dimensions of each block are given in Figure 33b.

(a) Design of the roughness elements. **(b)** Dimension of the blocks.

Figure 33: Structure 4

As before, let us begin the analysis with the overtopping measurement. The final amount of liquid in the fill box is about $11m^3$. This makes the structure more efficient than Structure 1 and 2, but worse than Structure 3.

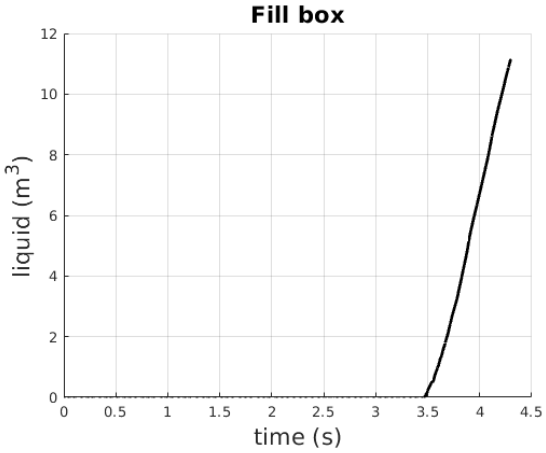

Figure 34: Overtopping measurement for Structure 4.

The readings for the horizontal and vertical hydrodynamic forces strongly resemble those obtained for Structure 2. The maximal horizontal force is around $4.7 \times 10^5 N$ and occurs around the time $3.15s$. Another rise in the magnitude is spotted starting at $3.7s$, suggesting another collision of the water with the blocks. Similarly, the maximum vertical force is reached at a singular point, and equals approximately $-14 \times 10^5 N$. Later on a small increase in the force is seen after $3.7s$.

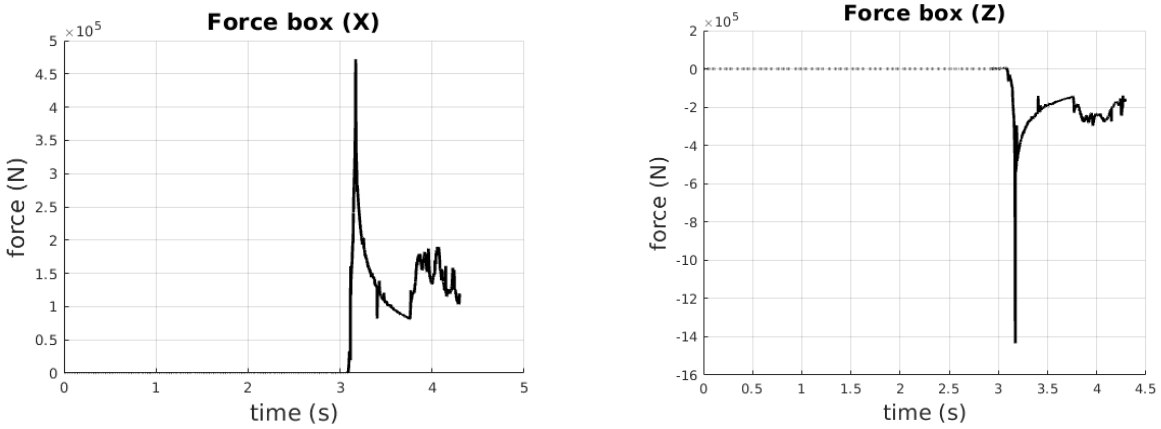

(a) Horizontal hydrodynamic force.

(b) Vertical hydrodynamic force.

Figure 35: Hydrodynamic forces acting on Structure 4.

The next data to be examined, is the velocity data gathered from the monitor points, visible in Figure 36. The scale and shape of the horizontal velocities resemble those previously observed in Subsection 6.2. For the first two monitor points, the functions are relatively smooth, suggesting that only small-scale disruptions to the flow are taking place. For the last monitor point, visible in Figure 36c, large oscillations are observed. This is probably caused by the absence of a big body of fluid traveling through the point in combination with the occurrence of turbulence. From the data, it can be concluded that the alternative slope of the upper part of the roughness elements does not reduce the wave velocity.

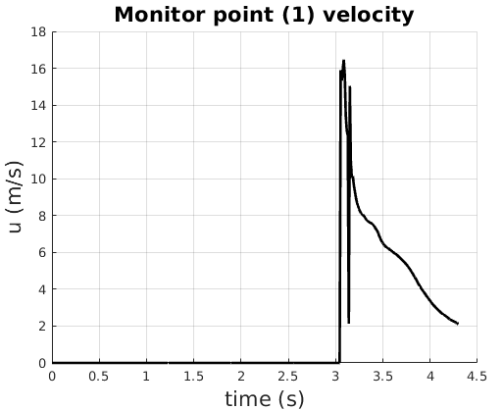

(a) Horizontal velocity at the first monitor point.

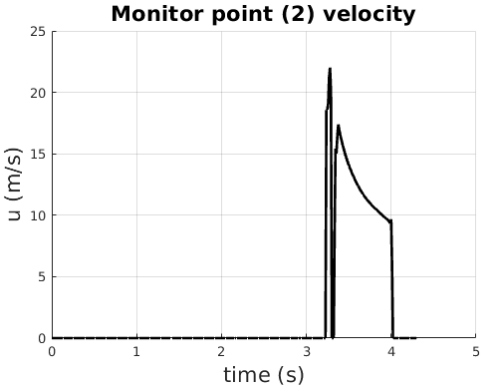

(b) Horizontal velocity at the second monitor point.

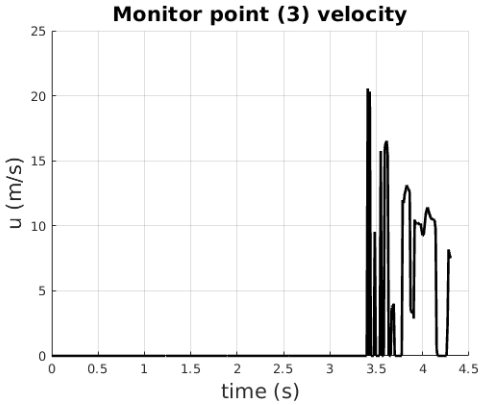

(c) Horizontal velocity at the last monitor point.

Figure 36: Comparison of horizontal velocities for monitor points in Structure 4.

Lastly, the collision dynamics, depicted in Figure 37, are considered. As before, the coloring of the plots is based on the absolute velocity on a scale 0 to 30. At time $3.15s$ the wave crashes into the first roughness element. Due to the shape of the blocks, the water is not redirected upwards. Instead, the trajectory of the big water mass is directed more horizontally, towards the crest. The fluid quickly drops down onto the rest of the blocks, causing turbulence. The effects of this are clearly visible in Figure 37d. The flow of the water traveling through the 'empty pass' is disrupted, thus stopping the majority from reaching the crest. On the other hand, the part of the wave that is above the roughness elements moves towards the crest without much difficulty.

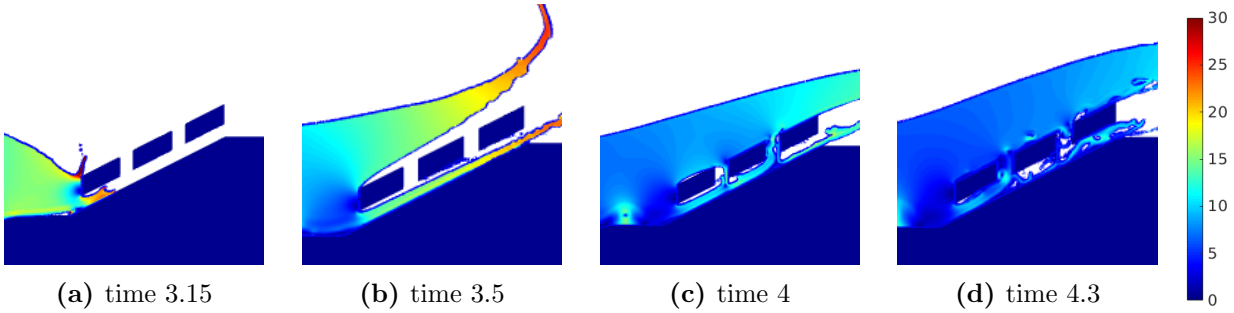

(a) time 3.15 **(b)** time 3.5 **(c)** time 4 **(d)** time 4.3

Figure 37: Structure 4 collision dynamics.

This simulation shows that a smaller upward redirection of the fluid increases the possibility for turbulent flow to occur. However, it barely reduced the overtopping, as the movement of the main mass of water is not disrupted. Although this design did not prove effective, it allowed us to understand the collision dynamics further.

6.4 Height difference between the blocks

As discussed in Subsection 6.2, a larger size of the roughness elements is more effective in reducing the overtopping. However, in the previous design referred to as Structure 3, the wave only collided with the first block, using it as a ramp. The water shoot around the element, and the latter two blocks turned ineffectual. Hence, the incentive for this subsection is to modify the design to increase the relevance of the other roughness elements. This is done through the study of height difference between consecutive blocks. Two designs, based on Structure 3, are considered, where the height of each roughness element is modified.

In the first design, called Structure 5, a height difference of $0.25m$ has been incorporated. As visible in Figure 38, the closer a block is to the seaside, the shorter it is. The middle block has the same dimensions as the standard block in Structure 3, while the height of first and last elements has been modified.

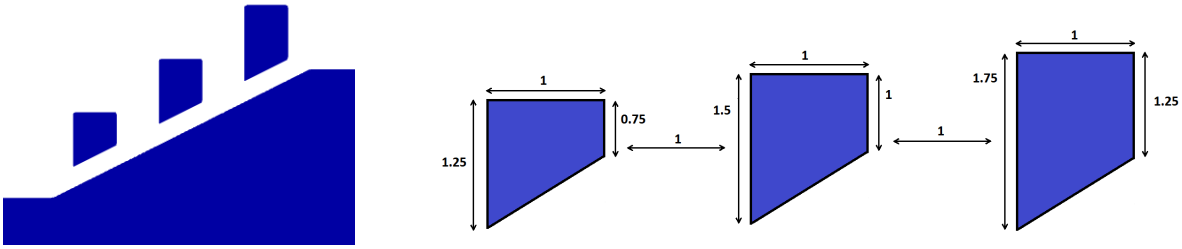

(a) Design of the roughness elements. **(b)** Dimension of the blocks.

Figure 38: Structure 5

A similar pattern has been used in the other design, referred to as Structure 6. However, the height difference of consecutive blocks has been increased to $0.5m$, as visible in Figure 45.

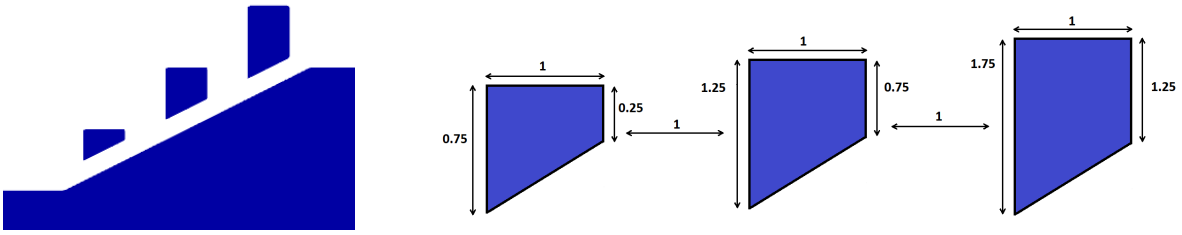

(a) Design of the roughness elements. **(b)** Dimension of the blocks.

Figure 39: Structure 6

The overtopping measurements for both designs are visible in Figure 40. As a reminder, for the previously discussed Structure 3, that has blocks of the same height, the amount of water over the

dike reached $8m^3$. By comparison, it can be deduced that a height difference between the blocks does not necessarily improve the design. For Structure 5 the amount of liquid has increased, to approximately $9.5m^3$. On the other hand, the height difference of $0.5m$ (Structure 6) has reduced the overtopping to less than $7m^3$.

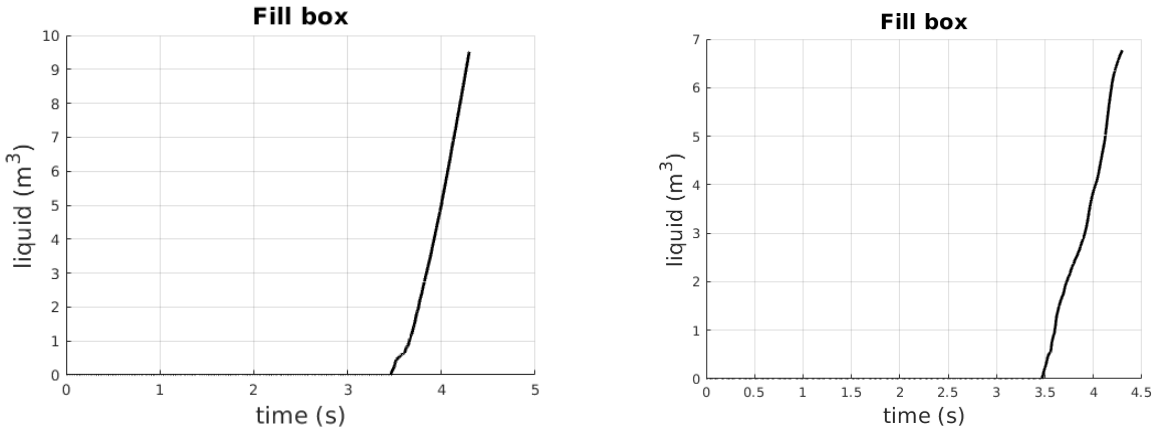

(a) Structure 5 **(b)** Structure 6

Figure 40: Overtopping measurement for Structure 5 and Structure 6.

Next, let us consider the horizontal hydrodynamic forces acting on the structures. The corresponding data from the force box is visible in Figure 41. For the design with a smaller height difference of the blocks, the maximum value of approximately $6.5 \times 10^5 N$ is obtained at a singular point near time $3.15s$. Another small rise in force is observed after the time $4s$, which suggests another collision with the wave. On the other hand, the maximum force acting on Structure 6 is around $4.7 \times 10^5 N$, which is a slightly smaller value in comparison to the other design. However, the force of this magnitude is observed twice throughout the simulation, and other smaller peaks appear later on. This behavior suggests, that the water crashes against the roughness elements more frequently, making them more relevant. The confirmation of these dynamics can be observed in the corresponding simulation snapshots, depicted in Figure 44 and Figure 45.

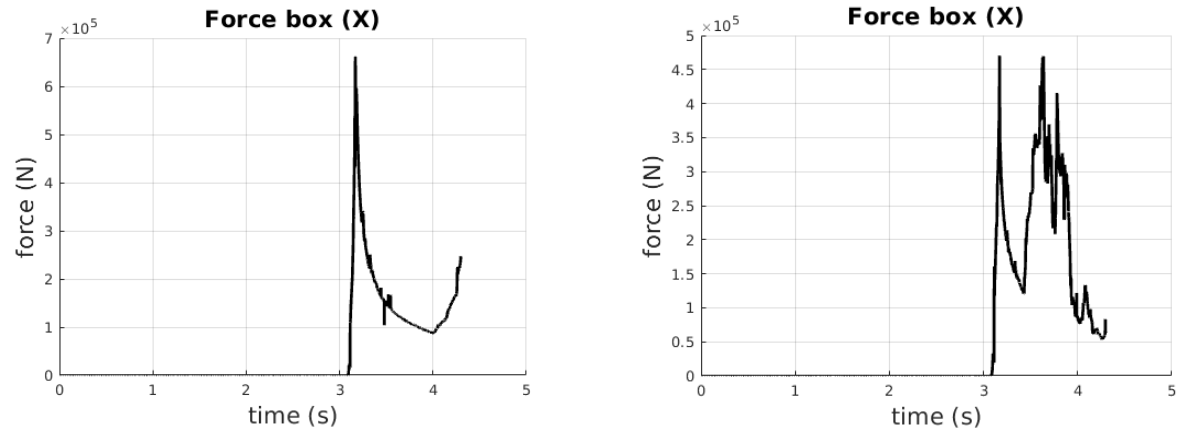

(a) Structure 5 **(b)** Structure 6

Figure 41: Horizontal hydrodynamic forces acting on Structure 5 and Structure 6.

The vertical force measurements are visible in Figure 42. For both designs, the maximal value is obtained around time $3.15s$. The value for Structure 6 is slightly higher, reaching $-16 \times 10^5 N$. Later on in the simulations, for the first design a small increase in force after time $4s$ is observed, while for the other design multiple oscillations are visible, suggesting a more turbulent flow.

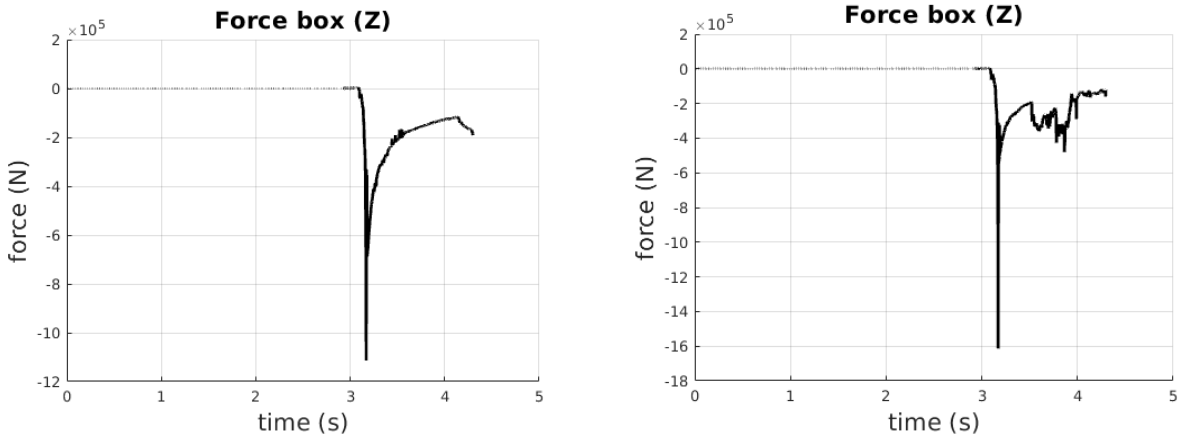

(a) Structure 5 **(b)** Structure 6

Figure 42: Vertical hydrodynamic forces acting on Structure 5 and Structure 6.

Next, the horizontal velocity measured at the monitor points is analyzed. The data is visible in Figure 43. At the first monitor point, the pattern for both designs is very similar, with a small difference around time $3.7s$. There, a rise in the velocity is observed for Structure 6. At the second monitor point, there are many dissimilarities between the data. For Structure 5 most of the velocity function is smooth. On the other hand, there are many disruption observed for Structure 6, suggesting turbulent flow. This is confirmed by the simulation snapshots given in Figure 45. For the last monitor point, both of the plots include a large number of oscillations. However at the end time, the final velocity for Structure 5 is around $8m/s$, while for Structure 6, the value is much lower, being around $4m/s$. From this data it can be concluded that a big difference in height of the blocks incites turbulent flow in the 'free path' of the dike.

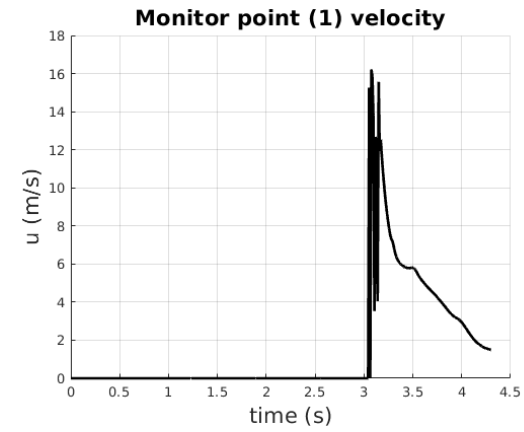

(a) Structure 5

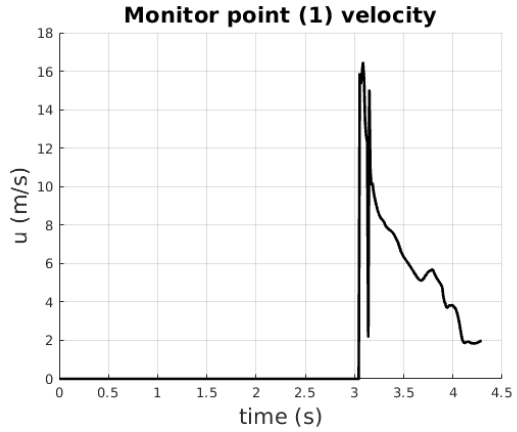

(b) Structure 6

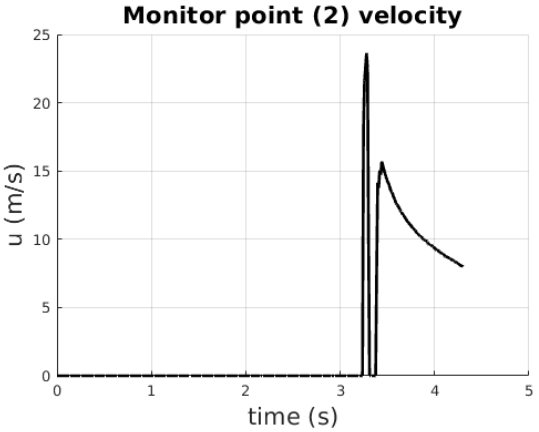

(c) Structure 5

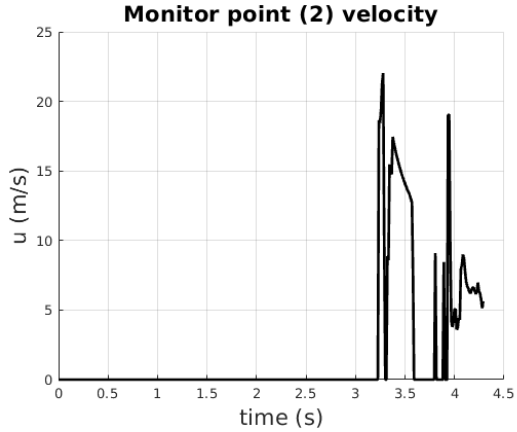

(d) Structure 6

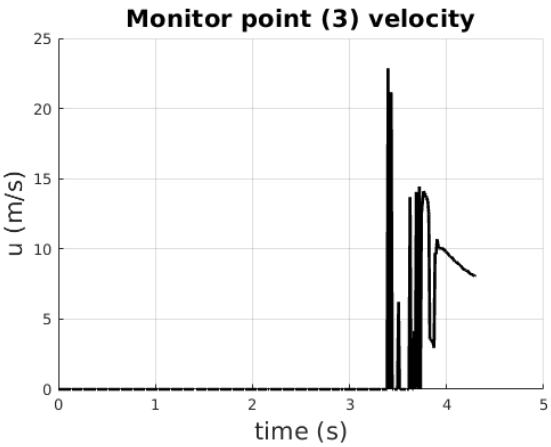

(e) Structure 5

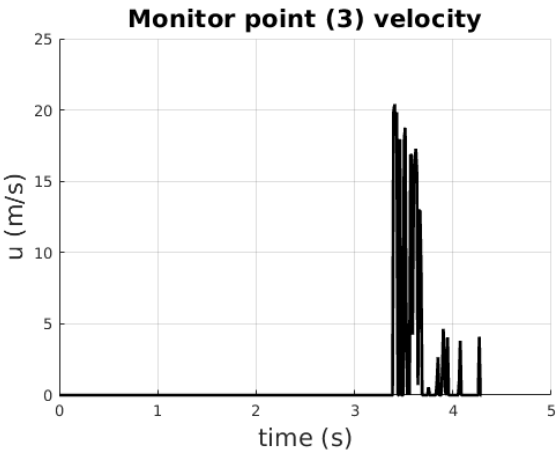

(f) Structure 6

Figure 43: Horizontal velocities at monitor points for Structure 5 and Structure 6.

Finally, let us consider the collision dynamics for both designs. As before, the coloring of the plots is based on the absolute velocity on a scale 0 to 30.

The snapshots for Structure 5 are given in Figure 44. The flow of the water resembles the one observed for Structure 3. The first block acts as a ramp for the wave, causing the fluid to go around

it. The line of droplets, visible in Figure 44b, is a numerical error with only a negligible effect on the flow. The numerical errors are discussed in Section 7. Due to the smaller height of the first block, the water mass is directed less upward than in Structure 3. Because of that and the increased height of the other two blocks, the falling water reaches the other roughness elements sooner. It causes a collision visible in the last snapshot 44d.

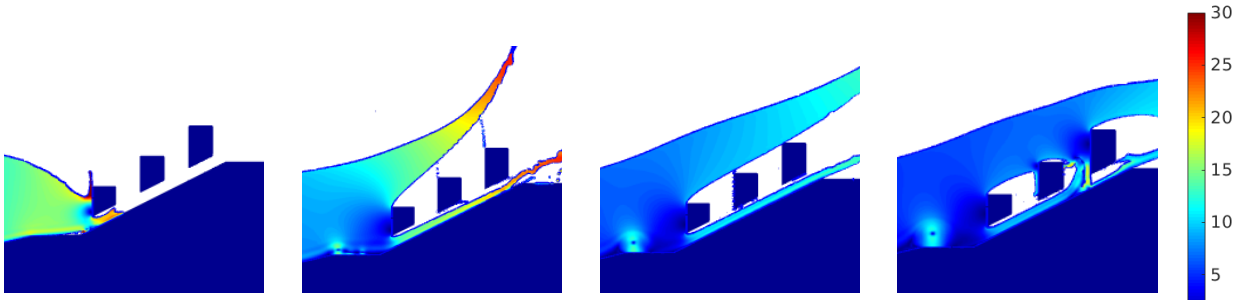

(a) time 3.15 **(b)** time 3.5 **(c)** time 4 **(d)** time 4.3

Figure 44: Structure 5 collision dynamics.

The effect of a bigger height difference of the blocks on the flow is visible in Figure 45. The first roughness element does not significantly redirect the wave. Because of that, and the increased height of the later blocks, the water collides with these, rather than fall on them from the top. This is visible in Figure 45b, where the fluid connects with top left corners of the other roughness elements. This causes a highly turbulent flow, which breaks down the structure of the wave. This has an especially big effect on the water traveling through the 'free path', as only droplets of the fluid reach the crest.

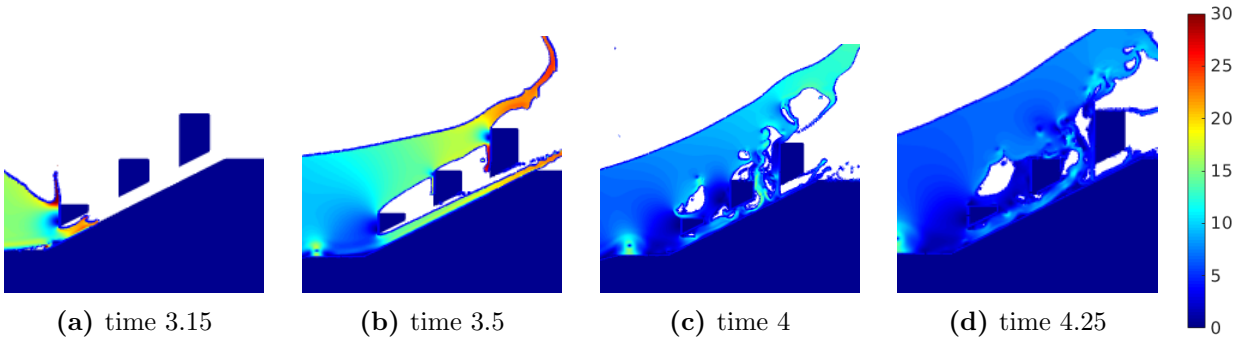

(a) time 3.15 **(b)** time 3.5 **(c)** time 4 **(d)** time 4.25

Figure 45: Structure 6 collision dynamics.

From this subsection, it can be deduced that the height difference of consecutive roughness elements has an influence on the efficiency of the design. For both of the considered designs, it increased the relevance of the latter two blocks. However, the data suggests that only a big height difference, such as the one considered in Structure 6, has a positive effect on the reduction of wave overtopping.

6.5 Width of blocks

The next query, is how the width of the blocks affects their efficiency. It is anticipated that the width has influence an on the forces acting on the structure, but not much effect on other parameters.

This claim is studied through the consideration of two designs. Both are based on Structure 3, where the only modified characteristic is their width. Recall, that the width of the blocks for that design was $1m$. Furthermore, note that the applied change has an effect on the location of the elements and the distance between them.

The first design, Structure 7, has three roughness elements of width $0.5m$, as visible in Figure 46.

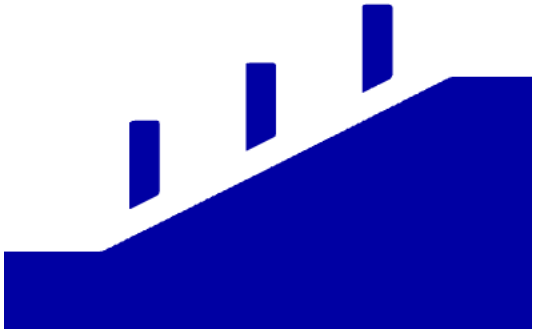

(a) Design of the roughness elements.

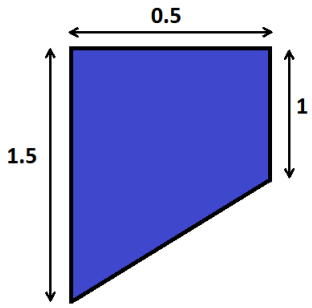

(b) Dimension of the blocks.

Figure 46: Structure 7

The second design, referred to as Structure 8, consists of blocks of width $1.5m$. Due to an occurrence of a numerical error, initially described in Section 7, the alternative computational mesh depicted in Figure 17 was used for this simulation.

(a) Design of the roughness elements.

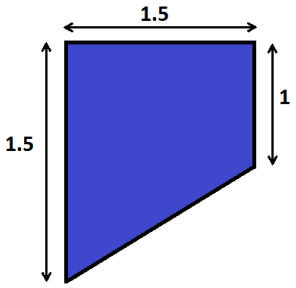

(b) Dimension of the blocks.

Figure 47: Structure 8

The overtopping measurements, visible in Figure 48, appear to be identical. The only minimal difference that can be spotted, is that Structure 8 has a slightly larger final amount by approximately $0.2m^3$. As such, it can be concluded that the width does not have a significant influence on the effectiveness of reducing the overtopping.

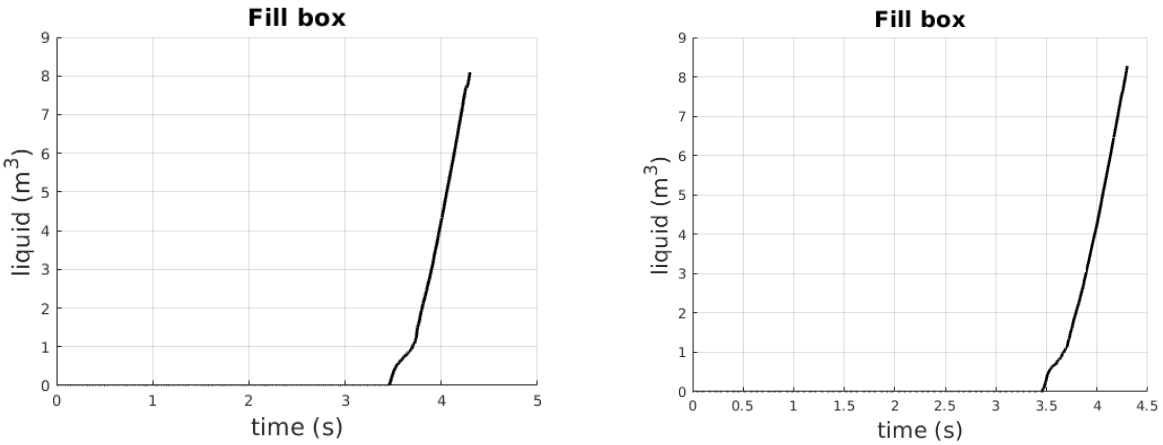

(a) Structure 7 **(b)** Structure 8

Figure 48: Overtopping measurement for Structure 7 and Structure 8.

As mentioned, the parameters of interest for this subsection are the hydrodynamic forces acting on the structure.

Firstly, let us consider the horizontal forces, for which the data is depicted in Figure 49. The shape of both functions appears to be identical. The only dissimilarity is the magnitude of the peak, which for Structure 7 is $9 \times 10^5 N$ and for Structure 8 is $7 \times 10^5 N$.

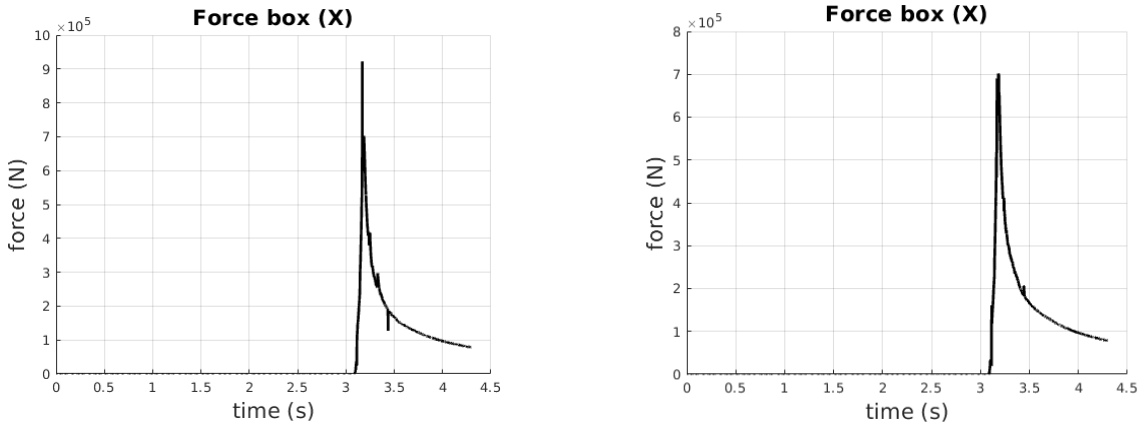

(a) Structure 7 **(b)** Structure 8

Figure 49: Horizontal hydrodynamic force acting on Structure 7 and Structure 8.

Similar observation can be made regarding the vertical forces, depicted in Figure 50. The general pattern is the same, with the only difference being the magnitude of the maximal force. For Structure 7 it reached approximately $-2.2 \times 10^6 N$, while for Structure 8 it is $-1.4 \times 10^6 N$.

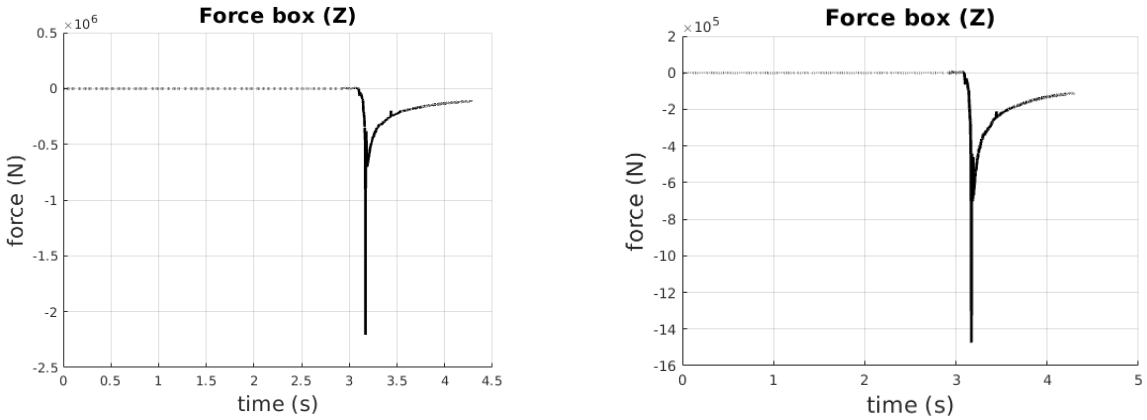

(a) Structure 7 **(b)** Structure 8

Figure 50: Vertical hydrodynamic force acting on Structure 7 and Structure 8.

From the analysis of the data obtained from the force boxes, it can be deduced that while the width of the blocks has an influence on the magnitude of the hydrodynamic forces acting on the structures, the effect is not significant. However, it should be acknowledged, that a wider block implies that the forces acting on a block are more spread out. For that reason, in real life, a wider block is able to sustain more stress.

The next component of the study are the horizontal velocities of the water passing through monitor points. The measurements are given in Figure 51. For both structures, the results for corresponding points are the same in scale and shape. Therefore, the width of the block does not influence the speed of the water in the ‘free path’‘ of the dike.

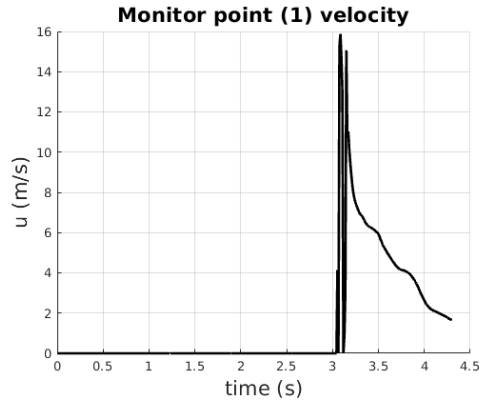

(a) Structure 7

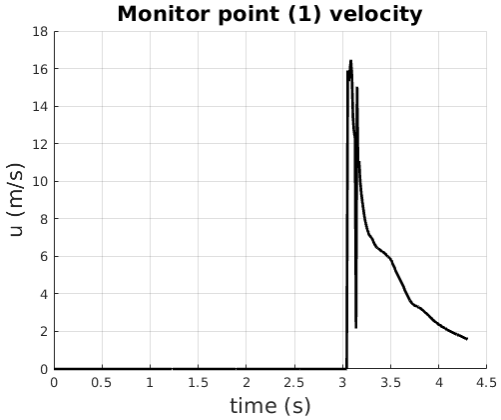

(b) Structure 8

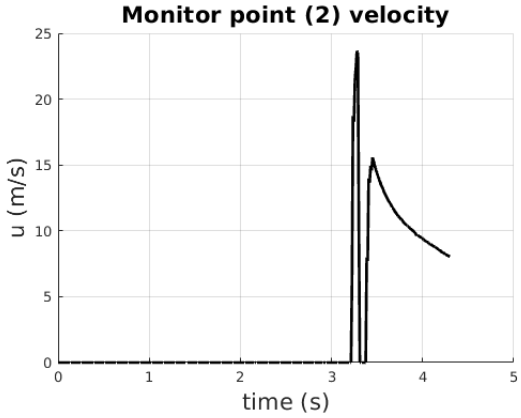

(c) Structure 7

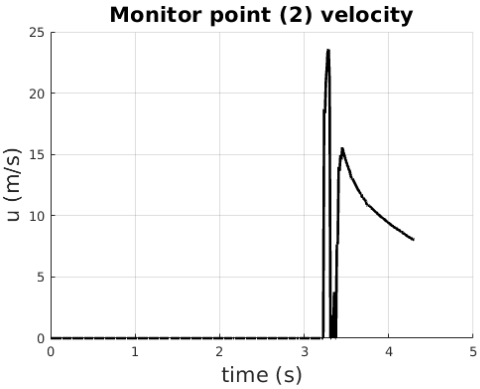

(d) Structure 8

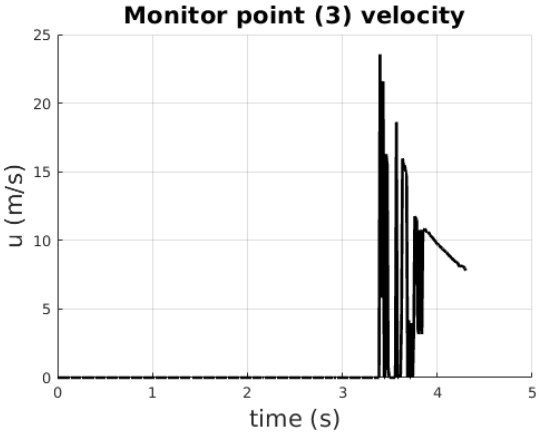

(e) Structure 7

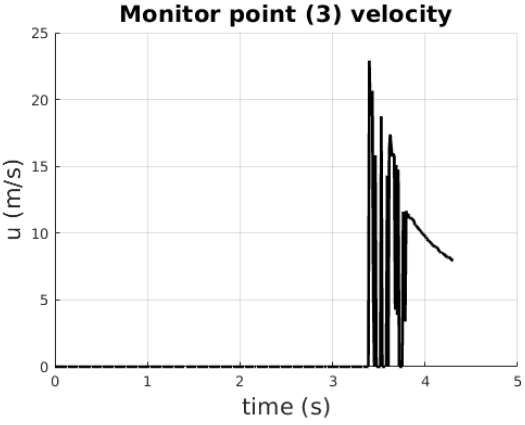

(f) Structure 8

Figure 51: Horizontal velocities measured at the monitor points for Structure 7 and Structure 8.

Finally, let us study the fluid dynamics around the considered roughness elements. The snapshots for Structure 7 are given in Figure 52, and those for Structure 8 in Figure 53. The collision dynamics for both cases are nearly identical. The wave collides with the first element, and flows around it. By eye, the angle at which the water is directed upwards is the same for both. The wave slowly drops, however an impact with the blocks placed higher up the slope does not occur.

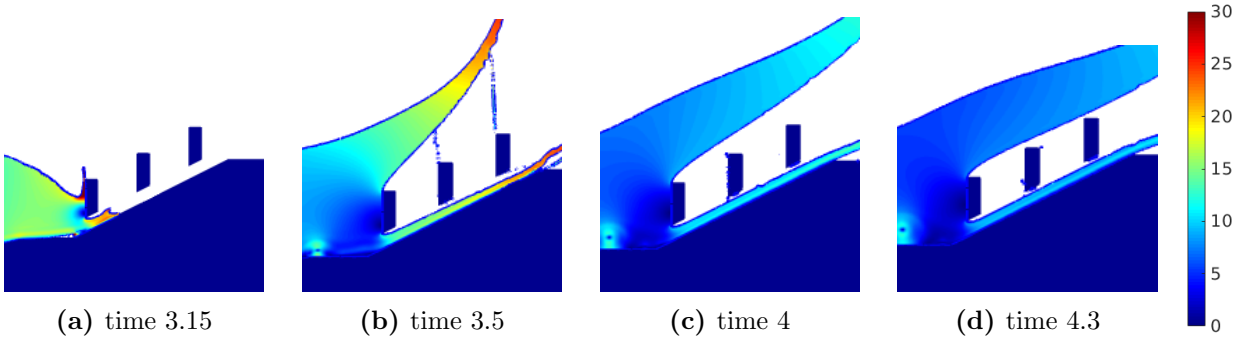

(a) time 3.15 **(b)** time 3.5 **(c)** time 4 **(d)** time 4.3

Figure 52: Structure 7 collision dynamics.

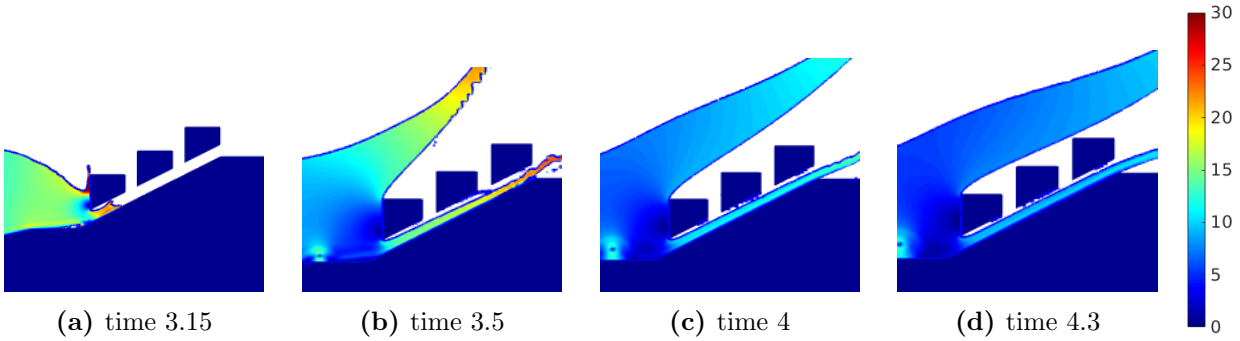

(a) time 3.15 **(b)** time 3.5 **(c)** time 4 **(d)** time 4.3

Figure 53: Structure 8 collision dynamics.

It can be concluded that the width of the roughness elements does not have a big effect on the water dynamics or on the reduction of overtopping. It has a small influence on the magnitude of the hydrodynamic forces experienced. Although this is not fully obvious from the obtained results, it makes sense for blocks to be wide, as the applied stress can spread over a larger volume. As the roughness elements are meant to last prolonged periods of time, it is crucial to ensure that they are able to sustain higher forces applied to them, without any breakage of the structure. Nonetheless, as the modified width did not result in a significant improvement, the standard width of $1m$ is used for later designs.

6.6 Distance between the blocks

An important characteristic of a dike design is the placement of the roughness elements. Even if the shape is unchanged, the efficiency of the structure can alter. To study this phenomenon, a new design is considered, which is based on Structure 3. To compare the effects of the modification more easily, the data previously discussed in Section 6.2 is included once again.

For Structure 3, the blocks are placed $1m$ away from each other, as depicted in Figure 54.

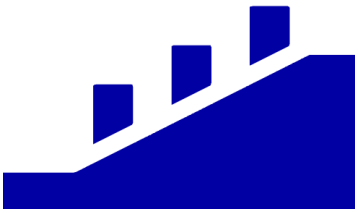

(a) Design of the roughness elements.

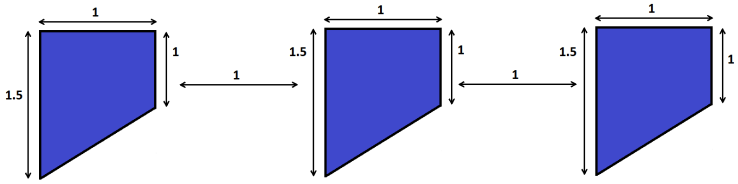

(b) Distance between the blocks.

Figure 54: Structure 3

For the new design, called Structure 9, the distance between the roughness elements is increased to $1.5m$. With this, the first and last block are moved closer to the endpoints of the upper seaward slope, while the position of the middle block is unchanged. Furthermore, the extended computational grid, given in Figure 17, has been used for this simulation due to numerical errors occurring during an initial simulation.

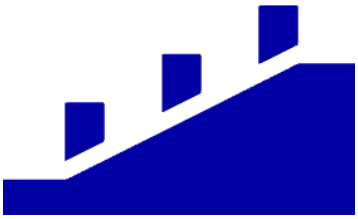

(a) Design of the roughness elements.

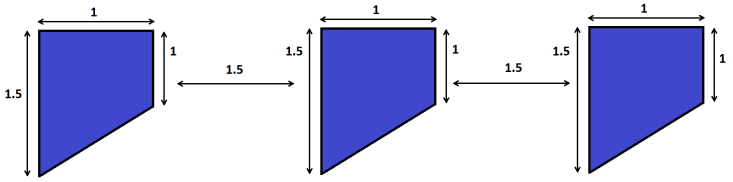

(b) Distance between the blocks.

Figure 55: Structure 9

Firstly, let us study how the change of the design affects the overtopping. The data for Structure 3 and Structure 9 is given in Figure 56. The shape of the functions is very similar, however the final amount of fluid is larger for Structure 9, by about $1m^3$. This result suggests that the increased distance between the blocks is not beneficial.

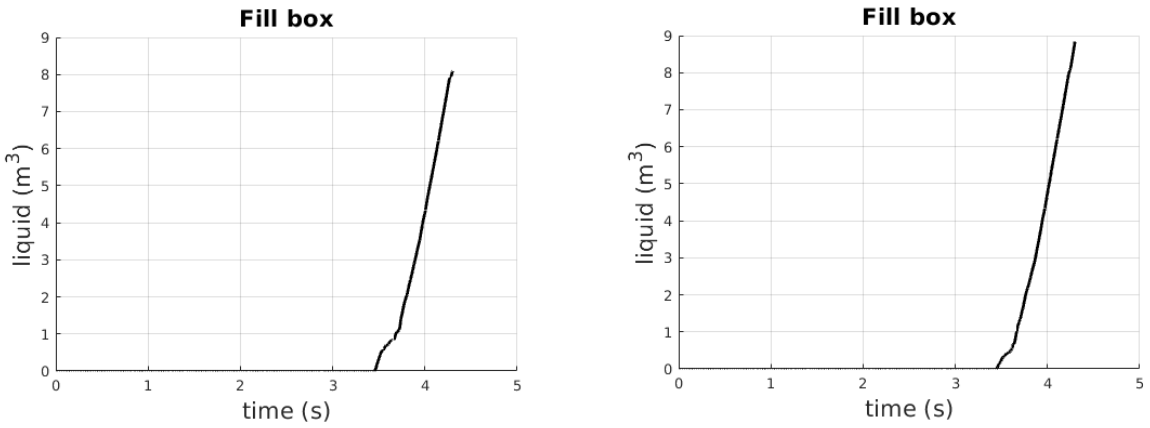

(a) Structure 3 **(b)** Structure 9

Figure 56: Overtopping measurement for Structure 3 and Structure 9.

The measurements for the horizontal hydrodynamic force acting on the structures is given in Figure 57. The main shape of both functions is similar, however there are more disruptions to the force detected for Structure 9. For example, there is a singular high value peak around the time $3.4s$. Due to the sudden occurrence of the peak lasting only one time step, it is suspected that it could be a result of a numerical error. Otherwise, the force registered for the Structure 3 appears to be slightly higher at the initial stage. At the end, a small rise is visible for Structure 9, suggesting a collision of the wave with another block.

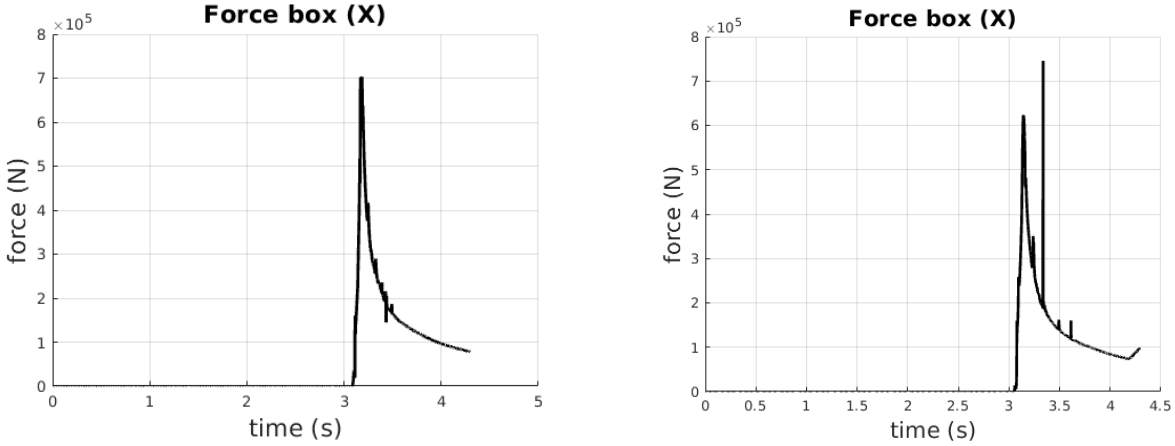

(a) Structure 3 **(b)** Structure 9

Figure 57: Horizontal hydrodynamic force acting on Structure 3 and Structure 3.

The measurement of the vertical forces is given in Figure 58. The shape of the functions is similar, however the magnitude of the force is larger for Structure 3. For both designs, there are negligible disruptions appearing around time $3.5s$.

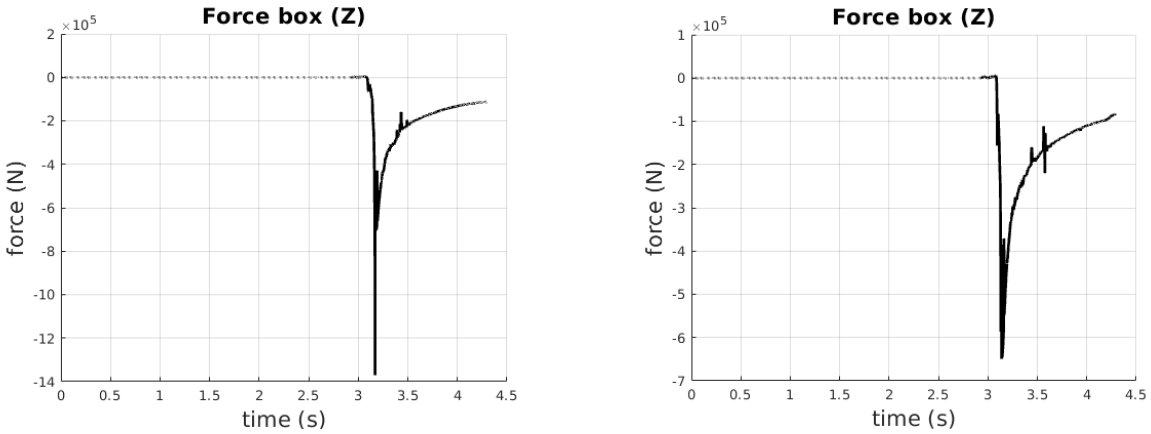

(a) Structure 3 **(b)** Structure 9

Figure 58: Vertical hydrodynamic force acting on Structure 7 and Structure 8.

Next, let us analyze the horizontal velocities of water passing through the monitor points. The data is depicted in Figure 59. For the first monitor point there is a clear difference between the results. The average velocity obtained for Structure 9 is higher, and its value decreases at a slower rate. A probable cause for this behavior is the placement of the first roughness element. Similarly, at the second monitor point, the latter design achieves a higher peak value, of around $27m/s$. However, after that, Structure 3 attains a larger velocity, with a secondary peak reaching $15m/s$. Finally, for the last monitor point, the results for both simulations are the same in terms of pattern and magnitude. From the considered data, it can be concluded that the location of the elements has an effect on the fluid flow. However it is not clear which one is more beneficial, in terms of slowing down the water running up the slope.

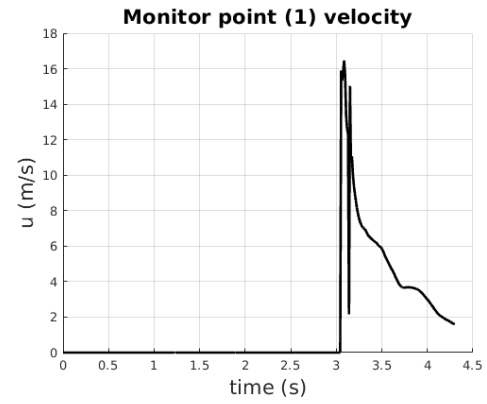

(a) Structure 3

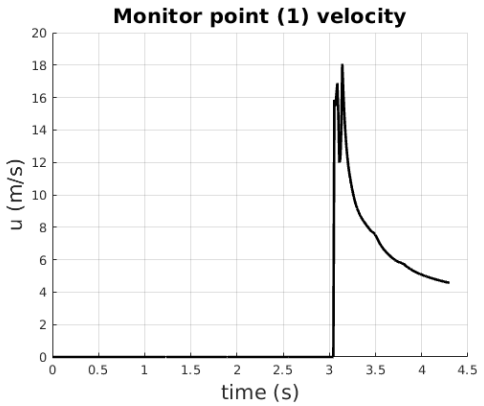

(b) Structure 9

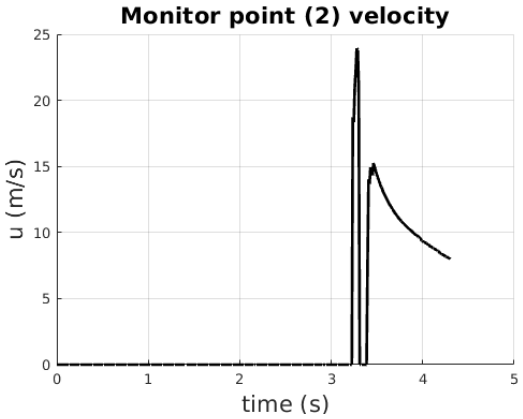

(c) Structure 3

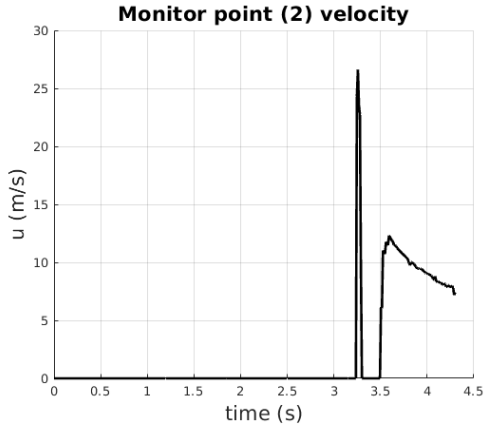

(d) Structure 9

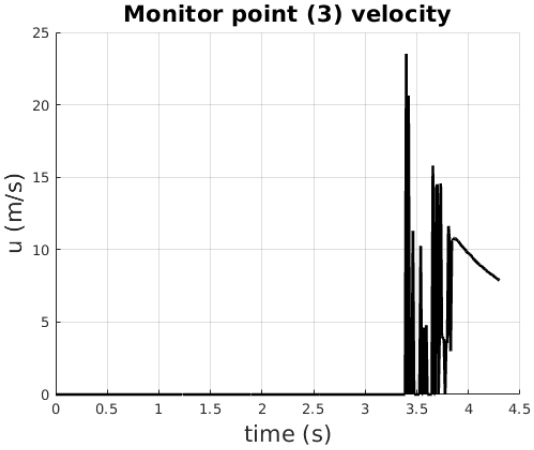

(e) Structure 3

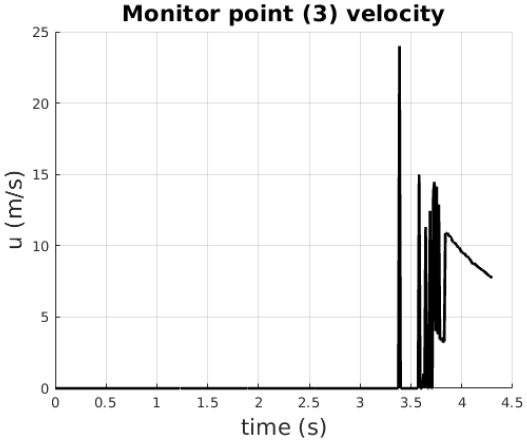

(f) Structure 9

Figure 59: Horizontal velocity measured at the monitor points for Structure 3 and Structure 9.

Lastly, the snapshots from the considered simulations are given in Figures 60 and 61. As the dynamics of Structure 3 were discussed in detail in Section 6.2, in this section they are only used for comparison purposes. As the first block of Structure 9 has been moved towards the start of the seaward slope, at time $3.15s$ the impact of the water is greater. However, after that point the difference between both simulations, for times $3.5s$ and $4s$, is minimal. Only near time $4.25s$, the

wave drops down onto Structure 9, causing another collision. As such, it can be deduced that the distance between the blocks has some effect on the fluid flow. Furthermore, a numerical error in the form of a line of droplets can be seen for both simulations at the $3.5s$ snapshot. As it does not effect the main fluid flow, it can be neglected. A more detailed discussion about the numerical errors is in Section 7.

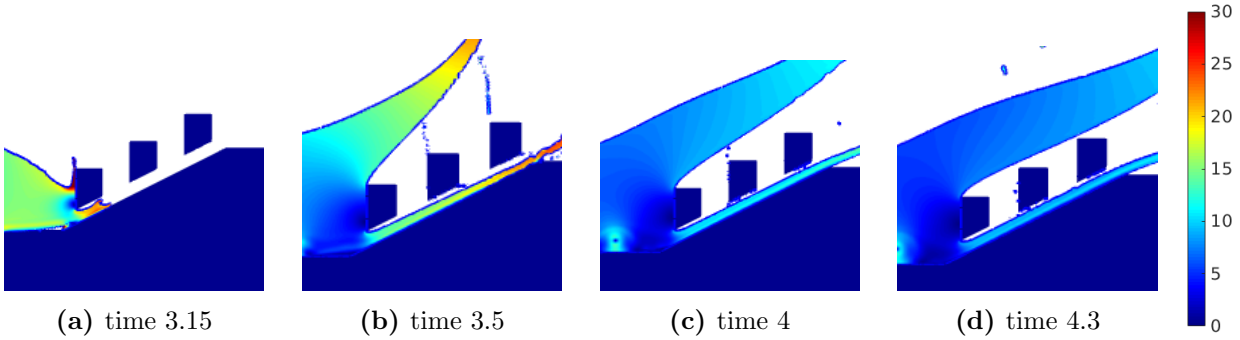

(a) time 3.15 **(b)** time 3.5 **(c)** time 4 **(d)** time 4.3

Figure 60: Structure 3 collision dynamics.

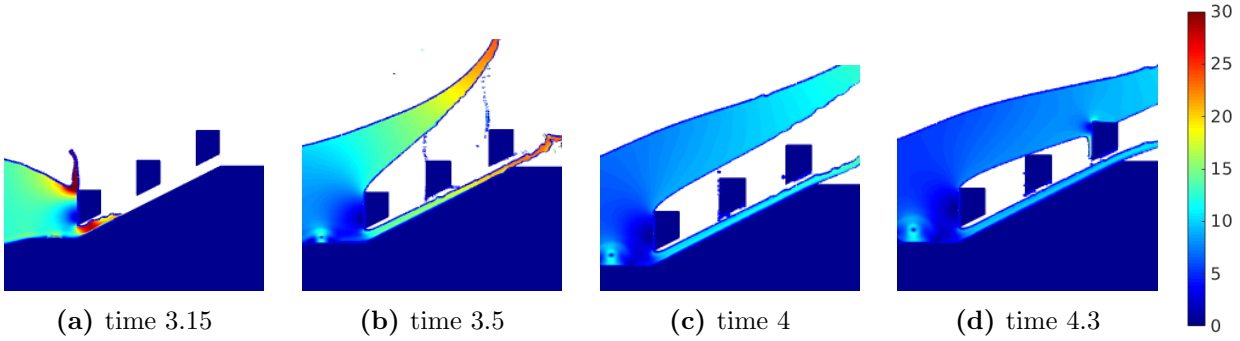

(a) time 3.15 **(b)** time 3.5 **(c)** time 4 **(d)** time 4.3

Figure 61: Structure 9 collision dynamics.

From the analyzed data, it can be concluded that the larger distance between the roughness elements has an effect on the solution. However, it is not necessarily increasing the efficiency of the design. Instead, the overtopping measure is larger. Therefore, the increased distance between the blocks is considered an ineffective modification.

6.7 Placement of the middle block

To further improve the efficiency of the design, in this section a non equidistant placement of the roughness elements is considered. Structure 6, previously analyzed in Section 6.4, has the highest influence of the blocks from all the previous simulations due to their height difference. As such, the new designs studied in this section are based on that structure. The location of the middle block has been modified, to vary the distance between consecutive elements.

In Structure 10, visible in Figure 62, the middle block has been moved $0.5m$ towards the bottom of the seaward slope. With this, the distance between the latter two blocks is $1.5m$.

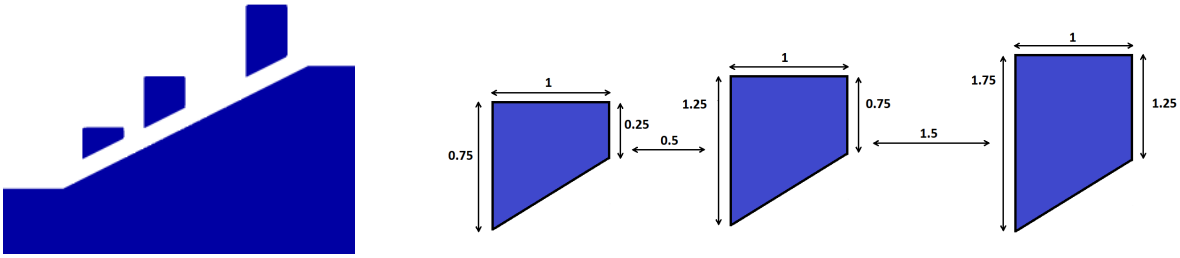

(a) Design of the roughness elements. **(b)** Dimension of the blocks.

Figure 62: Structure 10

Similarly, in Structure 11, the middle block has been placed $0.5m$ towards the crest, as depicted in Figure 63.

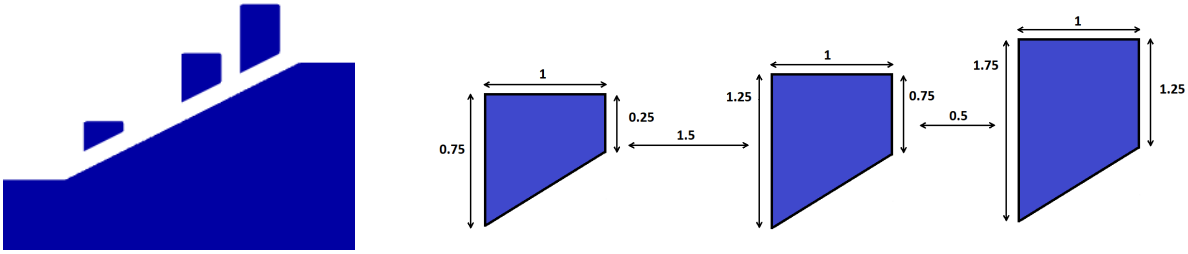

(a) Design of the roughness elements. **(b)** Dimension of the blocks.

Figure 63: Structure 11

This modification had a small influence on the overtopping for both structures, as visible in Figure 64. Recall, that for Structure 6 the final value was approximately $6.8m^3$. The placement of the middle block towards the seaside had a negative effect, increasing the amount of fluid in the fill box to over $8m^3$. On the other hand, Structure 11 has turned out be me more effective, as the overtopping has decreased to around $6.5m^3$.

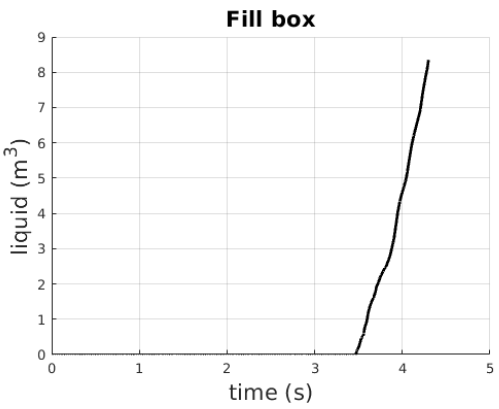

(a) Structure 10

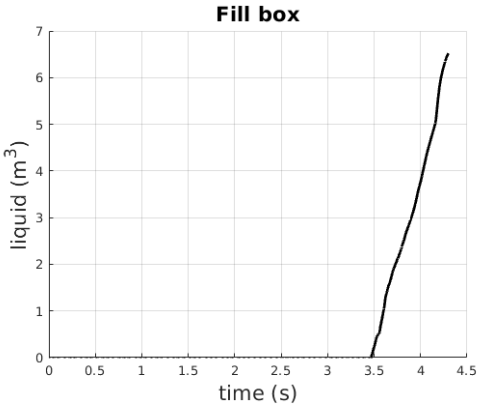

(b) Structure 11

Figure 64: Overtopping measurement for Structure 10 and Structure 11.

The horizontal hydrodynamic forces are given in Figure 65. The pattern and magnitude of both measurements is very similar, except for the last second of the simulation. For Structure 11 an additional rise in the force is registered around time $4s$, suggesting a higher amount of collisions in the last phase of the simulation. Instead, for Structure 10 there is only a small disruption recorded after that time frame.

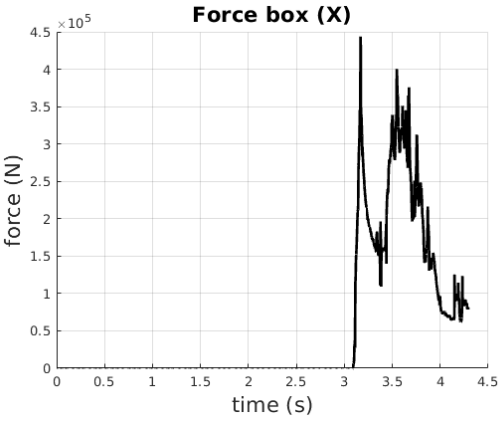

(a) Structure 10

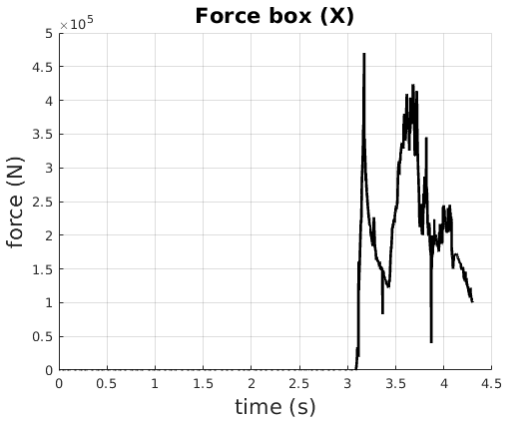

(b) Structure 11

Figure 65: Horizontal hydrodynamic force acting on Structure 10 and Structure 11.

The vertical force data is given in Figure 66. Both functions resemble each other in shape, however the scale of the initial peak differs. For Structure 10 the maximal value is around -11×10^5, while the other structure attains a higher magnitude of -16×10^5.

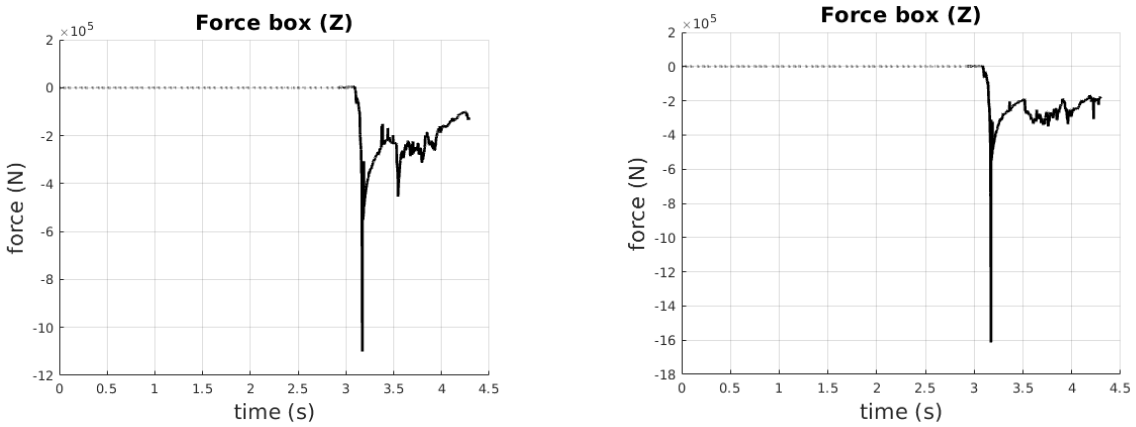

(a) Structure 10 **(b)** Structure 11

Figure 66: Vertical hydrodynamic force acting on Structure 7 and Structure 8.

The similarity of the results can also be seen for the horizontal velocities measured at the monitor points. The obtained data is given in Figure 67. At the first point, the shape and scale of the functions is almost identical. The only dissimilarity is for Structure 11, where a small rise in velocity is registered around time $3.7s$. At the second monitor point the magnitude of the first peak is the same for both simulations. It appears that there is less fluid passing through the 'free path' of Structure 10 around time $3.5s$, which suggests a big disruption to the flow. Furthermore, there appears to be a spike of negative velocity, which implies fluid traveling in the opposite direction. A similar occurrence of backflow can also be observed for Structure 11, along with many oscillations throughout the last second of the simulation. For the last monitor point the data shows multiple spikes. As such, it can be deduced that the water passing through had the form of many droplets. The results for both structures indicate a highly turbulent flow, which can be considered a positive point.

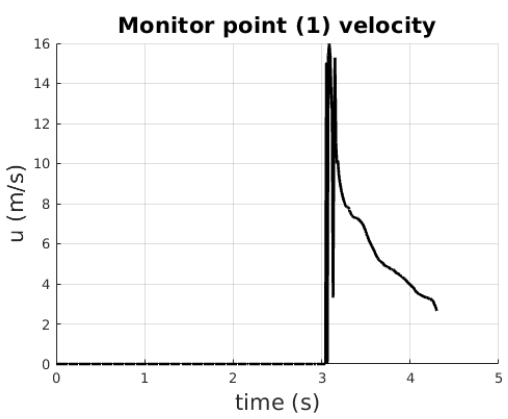

(a) Structure 10

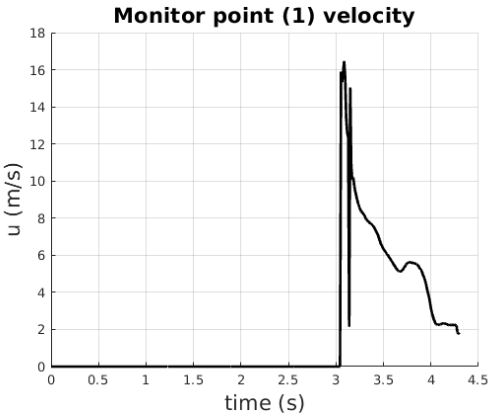

(b) Structure 11

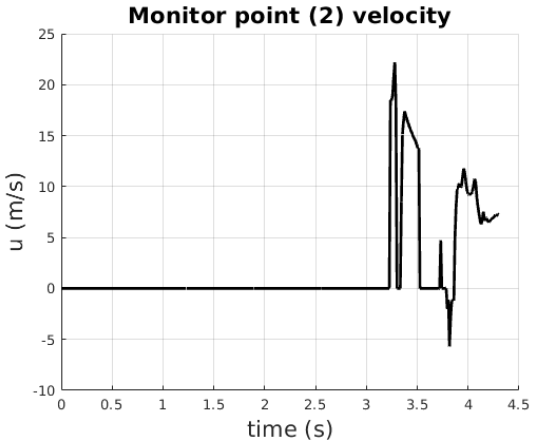

(c) Structure 10

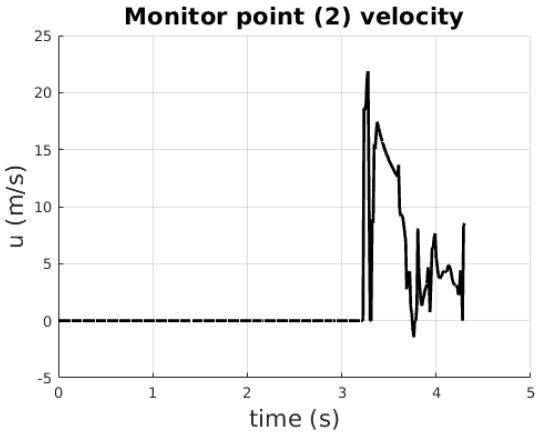

(d) Structure 11

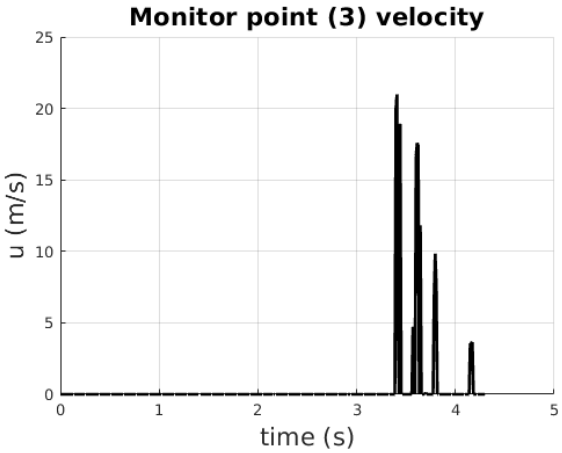

(e) Structure 10

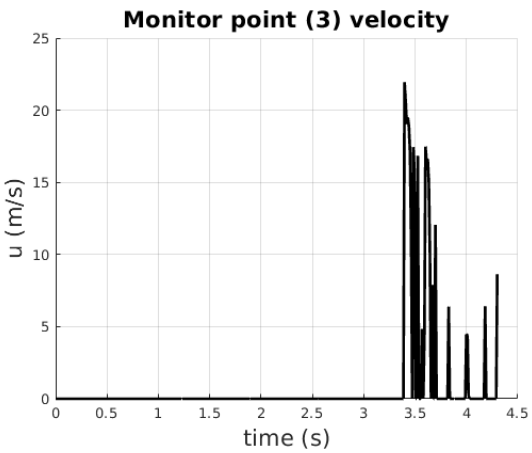

(f) Structure 11

Figure 67: Horizontal velocity measurements at the monitor points for Structure 10 and Structure 11.

The collision dynamics for Structure 10 and Structure 11 are given in Figure 68 and Figure 69, respectively. The movement of the fluid is analogous in both simulations. At time $3.15s$ an impact on the first roughness element is visible. The water is redirected around it, to subsequently collide

with other blocks soon after. For Structure 10 the wave bounces off the middle element, before hitting the last one. On the other hand, for Structure 11 the water passes above the second block and impacts with the wall of the final element. For both simulations, the collisions incite a highly turbulent flow visible at time $4s$ and $4.3s$. A high amount of splatter is considered beneficial, as the wave energy is less directed. Furthermore, the chaotic trajectory reduced the fluid passing through the 'free path'.

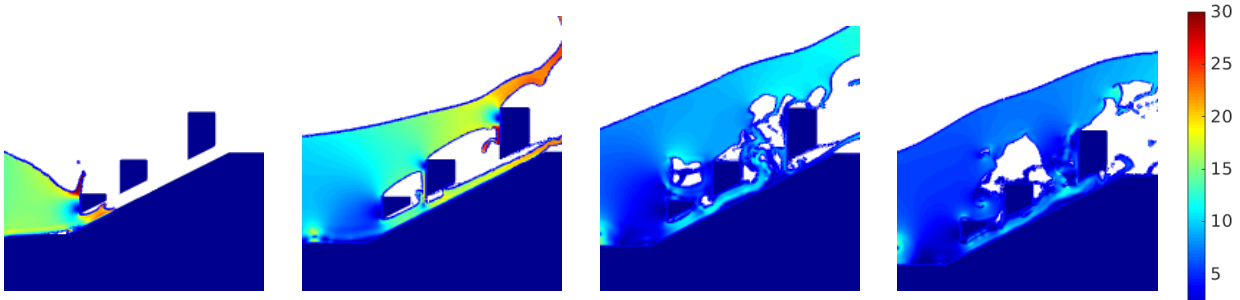

(a) time 3.15 **(b)** time 3.5 **(c)** time 4 **(d)** time 4.3

Figure 68: Structure 10 collision dynamics.

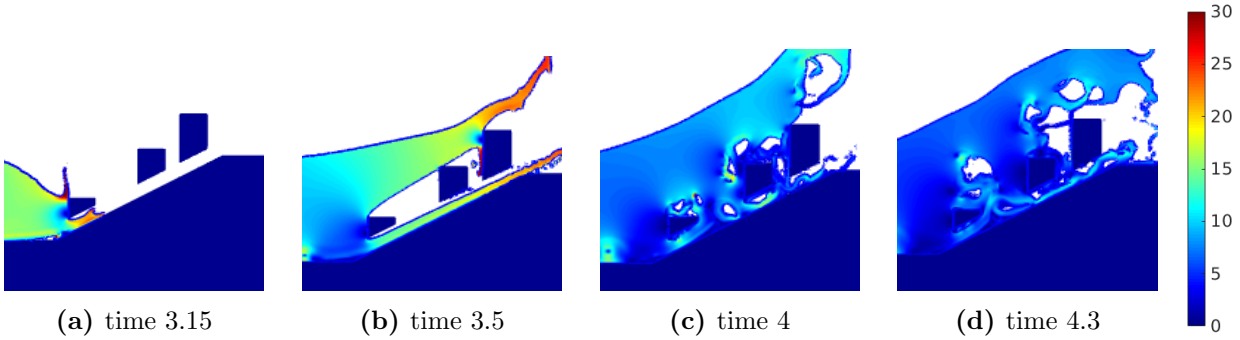

(a) time 3.15 **(b)** time 3.5 **(c)** time 4 **(d)** time 4.3

Figure 69: Structure 11 collision dynamics.

Summary

The results analyzed in this section verify the influence of the position of the middle block on the overall effectiveness of the structures. From the overtopping measurements it seems that placing the second roughness element closer to the crest is beneficial. However, the simulation snapshots for that structure show that the wave does not actually impact the block in the initial phase. This observation suggests that the second roughness element may not improve the efficiency of the design. This is studied further in the next Section 6.8.

6.8 Relevance of first two blocks

The collision dynamic observed for Structure 11 from Section 6.7 suggested that the middle roughness element may not be relevant or beneficial for the reduction of wave overtopping. In this subsection the assumption is investigated, and further extended to the practicality of the first block. Two designs are considered, which are based on Structure 6, introduced in Section 6.4. The applied

modification is the removal of the first two blocks. This allows to verify their functionality or lack thereof.

In Structure 12, visible in Figure 70, the second block is not included in the design. The dimensions or location of the other roughness elements has not been altered.

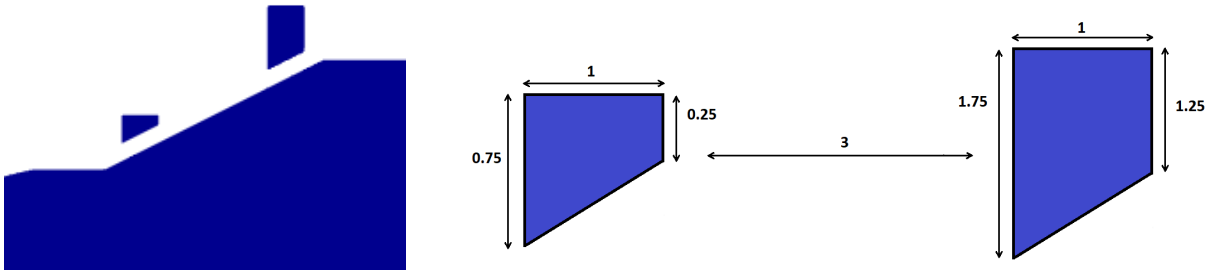

(a) Design of the roughness elements. **(b)** Dimension of the blocks.

Figure 70: Structure 12

In the other design considered, labeled as Structure 13, only the final roughness element is placed on the seaward slope. This is depicted in Figure 71. With this, the effect of the first block on the fluid flow can be studied.

(a) Design of the roughness elements. **(b)** Dimension of the blocks.

Figure 71: Structure 13

The overtopping measurements are visible in Figure 72. The previous best design, being Structure 11 from Section 6.7, has an overtopping of around $6.5m^3$. For the design without the middle block, there is a minimal improvement in the efficiency, as the final amount is around $6.2m^3$. On the other hand, for Structure 13 the fluid amount has been reduced to $4.7m^3$. This suggests that the lack of a roughness elements on the start of the seaward slope may be beneficial, however this claim is furthered discussed during the review of the collision dynamics.

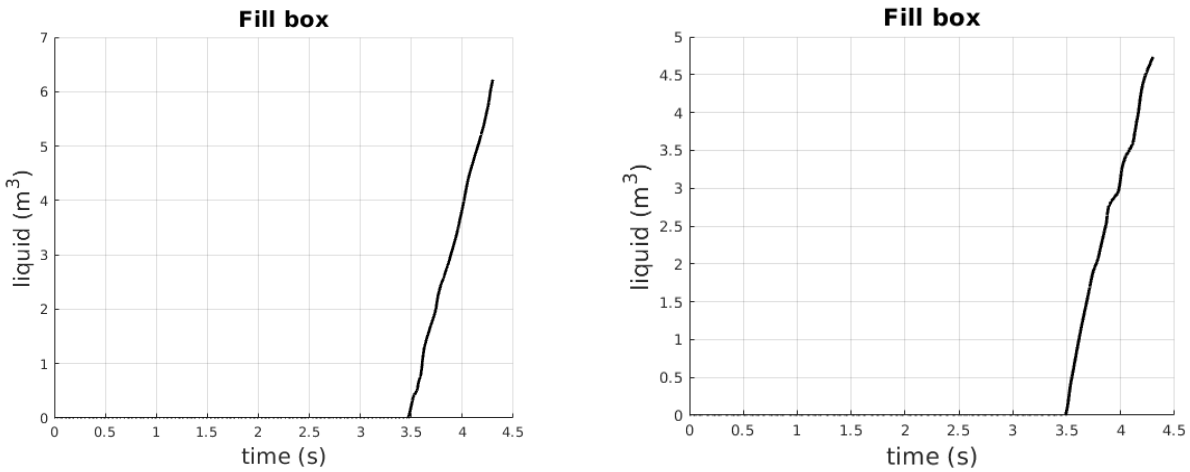

(a) Structure 12 **(b)** Structure 13

Figure 72: Overtopping measurement for Structure 12 and Structure 13.

The horizontal force readings, given in Figure 73, differ greatly in their shape. For Structure 12 we can observe multiple peaks , implying the occurrence of several collisions with the structure and a more chaotic flow. On the other hand, the force function for Structure 13 is rather a singular large peak, reaching the value of $4 \times 10^5 N$. After the time $3.5s$ the magnitude is slowly decreasing, with a few small disruptions to the force. This implies that the wave is traveling smoothly, until it impacts the large roughness element. Due to the lack of additional force peaks, the block only influences the flow during the initial collision.

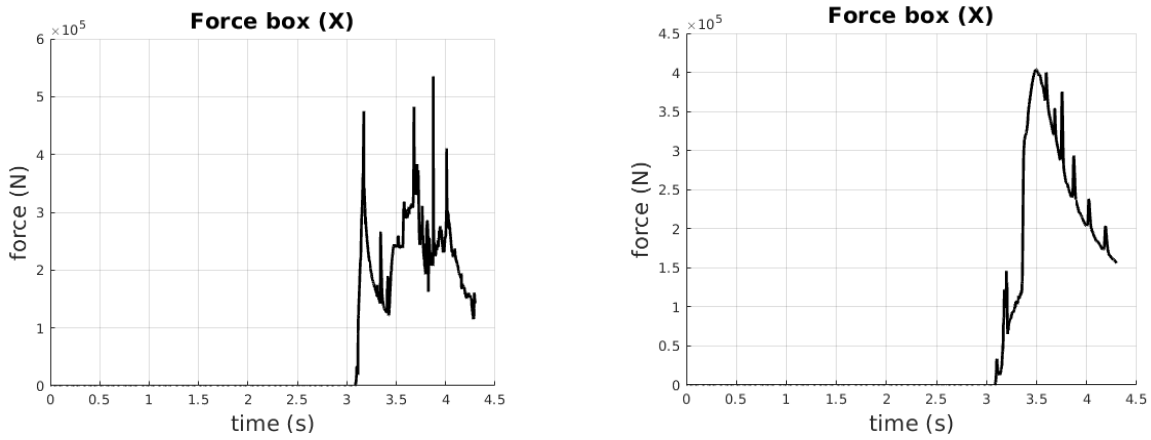

(a) Structure 12 **(b)** Structure 13

Figure 73: Horizontal hydrodynamic force acting on Structure 12 and Structure 13.

Similar behavior can be observed in the vertical force data, depicted in Figure 74. The force acting on Structure 13 consists of mostly one large peak. There are small disruptions to the force, however, they occur at singular points. On the other hand, Structure 12 has multiple wider force peaks, along a large singular peak around time $3.15s$. The majority of the forces acting on both structures have the same magnitude. The maximum values of Structure 12 are higher, however, as they are recorded at singular points, that could be caused by numerical errors.

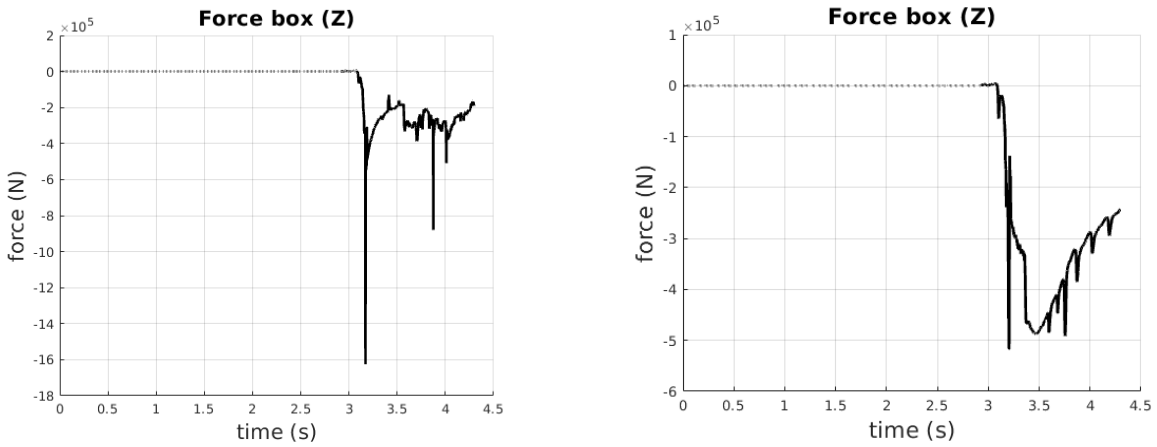

(a) Structure 12 **(b)** Structure 13

Figure 74: Vertical hydrodynamic force acting on Structure 12 and Structure 13.

The horizontal velocity of water flowing through the monitor points is given in Figure 75. At the first point, the average speed of water for Structure 12 is lower than that for Structure 13. The initial drop in magnitude goes down to almost $8m/s$ in the first simulation, and only to around $12m/s$ for the second one. At the second monitor point, there are no disruptions of the fluid for Structure 13, resulting in a smooth decrease of velocity. On the other hand, numerous small oscillations are visible for Structure 12. This implies that the initial block has affected the wave run up, causing some turbulence. Additionally, at the very end the recorded velocity is negative, implying the opposite direction of the flow. Finally, at the last monitor points both measurements consist of multiple peaks, of maximum velocity around $22m/s$. This suggests splashing of the wave.

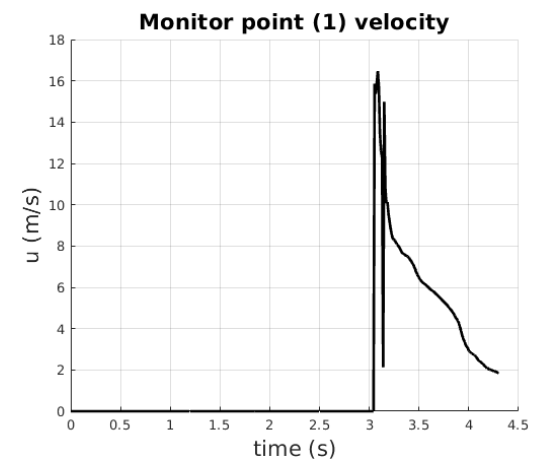

(a) Structure 12

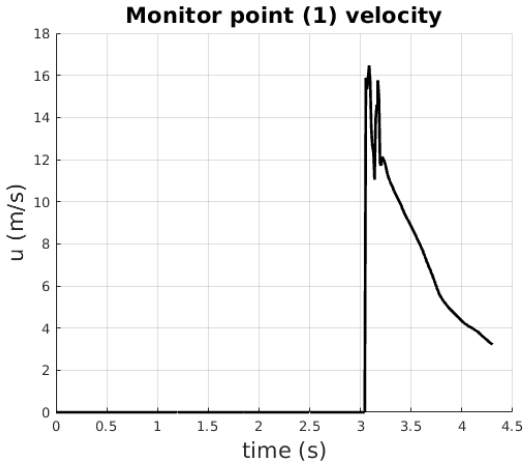

(b) Structure 13

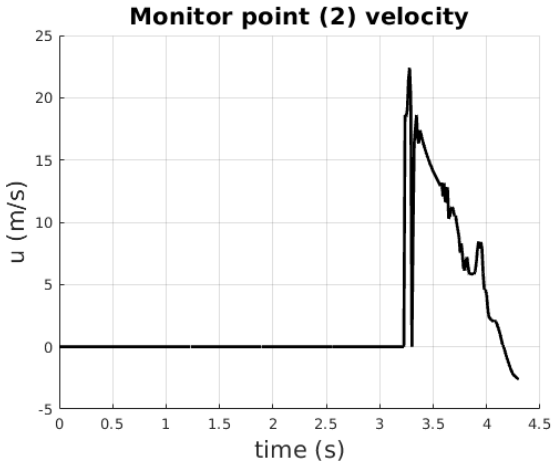

(c) Structure 12

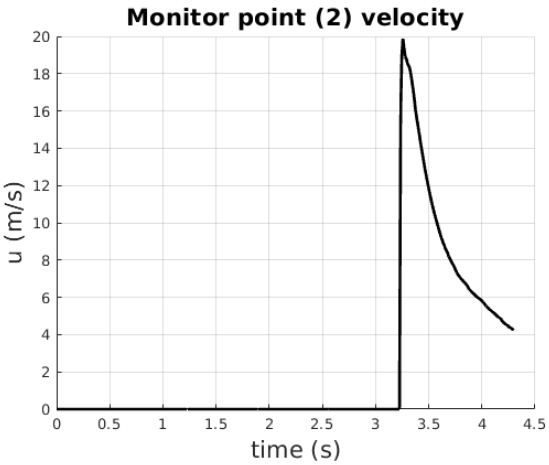

(d) Structure 13

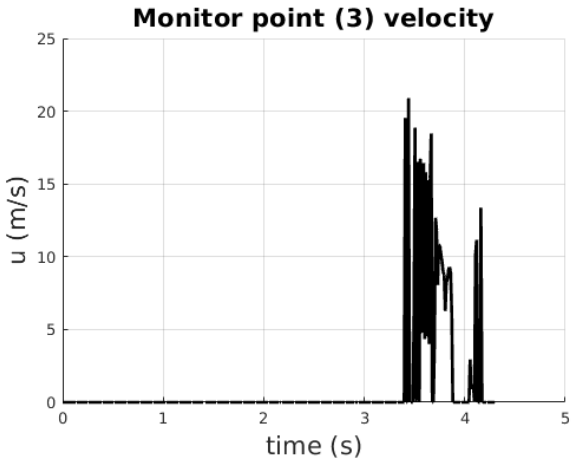

(e) Structure 12

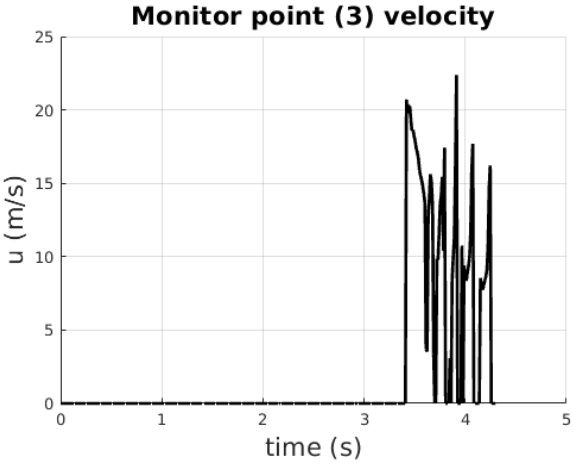

(f) Structure 13

Figure 75: Horizontal velocity measured at the monitor points for Structure 12 and Structure 13.

Finally, the collision dynamics for Structure 12 and Structure 13 are visible in Figure 76 and Figure 77, respectively. The colors of the plots are based on the average velocity, on a scale from 0 to 30.

For Structure 12, the initial impact at time 3.15s is comparable to previous simulations. As a result, the water runs around the block, almost using it as a short ramp. The ejected water hits the last block around 3.5s, which leads to a turbulent flow visible during the last two snapshots. This disrupts the water in the 'free path', reducing the amount of water that reaches the crest.

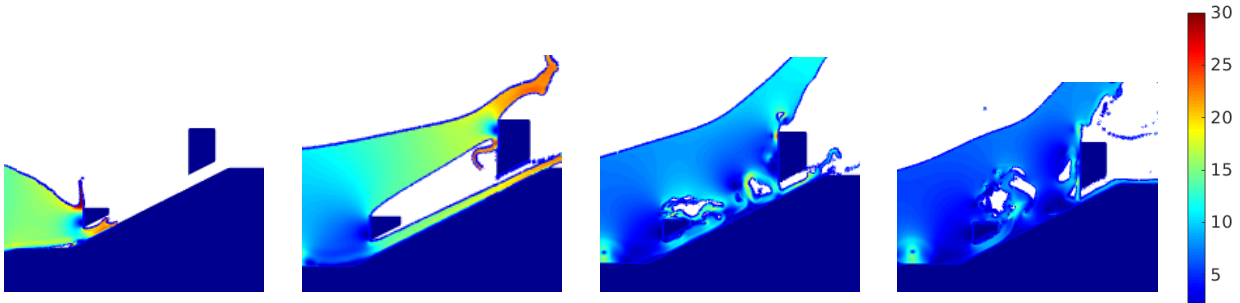

(a) time 3.15 **(b)** time 3.5 **(c)** time 4 **(d)** time 4.3

Figure 76: Structure 12 collision dynamics.

For Structure 13, the only impact is when the wave reaches the final block. This results in a strong redirection of the upper part of the wave, which is visible around time 3.5s. From this, the trajectory of the water has changed. However, the flow is not disrupted, which can be seen through the smooth color gradient of the water. At first, the water in the 'free path' reaches the crest undisturbed. However, later on vortices appear in the 'free path', which results in splashing of water on the crest, visible from time 4s.

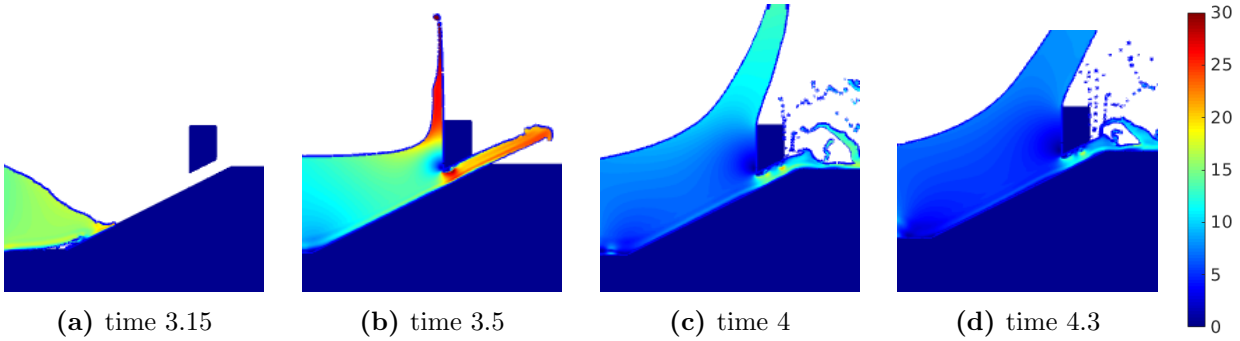

(a) time 3.15 **(b)** time 3.5 **(c)** time 4 **(d)** time 4.3

Figure 77: Structure 13 collision dynamics.

Summary

From the data considered in this section, it can be deduced that at least two blocks are needed to incite turbulent flow during the wave run up. A splashing wave is considered less damaging, as its force is less directed [18]. For that reason, in this study the first block is deemed necessary, despite the lower overtopping for Structure 13. The next goal for this study is to consider a different shape of the first roughness element, to enhance the occurrence of the turbulent flow.

On the other hand, as the lack of the middle roughness element has slightly improved the efficiency of the dike regarding the overtopping reduction, the block is not considered a crucial part of the structure and hence it is not included in further designs.

Furthermore, the collision dynamics for Structure 13 depicted that the last roughness element is functional for the redirection of the fluid flow. The attempt to improve this property of the block is studied in Subsection 6.10.

6.9 First block

As discussed in Subsection 6.8, the first roughness element placed on the slope has a significant influence on the dynamics of wave run up. The impact with the block breaks down the fluid trajectory, which combined with another collision incites turbulent flow. In this section, more complex designs of the first block are considered, in order to enhance that dynamic. Three designs are considered, where the shape of the element is modified. The inspiration for the changes are the modern designs of the revetment blocks as depicted in Figure 10 and discussed in Section 4. They allow for additional fluid flow in between roughness elements, through incorporation of 'channels' in the structure. The three designs considered in this subsection are meant to imitate that property, causing an unrealistically 'elevated' two-dimensional shape.

The first shape is based on the parallel slope used in Structure 4, which was introduced in subsection 6.3. An additional change is the inclusion of a 'free channel' of height $0.25m$ through the middle of the block. This design is labeled as Structure 14, and alongside its dimensions, it is depicted in Figure 78. The idea is for the first block to incite more turbulence, rather than redirect the trajectory of the flow. Due to the complexity of the flow, the extended computational grid visible in Figure 17 is used for this simulation.

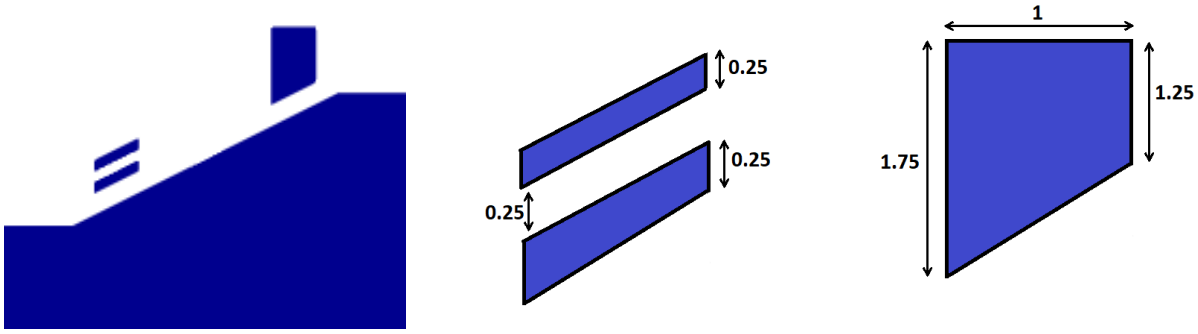

(a) Design of the roughness elements. **(b)** Dimension of the blocks.

Figure 78: Structure 14

The second design, referred to as Structure 15, is depicted in Figure 79. A 'free channel' of height $0.2m$ is incorporated into the previous block shape also for the case used in Structure 12. The idea is to allow part of the water to pass through the roughness element more easily, while still breaking down the wave. The extended grid previously depicted in Figure 17 is used for this simulation, due to the complexity of the fluid flow.

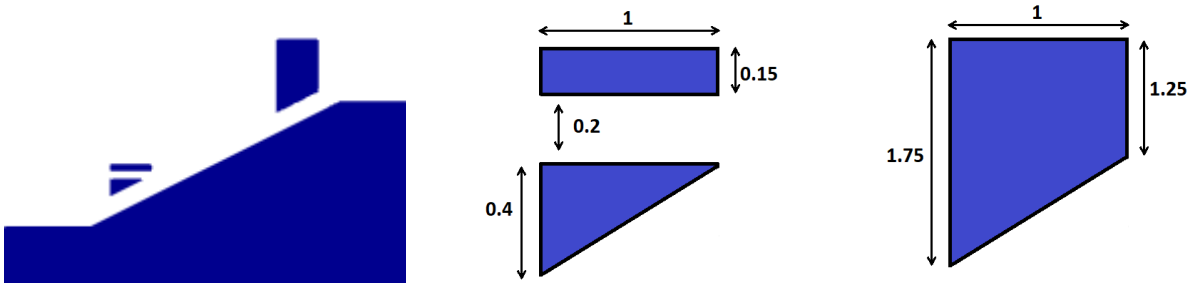

(a) Design of the roughness elements. **(b)** Dimension of the blocks.

Figure 79: Structure 15

The final design considered in this subsection is Structure 16, visible in Figure 80. Instead of a full open 'channel', a triangular incision of height $0.4m$ and width $0.5m$ is added to the front face of the block. The anticipation is to enhance turbulence before the first element.

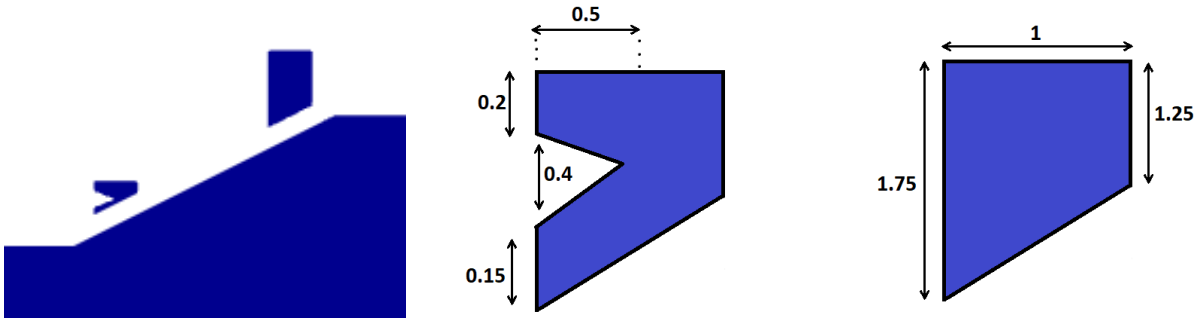

(a) Design of the roughness elements. **(b)** Dimension of the blocks.

Figure 80: Structure 16

The various designs had different influence on the recorded wave overtopping. Recall, that for the previously discussed Structure 12 the overtopping was slightly higher than $6m^3$. The biggest improvement is observed for Structure 14, where the amount of water has dropped to only $2.7m^3$. This makes it the most effective design in comparison to the ones previously discussed. A small reduction in overtopping is also registered for Structure 15, where the final amount is slightly above $5m^3$. On the other hand, the inclusion of the triangular incision worsened the design, as the overtopping rose above $7m^3$. With this data, it can be deduced that the 'free channel' has a beneficial effect on the performance of the structures.

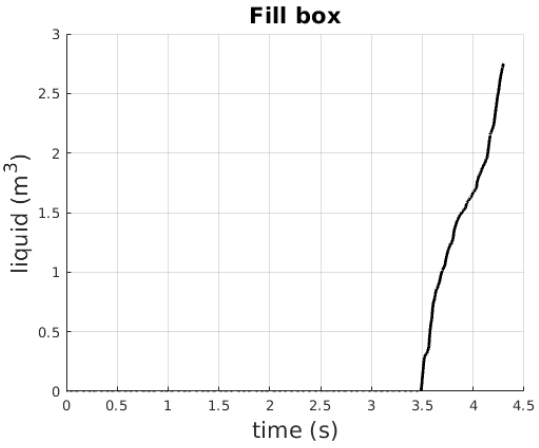

(a) Structure 14

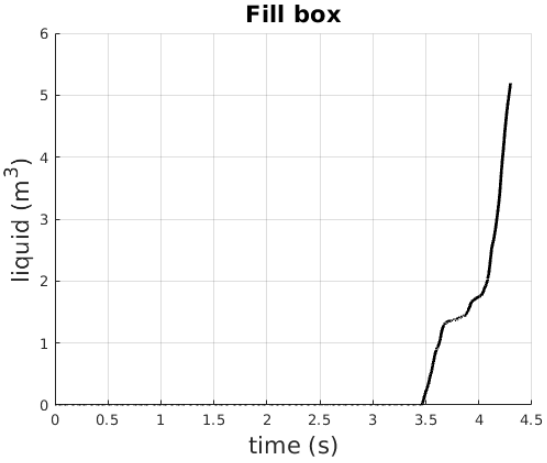

(b) Structure 15

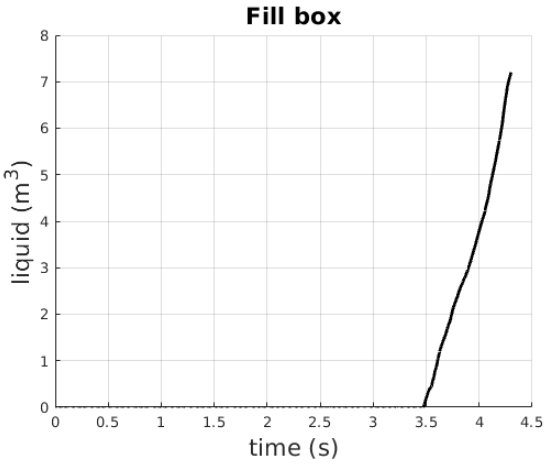

(c) Structure 16

Figure 81: Overtopping measurement for Structure 14, Structure 15 and Structure 16.

The data of the horizontal hydrodynamic forces acting on the three structures is given in Figure 82. For all of the graphs there are vast oscillations, suggesting chaotic flow. The highest value of approximately $5.8 \times 10^5 N$ is obtained for Structure 15, however the maximal values for other designs are of similar scale. Only for Structure 14 the force experienced seems to gradually decrease. For the other two designs there appear to be numerous peaks occurring in the force signal.

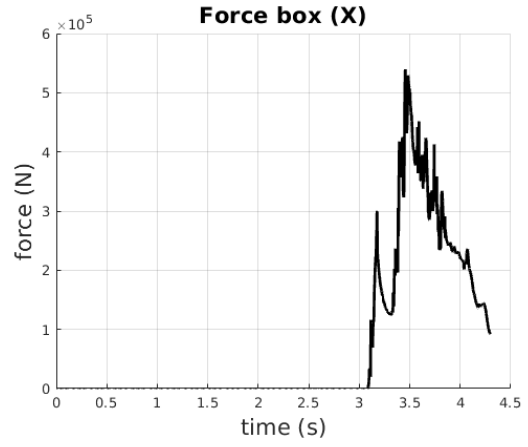

(a) Structure 14

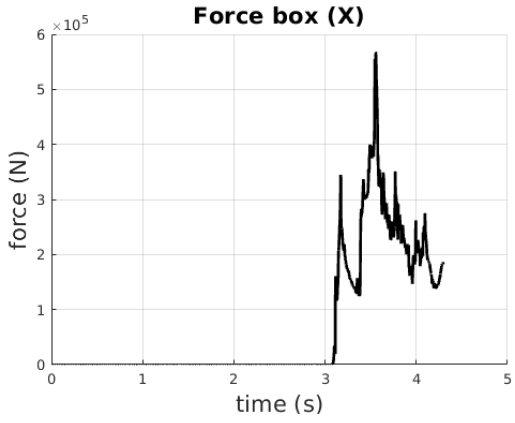

(b) Structure 15

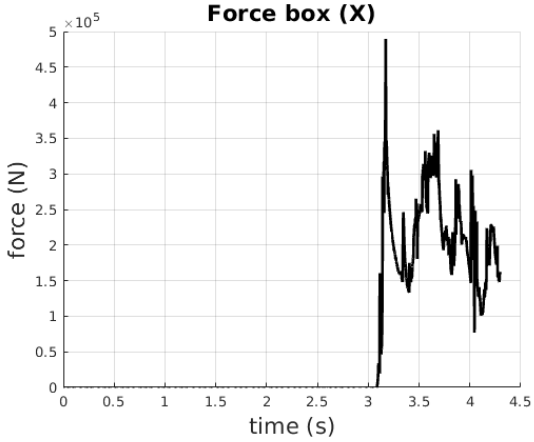

(c) Structure 16

Figure 82: Horizontal hydrodynamic force acting on Structure 14, Structure 15 and Structure 16.

The vertical forces registered are depicted in Figure 83. The patterns and scales of the measurements are comparable for all designs considered. At the initial collision there occurs a singular high peak, which attains values between $-8 \times 10^5 N$ and $-11 \times 10^5 N$. After that, the curves show numerous oscillations of average magnitude around $-3 \times 10^5 N$. Hence, for the vertical hydrodynamic forces do not seem to be affected by the modifications of the first roughness element.

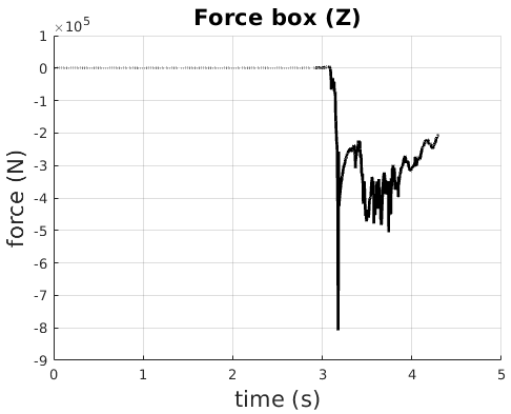

(a) Structure 14

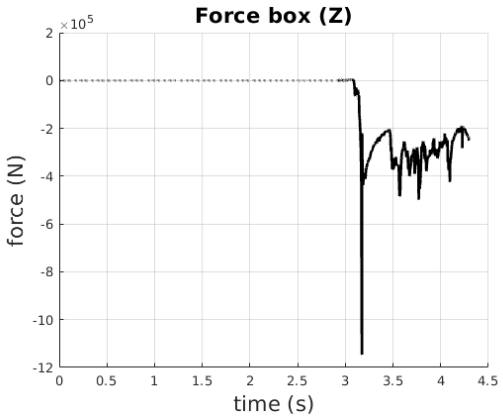

(b) Structure 15

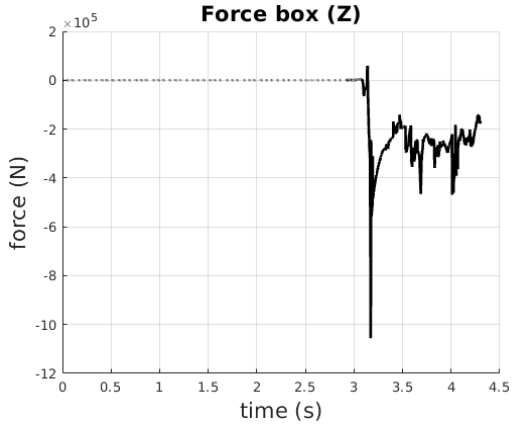

(c) Structure 16

Figure 83: Vertical hydrodynamic force acting on Structure 14, Structure 15 and Structure 16.

Then, let us study the horizontal velocities of fluid passing through the monitor points. The water in the 'free path', where the points are located, is strongly influenced by how turbulent the flow is. As such, the modifications applied to the first roughness element should have a visible effect on the velocities, especially those registered in the latter two points.

The data for the first monitor point is given in Figure 84. The shape and scale of the curves is almost identical, with the maximum value reaching $16m/s$ and the velocity at the end of the simulations being close to $2m/s$. This was expected for Structure 14 and 15 due to their build. However, the incentive for the shape of Structure 16 was to enhance turbulent flow in front of the first block. As such, one would expect changes in the velocity at the first monitor point. Due to lack of such observations, the design of Structure 16 is likely to be less effective.

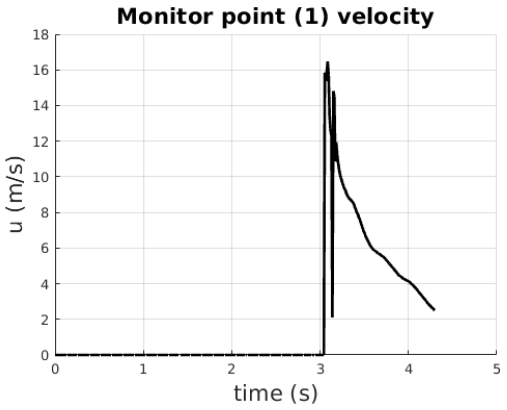

(a) Structure 14

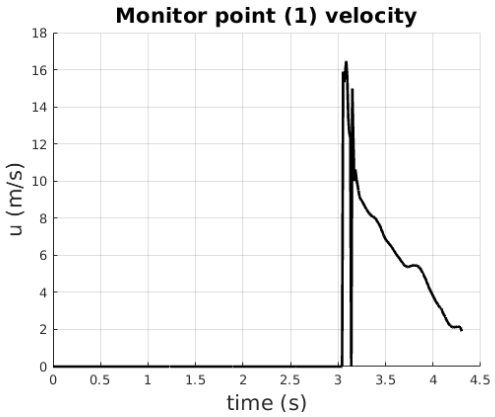

(b) Structure 15

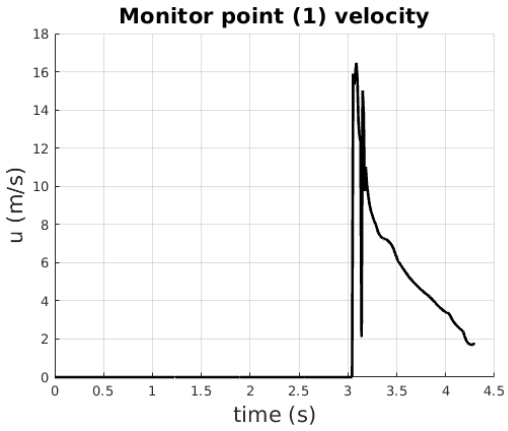

(c) Structure 16

Figure 84: Horizontal velocity measured at the first monitor point for Structure 14, Structure 15 and Structure 16.

Figure 85 depicts the horizontal velocities registered at the second monitor point. The maximum value for all designs is between $20m/s$ and $25m/s$, after which the velocity is decreasing in value. There are many oscillations seen for Structure 14 and Structure 15, suggesting a turbulent flow. For Structure 16 there are minimal disturbances to the function. Additionally, for all of the designs, negative velocities are measured, which implies a flow in the opposite direction. This is especially noticeable for Structure 16, where the most negative value is $-10m/s$. This is most likely caused by the reflection of water from the final block.

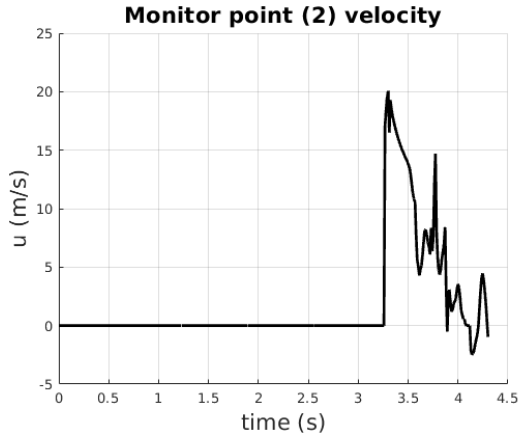

(a) Structure 14

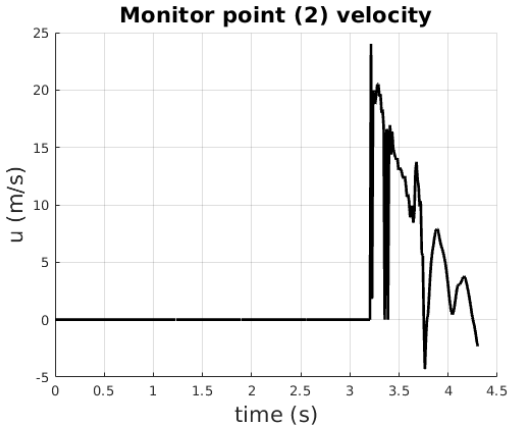

(b) Structure 15

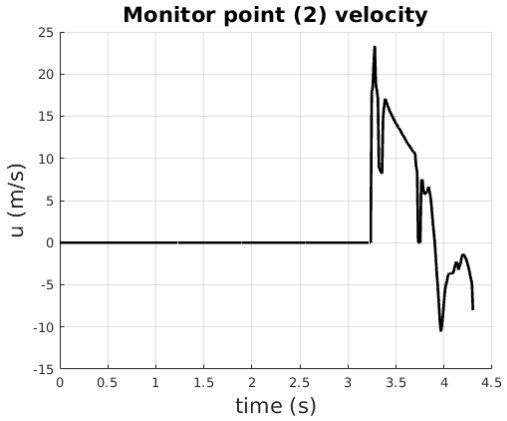

(c) Structure 16

Figure 85: Horizontal velocity measured at the second monitor point for Structure 14, Structure 15 and Structure 16.

At the last monitor point all of the data shows numerous spikes, as visible in Figure 86. This implies that the wave undergoes significant splashing, or alternatively the water reaching the crest of the dike can take form of multiple droplets.

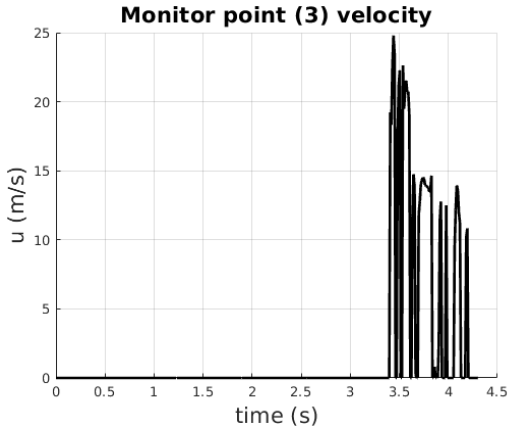

(a) Structure 14

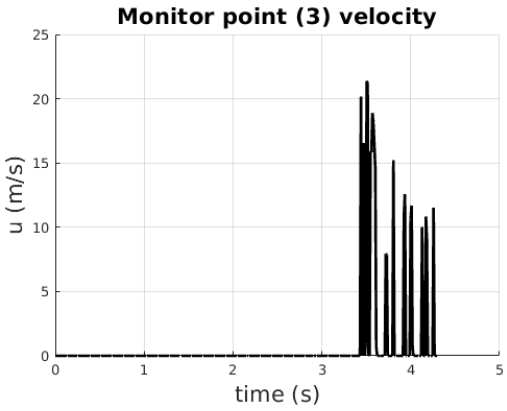

(b) Structure 15

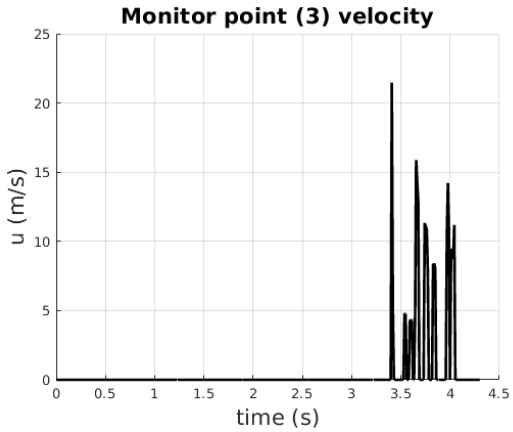

(c) Structure 16

Figure 86: Horizontal velocity measured at the third monitor point for Structure 14, Structure 15 and Structure 16.

Finally, let us analyze the collision dynamics from the simulation snapshots. The coloring of the plots is based on the absolute velocity of the water, given on a scale 0 to 30.

Figure 87 depicts the wave run up for Structure 14, which was the most effective in overtopping reduction. At time $3.15s$ it can be observed that the majority of the water goes inside the 'free channel' and below the block, instead of shooting up, like in previous simulations. Then the water travels around the two parts of the block, hitting the final roughness element. The wave is redirected upwards, similarly to previously discussed regarding Structure 13. However, the absolute velocity of the water is smaller in comparison to that given in Figure 77. Furthermore, the turbulent flow can already be observed by time $3.5s$, in the form of vortices forming in front of the final block. In the snapshot for time $4s$ a complex flow is visible, where the vortices appear in between the two blocks in a zig-zag pattern. This continues up to the end of the simulation, as visible for time $4.3s$. The turbulent flow reduced the amount of water passing to the crest through the 'free path', which can be observed in the last two snapshots. Finally, the wave passing above the structure is slowly moving towards the crest, where minimal splashing can be spotted.

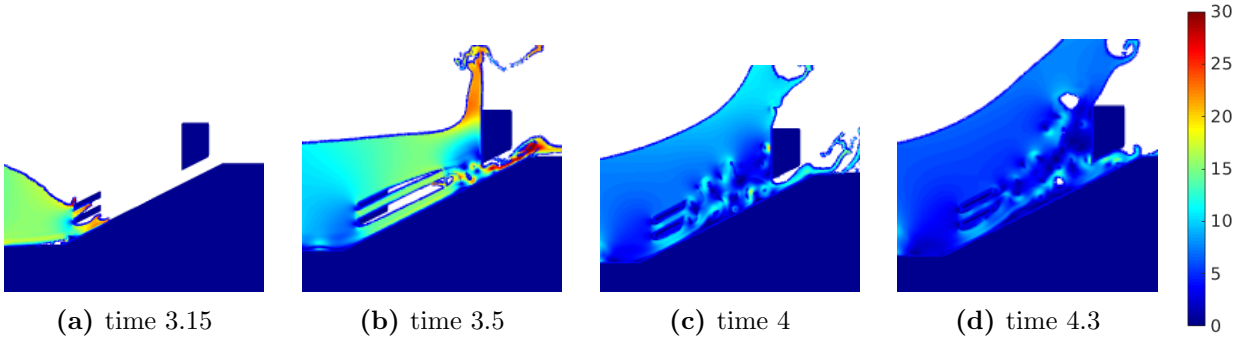

(a) time 3.15 **(b)** time 3.5 **(c)** time 4 **(d)** time 4.3

Figure 87: Structure 14 collision dynamics.

The collision dynamics for Structure 15 are given through snapshots visible in Figure 88. The impact with the first block resembles strongly the behavior observed in previous simulations. The water shoots around the element, with its trajectory slightly moved upwards. Then, the wave collides with the last block, as visible at time 3.5s. A small amount of fluid travels through the channel, however it merges with the water passing through the 'free path' of the dike. This interaction does not result in much turbulence at first, however there is small splashing observed in front of the last block. The water dynamics becomes more chaotic due to the fluid reflecting from the final element. The turbulence can be observed at time 4s and 4.3s, however it does not have a visible pattern like the one for Structure 14. Finally, by the end of the simulation, the water flows through the 'free path' towards the crest without much difficulty, as seen at time 4.3s.

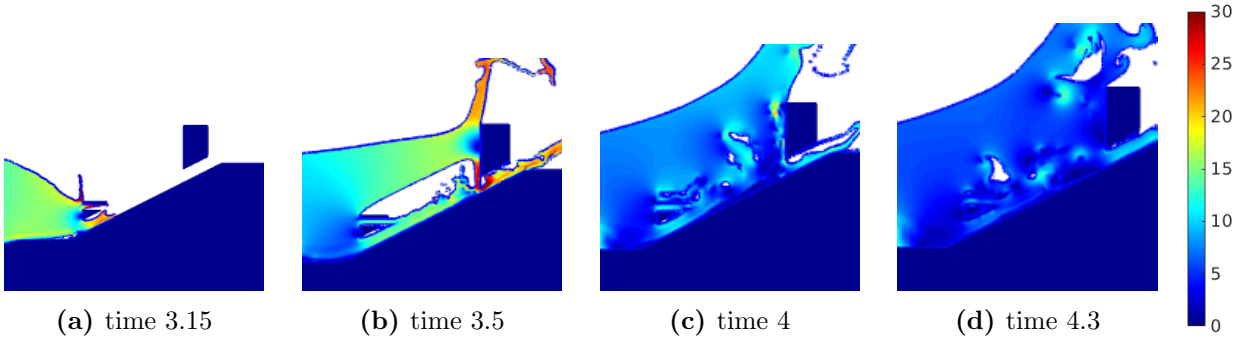

(a) time 3.15 **(b)** time 3.5 **(c)** time 4 **(d)** time 4.3

Figure 88: Structure 15 collision dynamics.

The fluid flow for the last structure is given in Figure 89. At the initial impact with the roughness elements, the water quickly fills up the triangular incision applied to the first block. This is visible in the first snapshot at time 3.15s. Furthermore, it appears that the water in that area is trapped, which can be deduced from its minimal velocity. With this, the modification has minimal effect on disruption of the fluid flow for the duration of the simulation. The wave travels around the first block, before colliding with the final element. Part of the water flows above the structure towards the crest, however its trajectory is slightly redirected upwards. The fluid reflecting from the final block incites chaotic flow in the middle of the structure, as visible at time 4s and 4.3s. The water in the 'free path' passes towards the crest in a thin stream. From these snapshots it can be deduced that the triangular incision does not have a significant influence on the fluid flow.

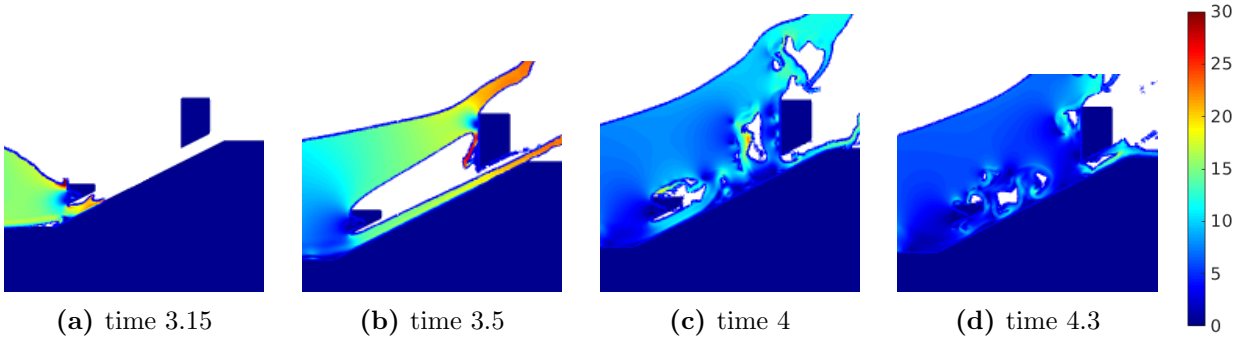

(a) time 3.15 **(b)** time 3.5 **(c)** time 4 **(d)** time 4.3

Figure 89: Structure 16 collision dynamics.

Through studying the three designs of the initial block, it can be concluded that Structure 14 is the most effective in terms of inciting turbulent flow. This can be seen through the zig-zag pattern of vortices that appear in between the roughness elements and the greatly reduced overtopping to below $3m^3$. The other two designs were not as successful. For that reason, Structure 14 is chosen as the base for the design of next simulations.

6.10 Last block

The final component considered in this research is the shape of the last block. As concluded at the end of Subsection 6.8, the roughness element placed on top of the seaward slope is very functional in redirecting the fluid. Changing the trajectory of the wave vastly reduced the overtopping. For that reason, the goal of this section is to enhance that property of the block, by attempting two designs meant to reverse the direction of the water as much as possible. Both of them are based on Structure 14, which was the most efficient of all previous simulations.

Additionally, to prevent possible numerical errors, caused by the high complexity of the flow, the extended grid shown in Figure 17 was used.

The first design, labeled Structure 17, is visible in Figure 90. An elliptic 'incision' is applied to the front wall of the last roughness element. The horizontal radius of the cut is equal to $0.5m$ and the vertical one is $0.7m$. The intended purpose is to let the wave flow inside the bottom part of the ellipse, follow its curvature and then return towards the sea.

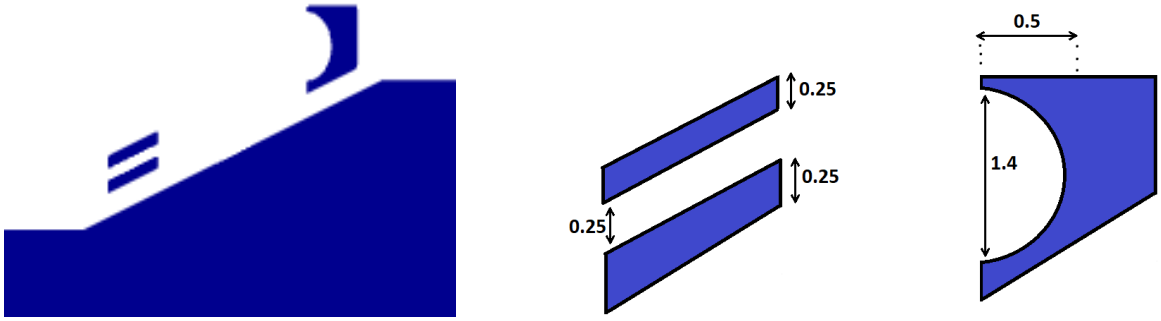

(a) Design of the roughness elements. **(b)** Dimension of the blocks.

Figure 90: Structure 17

Another design meant to redirect the incoming water is Structure 18, depicted in Figure 91. The applied 'incision' consist of a triangle on the bottom half of the block, and an ellipse above it, which shortens the top part of the block. Once more, this design is meant to reverse the trajectory of the wave. The velocity of the wave is meant to be slowed down further on the triangular part of the incision, and redirected by the half ellipse.

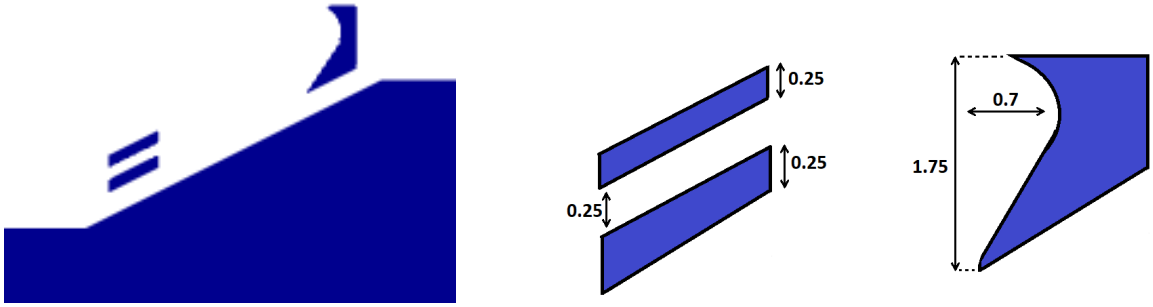

(a) Design of the roughness elements. **(b)** Dimension of the blocks.

Figure 91: Structure 18

Recall, that the overtopping for Structure 14, on which both considered designs are based, was around $2.7m^3$. The corresponding data for Structure 17 and Structure 18 is given in Figure 92. Only a minimal reduction of about $0.1m^3$ can be observed for both simulations. As such, from just this data one cannot determine which design is more effective.

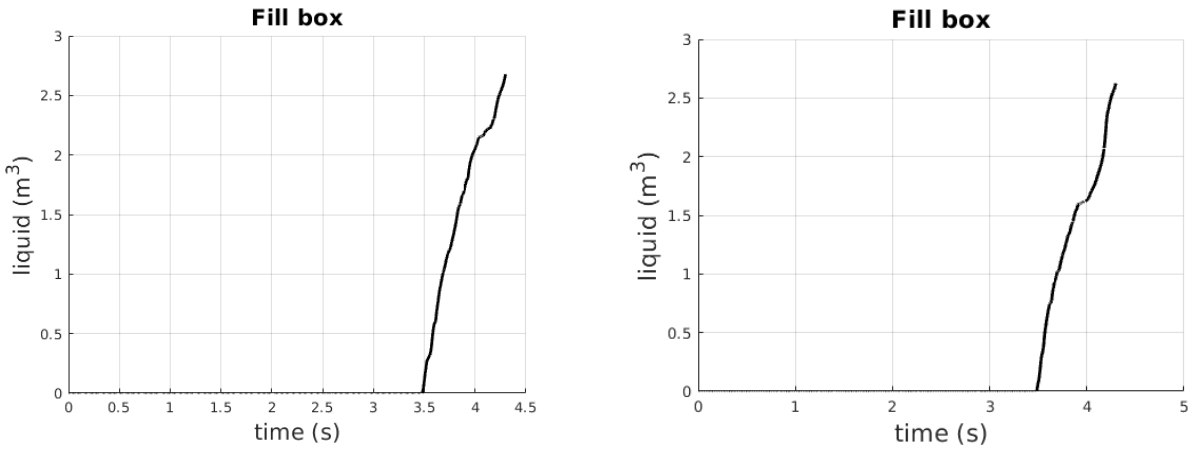

(a) Fill box for Structure 17 **(b)** Fill box for Structure 18

Figure 92: Overtopping measurement for Structure 17 and Structure 18.

The results for the horizontal hydrodynamic forces are given in Figure 93. The patterns for both are comparable, with many spikes occurring. This suggests a non-uniform flow. The maximal value is slightly lower for Structure 18, where it does not rise above $6 \times 10^5 N$.

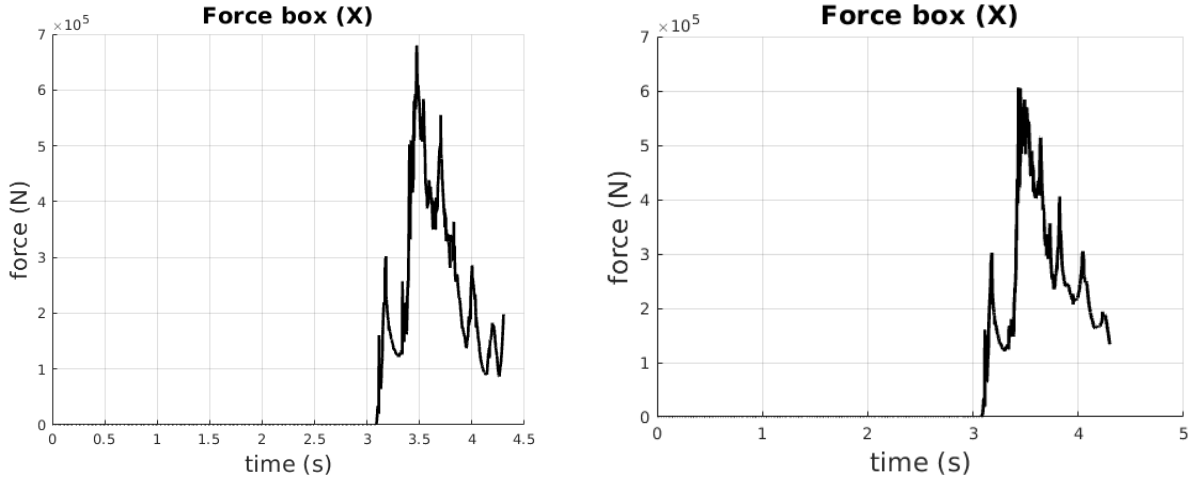

(a) Structure 17 **(b)** Structure 18

Figure 93: Horizontal hydrodynamic forces acting on Structure 17 and Structure 18.

An almost identical behavior is also observed for the vertical forces depicted in Figure 93. The largest magnitude is the same for both structures, and the pattern of the curves is comparable. Once more, the appearing oscillations imply a turbulent flow.

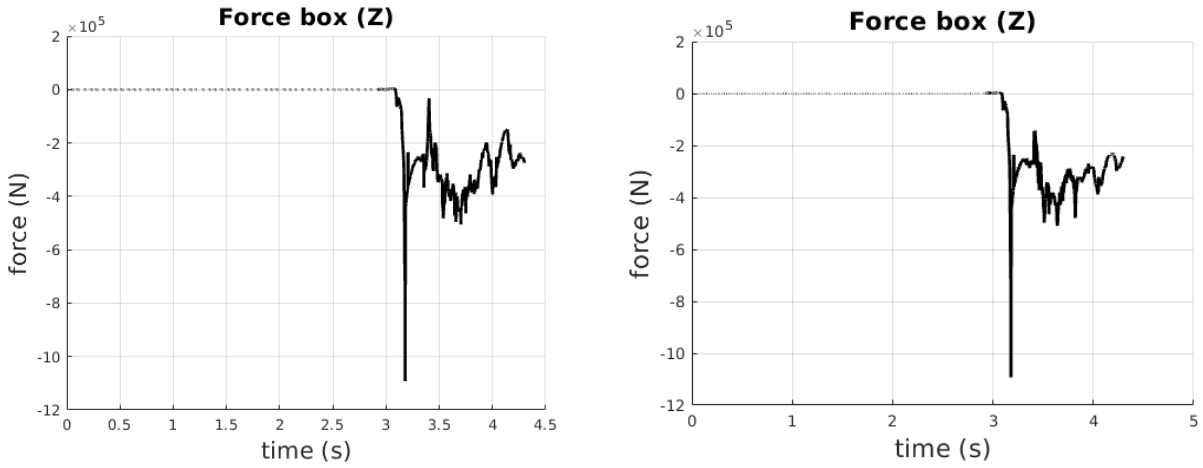

(a) Structure 17 **(b)** Structure 18

Figure 94: Vertical hydrodynamic forces acting on Structure 17 and Structure 18.

The horizontal velocities of the water passing through the monitor points are given in Figure 95. By eye, the results at the first monitor point are identical for the two simulations. This suggests that the modification of the last block does not have any effect on the flow near the start of the slope. At the second monitor point, the maximal value for both designs is $20m/s$. Only after time $3.5s$ the curves differ slightly. Near the end of the simulation, a negative velocity is observed for Structure 17. This can either imply a chaotic flow, or the reflection of the water from the last block. For structure 18 there are spikes visible, however the horizontal velocity is always positive. At the final monitor point, the readings for both simulations take the form of oscillations, with the maximal value around $20m/s$. This suggest an improvement in the design, as the highest magnitude of velocity for Structure 14, was around $25m/s$. As such, it suggests that the incisions in the final block are beneficial.

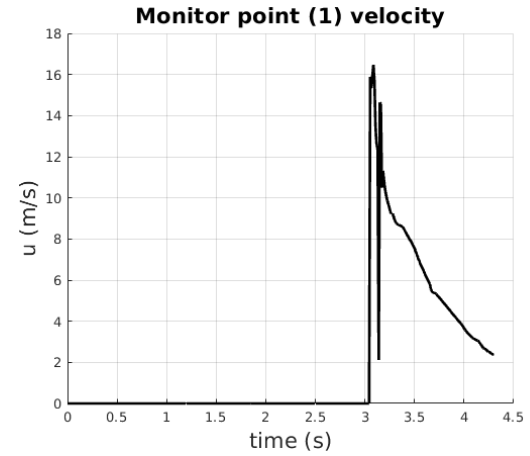

(a) Structure 17

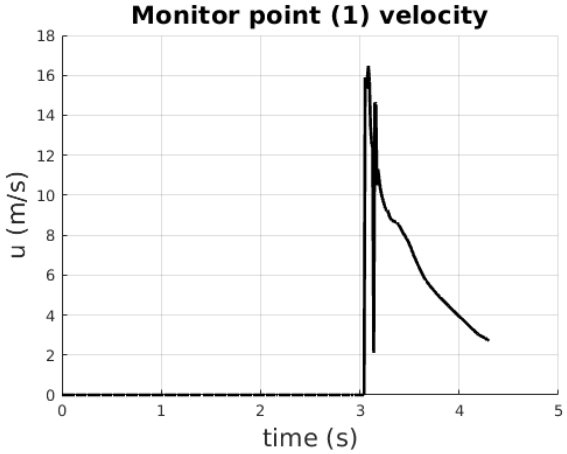

(b) Structure 18

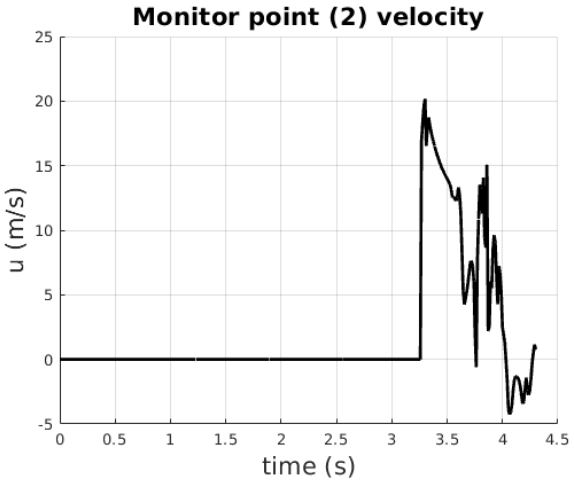

(c) Structure 17

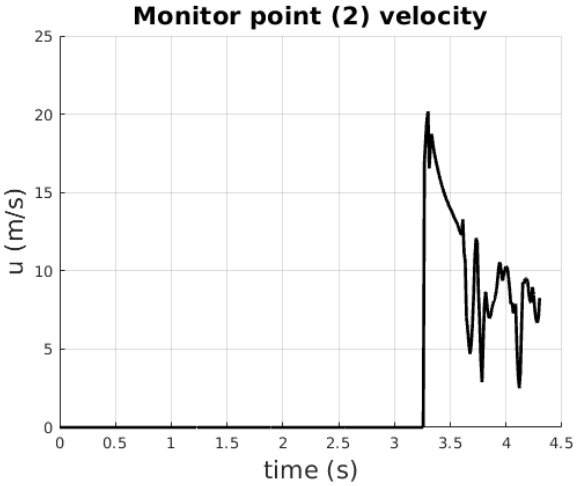

(d) Structure 18

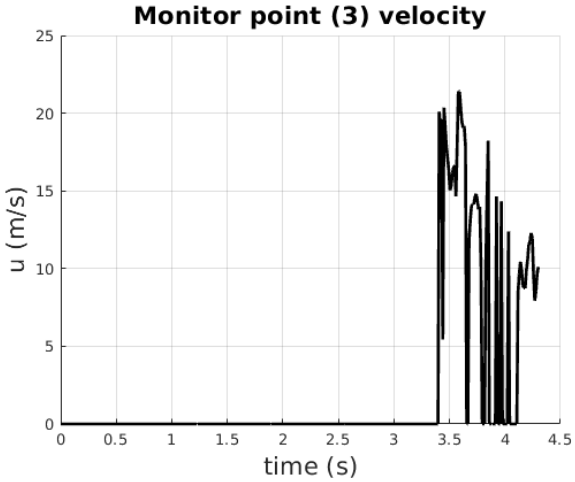

(e) Structure 17

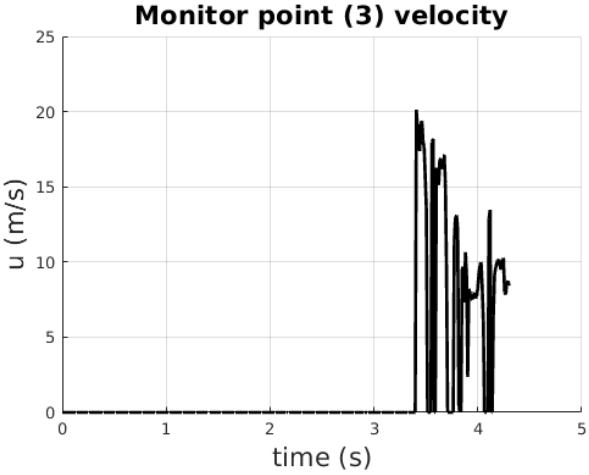

(f) Structure 18

Figure 95: Horizontal velocity measured at monitor points for Structure 17 and Structure 18.

Finally, let us consider the collision dynamics. Because of the higher complexity of the flow, a larger

amount of snapshots is given. This is to ensure a proper analysis of the fluid flow. The colors of the plots are based on the absolute velocity on a scale from 0 to 30.

The images for Structure 17 are given in Figure 96. After the initial impact with the first block, the wave is split into three parts, as visible for time 3.35s. Then, the middle part of the fluid flows into the elliptic incision and travels along its curvature. On the other hand, the upper part of the wave connects with the top part of the final block, as seen at time 3.4s. After that, all three parts of the wave collide with each other causing splashing and turbulent flow. The vortices are seen in the zig-zag pattern between the roughness elements, and inside the incision. The chaotic flow reduced the fluid that passes through the 'free path', as seen at time 4s. At the final snapshot, a vortex appears in the upper part of the wave, which highlights how turbulent the flow is.

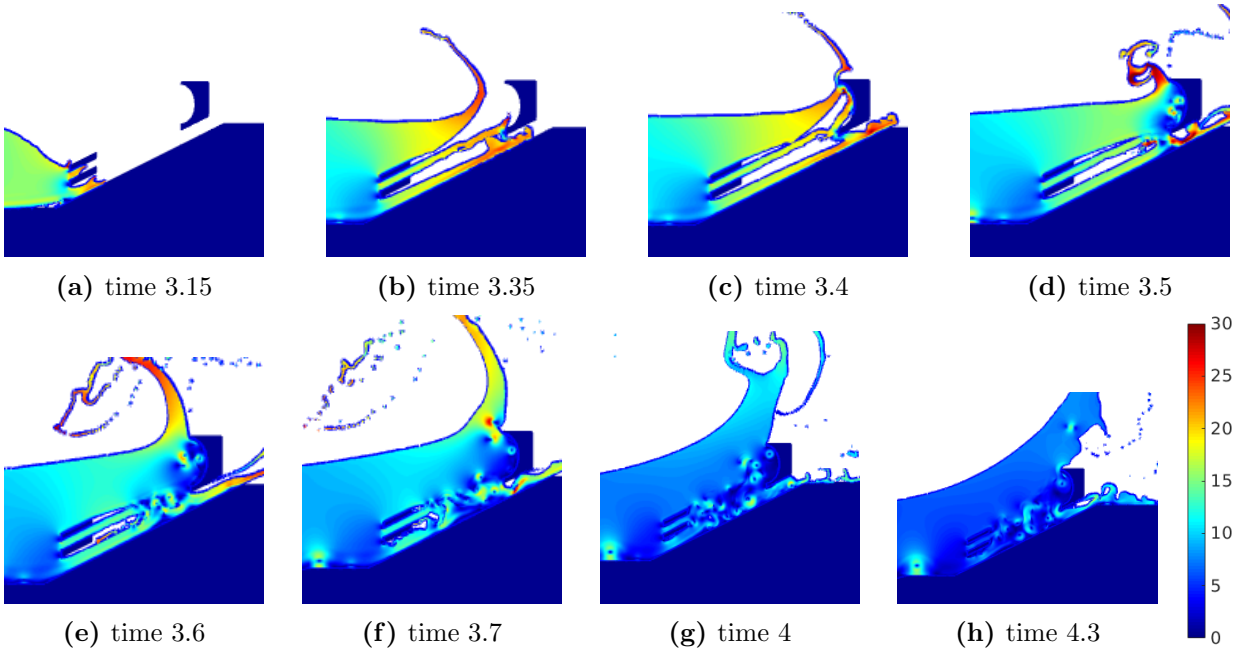

(a) time 3.15 **(b)** time 3.35 **(c)** time 3.4 **(d)** time 3.5

(e) time 3.6 **(f)** time 3.7 **(g)** time 4 **(h)** time 4.3

Figure 96: Structure 17 collision dynamics.

The snapshots for the final Structure 18 are given in Figure 97. The initial phase of the flow is comparable to the one for Structure 17. The first roughness element splits the wave into three parts, which later connect near the last block. The middle one follows the shape of the incision closely, and connects with the upper part, visible at time 3.5s. Because of that the flow is slightly disrupted, as visible at times 3.6s and 3.7s. This results in splatter and many droplets of water forming. After a short time more water flows above the final block, and the effects of the incision are not as visible. A turbulent flow forms in between the two blocks and by the incision. Some of the vortices seem to travel above the final element, which results in large splatter seen at time 4.3s. However, for this simulation, the flow in the 'free path' does not appear to significantly reduce the amount of water reaching the crest.

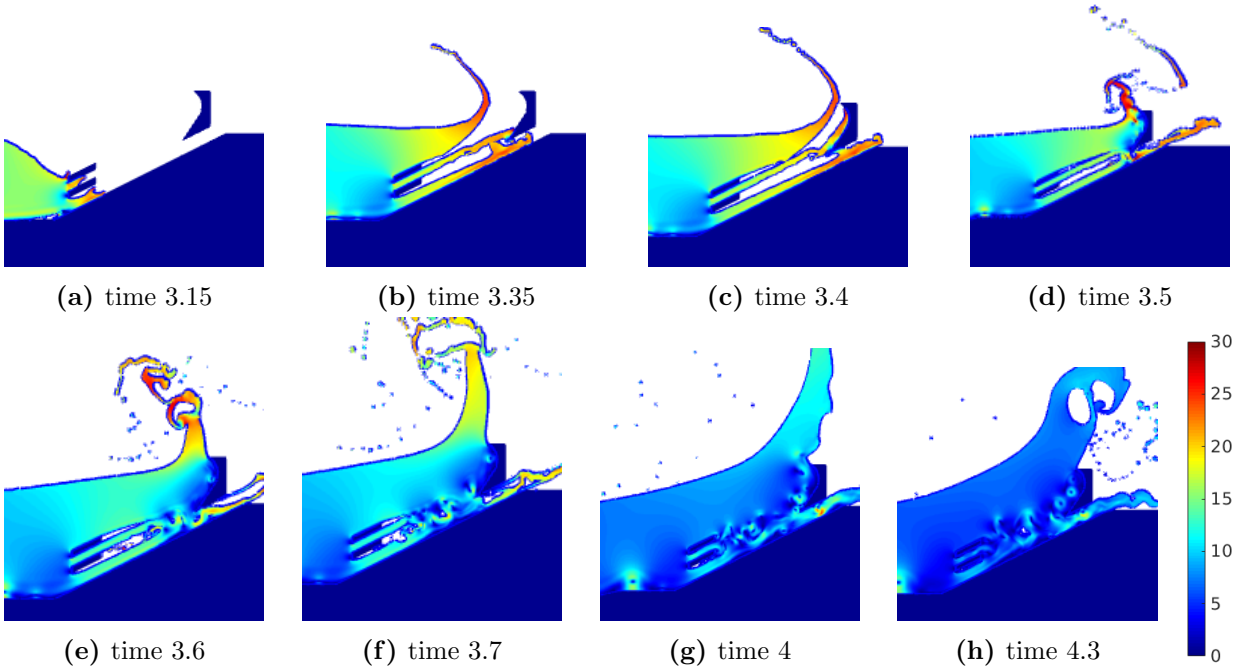

(a) time 3.15 **(b)** time 3.35 **(c)** time 3.4 **(d)** time 3.5

(e) time 3.6 **(f)** time 3.7 **(g)** time 4 **(h)** time 4.3

Figure 97: Structure 18 collision dynamics.

Summary

Finally, the results of this subsection indicate an influence of the incision in the final block onto the fluid flow. It caused a small improvement of the design, however a more significant effect was anticipated. The modifications redirected only the part of the wave that traveled through the channel in the first block. This resulted in small disruptions and splatter.

However, in comparison with the initial design of the smooth dike, the majority of the overtopping has been suppressed by inclusion of the modified elements. For the first structure the amount of fluid in the fill box reached almost $14m^3$, while for the final simulations it was below $2.75m^3$. Therefore, the measured wave overtopping has been reduced by approximately a factor of 5. This was obtained by enhancement of the turbulence and redirection of the wave trajectory.

Further discussion of the results, and of possible improvement, can be found in Section 8.

7 Observations of numerical errors

A crucial element of the analysis of simulations is the occurrence of numerical errors. They can be of a different origin and significance. While some can be neglected, due to the minimal effect on the final solution, others may have tremendous consequences. In this section, the numerical errors observed throughout the simulations are discussed together with possible adjustments meant to resolve the issue.

7.1 Line of vertical droplets

The first type of a numerical error took form of small droplets forming a vertical line, which more or less connects the roughness elements with the water mass above them. This pattern has been noted for four different structures around time $3.5s$ and is depicted in Figure 98. Similar dynamics has not been noted for any other structures. Due to the small mass and speed of the droplets, they do not affect the main water flow. For that reason, this type of numerical error is considered negligible. Nonetheless, let us examine the origin of this error.

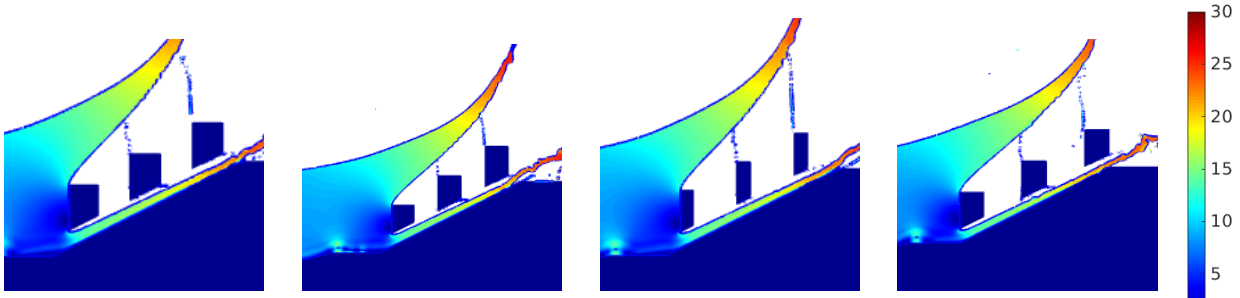

(a) Structure 3 **(b)** Structure 5 **(c)** Structure 7 **(d)** Structure 9

Figure 98: Minor numerical error in the form of vertical lines of small droplets appearing around time $3.5s$.

Additional snapshots of the simulation for Structure 3 are visible in Figure 99. The 'free path' below the roughness elements is part of the domain where the error occurs. Therefore, let us analyze the part of the wave that flows beneath the first block. At time $3.2s$ it can be seen that the water mass passes below the roughness element. Without additional objects disrupting the flow, the water should not rise. This can be observed for Structure 16, where at time $3.5s$ the lower part of the wave flows smoothly through the 'free path', as depicted in Figure 89b. However, for Structure 3 there is a sudden rise in the water, causing a collision with the second block, as visible in Figure 99b. This results in a thin vertical line of fluid shooting up the second block. A similar dynamic occurs near the last block on the slope. Additionally, at time $3.35s$, we can observe a thin line of water between the two upper roughness elements, as if the fluid sticks to the second block.

The cause of these seemingly unrealistic water dynamics is not certain. However, as stated in Subsection 2.3, near solid boundaries the discretization is changed to first-order upwind. This decreases the overall accuracy of the solution in the 'free path' and the increased artificial diffusion can negatively affect the water dynamics. Another difficulty in that part of the domain is that many grid cells are not fully open to flow. Because of this, more errors could occur during the reconstruction and advection of the water. The combination of these components is a probable cause for the numerical errors. However, as these unrealistic dynamics do not seem to have a

critical effect on the main wave flow, they can be neglected. Further study on the accuracy of ComFLOW in geometries such as the 'free path' is advised.

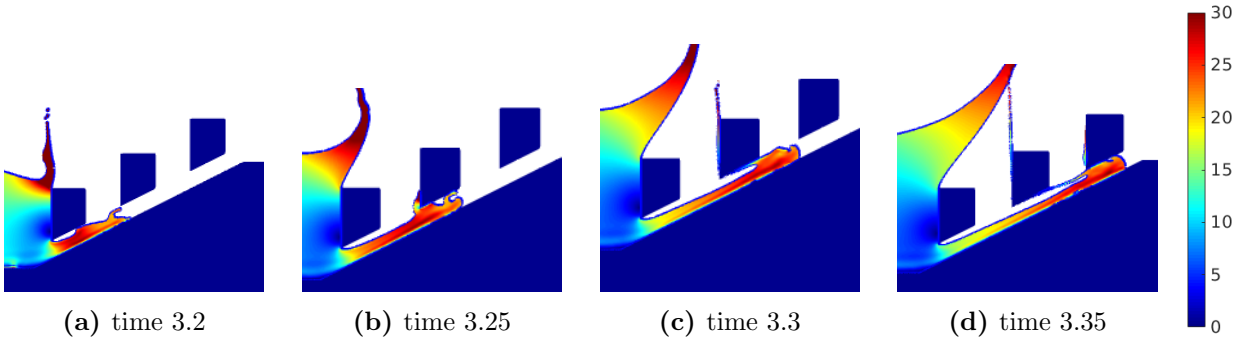

(a) time 3.2 **(b)** time 3.25 **(c)** time 3.3 **(d)** time 3.35

Figure 99: Origin of vertical lines of small droplets for Structure 3.

7.2 Droplets acting as bullets

The second type of the numerical error has a major effects on the water dynamics. It takes the form of singular droplets of high velocity, that behave like a 'bullet' during a collision with the wave. An example of this behavior is depicted in Figure 100, where the snapshots depict the ending of the original simulation for Structure 8. The 'original simulation' means the use of the standard computational mesh, which was discussed in Subsection 5.3. Later on, the simulation was re-run on an extended grid to prevent the numerical error from occurring.

As depicted in Figure 100a, at time $3.95s$ the wave has velocity of around $10m/s$, while the droplet closest to the surface reaches almost $20m/s$. Because of the large difference in the velocity, the droplet has a critical effect on the wave despite its small mass. This results in highly unrealistic wave dynamics. For this reason, the numerical error of the 'bullet droplet' is considered major. The rest of this section is devoted to analyzing and resolving this error.

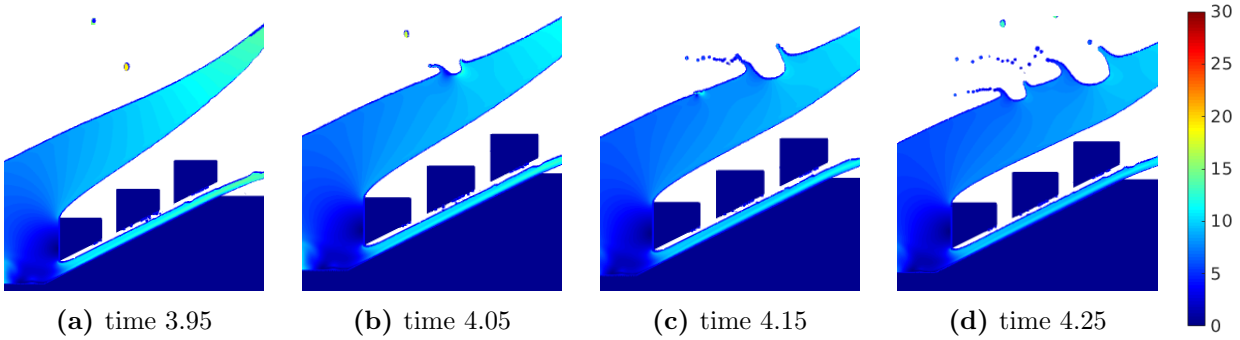

(a) time 3.95 **(b)** time 4.05 **(c)** time 4.15 **(d)** time 4.25

Figure 100: Major numerical error depicted for Structure 8, computed on the original grid.

Firstly, let us discuss the origin of the error. The overly high acceleration of the droplet is caused by the small volumes of fluid passing through the refinement zones. Recall the standard computational mesh, as introduced in Subsection 5.3, as depicted in Figure 101. With the placement of the refinement levels, a droplet ejected upward passes through both of them, until it reaches the most coarse part of the grid. There, the size of the grid cells is approximately $0.11m \times 0.11m$, which

could be larger than the droplet. Subsequently, as the droplet falls down towards the dike, it has to once more pass through both refinement zones. This could lead to information loss and errors from the free-surface methods.

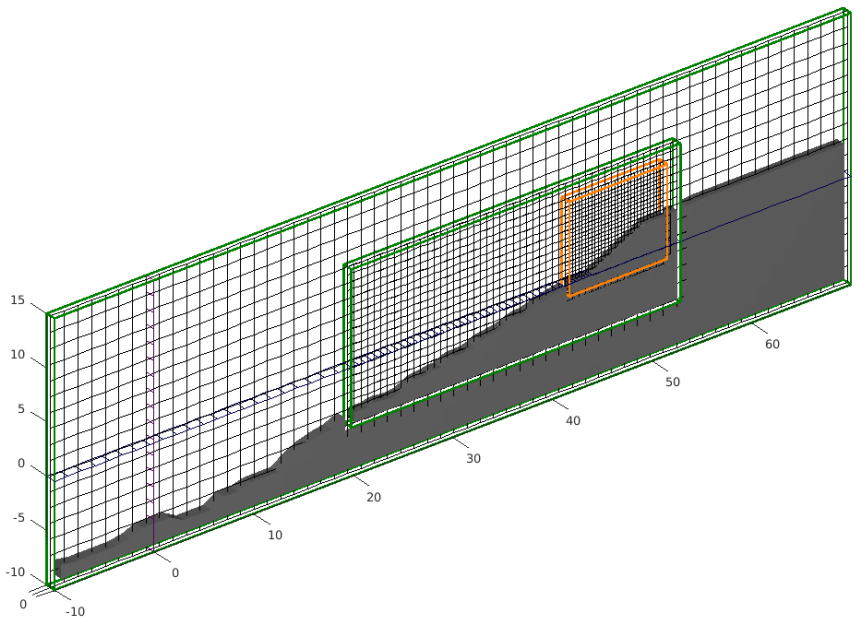

Figure 101: Standard computational grid, with cell stretching and local refinement zones.

A possible reconstruction of an arbitrary droplet moving through refinement zones is depicted in Figure 102. The dark blue is used to represent the actual movement of the water, while the light blue is a feasible result of the free-surface methods. The size difference of the grid-cells is analogous to the local refinement zones discussed in Subsection 5.3. In this example, the volume of liquid is smaller than the mesh size. In the more refined part of the grid, the approximation of the droplet is relatively accurate. However, as it moves upwards to the coarser mesh, the accuracy of the result decreases.

As previously discussed in Subsection 2.4, the location of the fluid in each cell is approximated through a line segment. Because of that, the droplet cannot be placed in the center of the grid cell. Instead, it has to be moved towards one of the corners, which results in information loss. Furthermore, to achieve that placement, the velocity of the droplet may have to be modified. As visible in the middle column of Figure 102, the approximation is placed in the upper corner, however the actual droplet does not rise that high. Therefore, the velocity of the approximated water mass has to be increased. Such errors are amplified, when the size of the grid cells is much larger than the volume of water. When a droplet re-enters the more refined zone, the previous errors are not corrected. This is depicted in the last column of Figure 102, where the location of the approximated droplet remains shifted to the upper left.

The occurrence of the 'bullet droplet' can be explained through the error dynamics described above. To precisely model a droplet, the mesh should be extremely fine, which would significantly increase the computational cost. However, the specific dynamics of droplets are not important for the study of wave overtopping. As such, the goal is to only reduce the error, so that it does not have a critical effect on the wave flow.

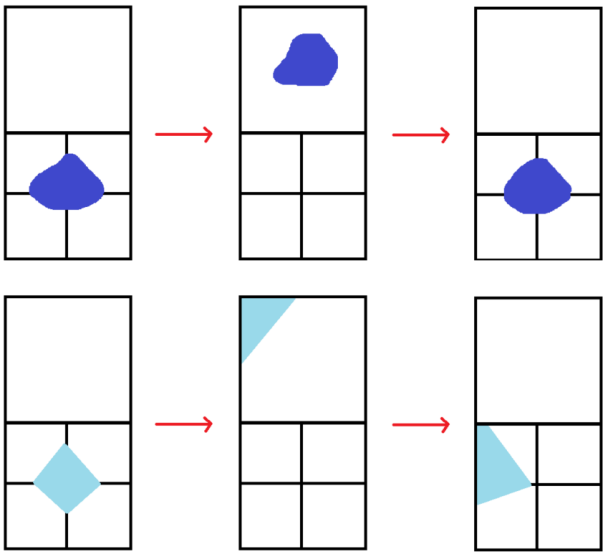

Figure 102: Possible reconstruction of a droplet passing through refinement zones. The dark blue denotes an actual droplet, and light blue is the probable reconstruction of it.

Different attempts were made to correct the bullet effect and resulting numerical error. The first one is the extension of the outer refinement zone, resulting in an alternative computational grid, visible in Figure 103. The details of this mesh are discussed in Section 5.3.

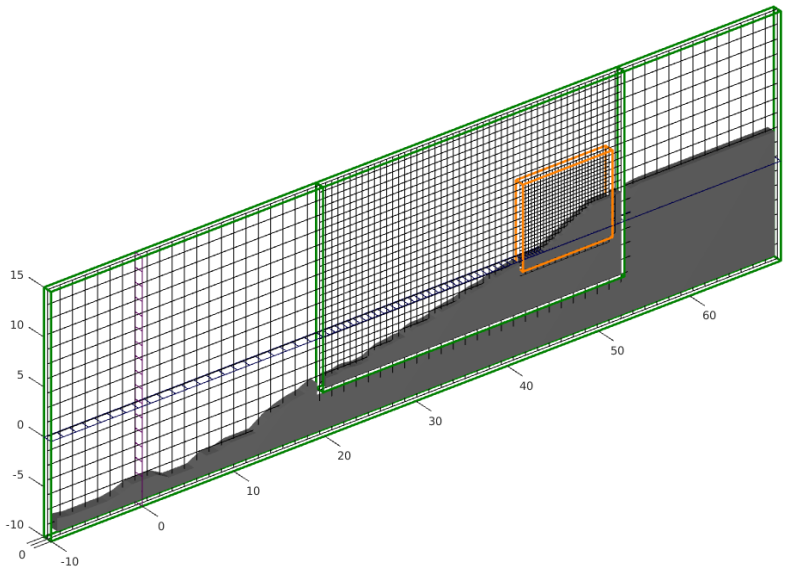

Figure 103: Alternative computational grid with extended local refinement zone.

The stretching of the outer refinement zone towards the upper part of the domain is meant to reduce the error dynamics depicted in Figure 102. This improves the accuracy of the approximation and limits the amount of information loss. The droplet only enters the coarse part of the grid near the upper boundary. This attempt proves successful, as visible in Figure 104, which depicts the re-run

of the simulation for Structure 8. The speed of the droplets has decreased, and as a consequence they do not return to the main wave mass within the time of the simulation. The disadvantage of this approach is the prolonged simulation time. As such, this modification of the simulation set-up should only be applied when necessary, and not used as a standard setting.

This extended grid has been used to correct the simulations, in which similar errors have been observed. Furthermore, it was also applied to the final simulations with complex design of roughness elements, to prevent them from occurring.

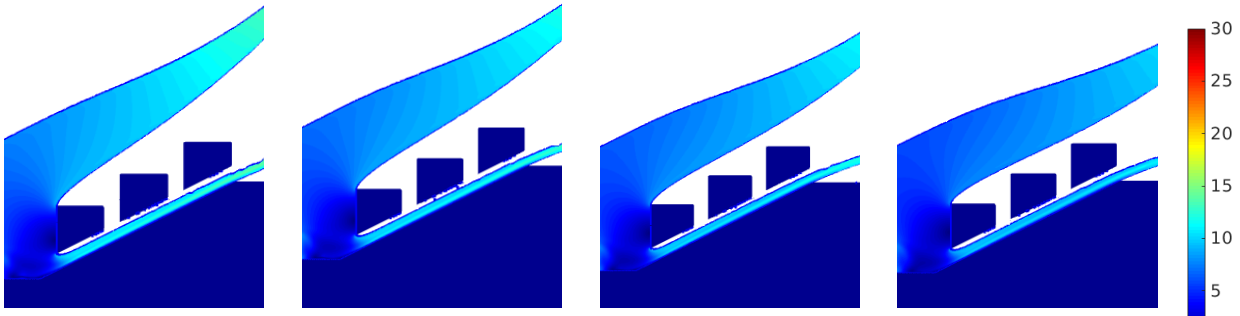

(a) time 3.95 **(b)** time 4.05 **(c)** time 4.15 **(d)** time 4.25

Figure 104: Rerun of the simulation for Structure 8 on the extended computational grid.

An alternative approach of reducing the numerical error caused by the 'bullet' effect, is the use of different free-surface methods. Note that these methods are meant to approximate the wave flow, rather than singular droplets. As such, it is not certain if the methods suggested in the ComFLOW manual are the optimal choice for the simulations incorporating the droplet dynamics. Recall that the method used for the simulations, following the recommended choice in the manual, was the PLIC-VOF method with Young's reconstruction and the MACHO advection method.

Firstly, the other available choice of the VOF method type was investigated, namely the Simple Line Interface Construction (SLIC) method of Hirt and Nichols. In this approach, the free surface is reconstructed with horizontal lines, as visible in Figure 105.

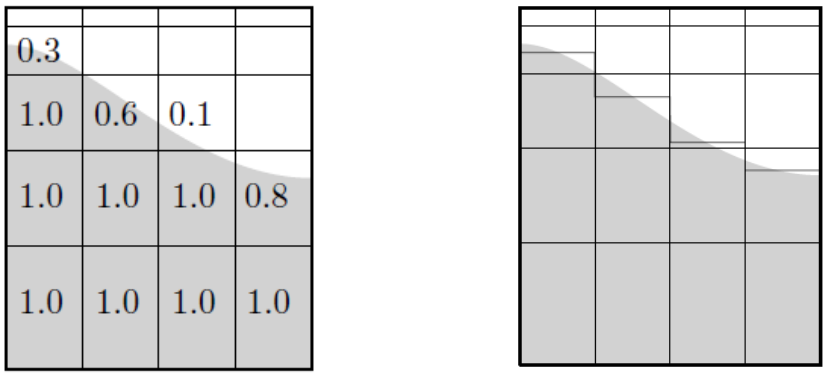

(a) VOF **(b)** SLIC

Figure 105: Reconstruction for Volume of fluid method. Images adopted from [24].

The simulation for Structure 8 was rerun with the SLIC-VOF method, and the results are visible in Figure 106. Unfortunately, this change had a negative effect on the results. Not only does the numerical error of fast droplets occur, resulting in the bullet effect as visible at time 4.25s, but also additional unexplained droplets occur throughout the domain. These droplets are not an effect of splashing or wave collision. As such, it is clear that it is another numerical error. Hence, the SLIC-VOF method is considered inadequate for this research.

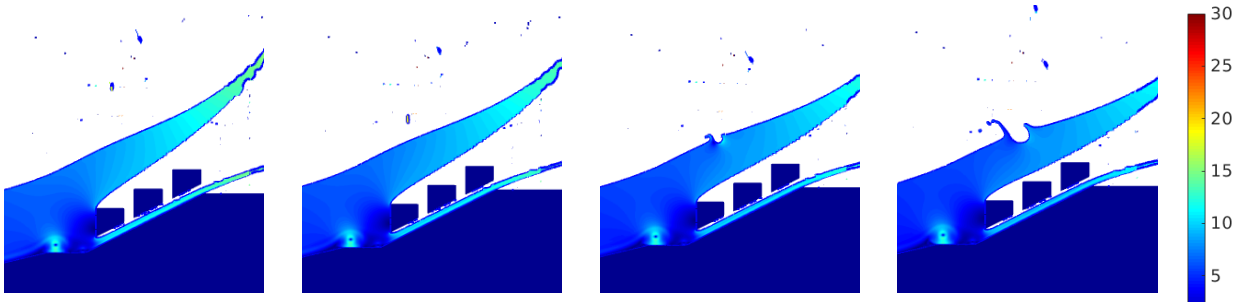

(a) time 3.95 **(b)** time 4.05 **(c)** time 4.15 **(d)** time 4.25

Figure 106: Rerun of the simulation for Structure 8, using a SLIC-VOF method.

Furthermore, different advection and reconstruction methods of PLIC-VOF were considered. A reader interested in the theory behind the alternative methods is referred to [12]. Certain combinations seemed to improve the solution, while others were not successful. For example, when the Least Square Gradient by Rider and Kothe was used with the Sussmann-Puckett advection technique, ComFLOW displayed many warnings. As such, the simulation using these methods was not completed.

Alternatively, two other reconstruction techniques were considered with the use of MACHO's advection method, namely the mixed Youngs-Centered (MYC) method and the Efficient least squares interface reconstruction algorithm (ELVIRA). The corresponding simulations did not appear to undergo any major numerical errors. There were no droplets near the wave, and as such the 'bullet' error was not observed. However, further research on the influence of the reconstruction methods on the droplet dynamic is advised.

To minimize the modifications of the settings between different simulation, the extended grid approach was used to reduce the numerical errors. Therefore, the same free-surface methods are used and the only difference is in the stretching of the outer local refinement zone.

8 Discussion and conclusion

In everyday life, one may forget about the dangers of nature or neglect the importance of transpiring environmental changes. However, the rising sea levels in combination with severe weather conditions greatly increase the risk of floods. This type of natural disaster is a serious threat, especially for countries with a geographical location like the Netherlands. In order to guard the safety of people, it is of great importance to study and improve the coastal defenses. For that reason, this project is on the topic of dikes, and more specifically on the efficiency of different designs of the roughness elements placed on a dike.

The computational tool used for the modeling of the coastal dynamics is ComFLOW. This software has been developed at the University of Groningen. The mathematical and numerical theory used in ComFLOW is explained in detail in Section 2. The optimal simulation settings have been found through experimentation and study of occurring numerical errors, as explained in Section 7.

Furthermore, to ensure the understanding of the coastal dynamics, a detailed explanation of wave phenomena and mathematical theory behind its modeling is given in Section 3. Through the study of statistical data, a wave event of height $8.5m$ is chosen for the numerical simulations. According to the data, such an event has a probability of occurring in the Netherlands once every 100 years. In addition, Section 4 is dedicated to the general design of coastal dikes and its components. Main focus is given towards different settings of roughness elements and a short explanation of more modern designs.

The simulation setup is discussed in Section 5. Firstly, the design of the domain is considered, alongside the methods of data gathering used in the simulations. Then the choice of the computational mesh is justified. The biggest challenge has been ensuring a high accuracy of the results, while minimizing the simulation time. An adequate setting has been found and its precision has been verified through comparison with a more detailed simulation.

In order to determine the efficiency of various roughness elements through numerical simulations, a few components are considered. The most important criterion is the level of overtopping, which is the amount of water passing through the structure onto the dike and eventually over the dike. Secondly the hydrodynamic forces acting on the roughness elements are studied. The velocity of the fluid passing through monitor points is also considered. And finally, the collision dynamics of the wave with the structure are analyzed.

Different characteristics of the roughness elements are researched, in order to determine their effect on the overall efficiency of the design. The studied properties are their size, slope, height, width and location on the slope. For the simulations, the designs are constructed to enhance the turbulent flow and reverse the trajectory of the incoming wave. The final designs have proven very efficient. For a smooth dike with no blocks present, the overtopping during the time of the simulation has almost reached $14m^3$. However, with the inclusion of the final roughness elements, this value has been reduced to less than $2.75m^3$. This implies an improvement by approximately a factor of 5.

Many further modifications can be applied to the considered coastal dike. However, due to the limited time of the project, this is not possible. A property of the roughness elements that could be enhanced is the redirection of the incoming wave. From the considered designs only a part of the wave has been influenced by the last block on the upper seaward slope. Hence, further analysis regarding the redirection of the wave is recommended.

Furthermore, this study has been limited to two dimensional simulations. Because of that many

designs are properties have been simplified, or modified to imitate the $3D$ reality. Considering the designs in three dimensions would allow for a more realistic representation of the roughness elements. This could vastly improve the accuracy of the simulations, but also require significant computer power.

On the other hand, conducting real life experiments, to be used for comparison, could be used to determine the performance of the ComFLOW software, or to find the optimal settings for certain simulations.

To conclude, in this project an initial study of the roughness elements on coastal dikes has been conducted. An effective design has been found, that reduced the amount of overtopping by approximately a factor of 5. This research shows how the ComFLOW software can be use to simulate complex collision dynamics of a wave running up a coastal dike. There is a vast area for future research to improve the design of roughness elements, or different components of the coastal dikes. This topic is of great importance, due to the rising risk of floods and consequences of such events.

References

[1] E. U. S. E. P. Agency. Climate change indicators: Weather and climate. Available online: https://www.epa.gov/climate-indicators/weather-climate, 2025. Accessed on 18 February 2025.

[2] P. N. E. A. Agency. Low probabilities - large consequences. reducing the vulnerability of the dutch population to floods. Available online: https://themasites.pbl.nl/o/flood-risks/, n.d. Accessed on 18 February 2025.

[3] Z. Ankers. The 1953 flood disaster. Available online: https://www.zeeuwseankers.nl/en/stories/the-1953-flood-disaster, n.d. Accessed on 18 February 2025.

[4] H. Bandringa. Immersed boundary methods. 08 2010.

[5] X. Chang, I. Akkerman, R. H. M. Huijsmans, and A. E. P. Veldman. Generating and absorbing boundary conditions for combined wave-current simulations. Paper presented at The 12th International Conference on Hydrodynamics, Egmond aan Zee, Netherlands., 2016.

[6] Y. Cheny and O. Botella. The ls-stag method: A new immersed boundary/level-set method for the computation of incompressible viscous flows in complex moving geometries with good conservation properties. *Journal of Computational Physics*, 229(4):1043–1076, 2010.

[7] M. College. Oceanography 101. Available online: https://batch.libretexts.org/print/Finished/geo-9666/Full.pdf?view=true, 2023. Accessed on 01 March 2025.

[8] Deltares. Sea level rise on the dutch coast has increased. Available online: https://www.deltares.nl/en/news/sea-level-rise-on-the-dutch-coast-has-increased, 2023. Accessed on 18 February 2025.

[9] K. Duncan Seraphin, J. Philippoff, F. M. Pottenger, L. Kaupp, M. H. Lurie, D. Lin, and E. Baumgartner. Exploring our fluid earth: Wave and wave properties. Available online: https://manoa.hawaii.edu/exploringourfluidearth/physical/waves/wave-and-wave-properties, n.d. Accessed on 02 March 2025.

[10] K. Duncan Seraphin, J. Philippoff, F. M. Pottenger, L. Kaupp, M. H. Lurie, D. Lin, and E. Baumgartner. Exploring our fluid earth: Wave energy and wave changes with depth. Available online: https://manoa.hawaii.edu/exploringourfluidearth/physical/waves/wave-energy-and-wave-changes-depth, n.d. Accessed on 01 March 2025.

[11] DutchNews. Inburgering with dutch news: key facts about the great flood of 1953. Available online https://www.dutchnews.nl/2023/01/inburgering-with-dutch-news-key-facts-about-the-great-flood-of-1953/, 2023. Accessed on 18 February 2025.

[12] B. Duz. *Wave Generation, Propagation and Absorption in CFD Simulations of Free Surface Flows*. PhD thesis, 09 2015.

[13] J. D. Fenton. A fifth-order stokes theory for steady waves. *Journal of Watenvay, Port, Coastal and Ocean Engineering*, 111:216–234, 1985.

[14] J. Garthwaite. Climate of chaos: Stanford researchers show why heat may make weather less predictable. Available online: https://news.stanford.edu/stories/2021/12/warming-makes-weather-less-predictable, 2021. Accessed on 18 February 2025.

[15] G. Lleshi. An investigation of wave run-up on a dike using comflow. University of Groningen, 2024.

[16] R. Luppes, P. van der Plas, B. Iwanowski, T. Bunnik, B. Duz, H. van der Heiden, R. Wemmenhove, P. Wellens, A. Veldman, T. HelmholtKleefsman, E. Loots, and J. Helder. *Manual ComFLOW Version 3.9.X/4.0*. University of Groningen, 2015.

[17] M. Rahman. Fundamentals concerning stokes waves. *Transactions on Engineering Sciences*, 9:289– 298, 1996.

[18] J. Van der Meer, N. Allsop, T. Bruce, J. De Rouck, A. Kortenhaus, T. Pullen, H. Schüttrumpf, P. Troch, and B. Zanuttigh. Eurotop, manual on wave overtopping of sea defences and related structures. an overtopping manual largely based on european research, but for worldwide application. Available online: `www.overtopping-manual.com`, 2018. Accessed on 18 February 2025.

[19] J. W. van der Meer. Technical report wave run-up and wave overtopping at dikes. *Technical Advisory Committee on Flood Defence*, 2002.

[20] H. A. van der Vorst. Bi-cgstab: A fast and smoothly converging variant of bi-cg for the solution of nonsymmetric linear systems. *SIAM Journal on Scientific and Statistical Computing*, 13(2):631–644, 1992.

[21] R. M. van Infrastructuur en Waterstaat. Watersnoodramp 1953. Available online: `https://www.rijkswaterstaat.nl/water/waterbeheer/bescherming-tegen-het-water/watersnoodramp-1953`, n.d. Accessed on 18 February 2025.

[22] A. Veldman. *Computational Fluid Dynamics (Lecture Notes)*. University of Groningen, 2012.

[23] N. A. via Wikimedia Commons. Watersnood 1953 rilland. Available online: `https://commons.wikimedia.org/wiki/File:Watersnood_1953_Rilland,_Bestanddeelnr_059-1219.jpg`, 1953. Accessed on 18 February 2025.

[24] P. Wellens. Wave simulation in truncated domains for offshore applications. 01 2012.

[25] F. Wubs. *Numerical Bifurcation Analsysis of Large Scale Systems (Lecture Notes)*. University of Groningen, 2009.

Appendix A

comflow.in

```
--@v312-----------------------------------------------------------------
-- Title ------------------------------------------------------------
Wave RunUp On Dike
---------------------------------------------------------------------
slosh   mvbd     twph   nproc
1       0        0      4
---------------------------------------------------------------------
-- domain definition ------------------------------------------------
xmin    xmax    ymin    ymax    zmin    zmax
-10.0     70.0    -0.50   0.50    -10.0   15.0
---------------------------------------------------------------------
-- green water parameters -------------------------------------------
grnwtr
0
---------------------------------------------------------------------
high    low     length
0.0     0.0     0.0
---------------------------------------------------------------------
width   a       b
0.0     0.0     0.0
---------------------------------------------------------------------
-- definition initial liquid configuration --------------------------
liqcnf lqxmin  lqxmax  lqymin  lqymax  lqzmin  lqzmax
1      -10.0     70.0    -0.50   0.50    -10.0   15.0
---------------------------------------------------------------------
-- definition of incoming wave --------------------------------------
wave  wvstart  period   wheight  xcrest  waterd  ramp
5     1        7.5     8.5     0       10.0    1       10     0.0  40.0
ramp  val1  val2
0     0.0   0.0
---------------------------------------------------------------------
-- definition of in- and outflow boundaries -------------------------
nrio
2
i/o     plane   xmin    xmax    ymin    ymax    zmin    zmax
11      1       -10.00    -10.00    -0.50   0.50    -10.00  15.00
11      1      70.00   70.00    -0.50   0.50    -10.00  15.00
---------------------------------------------------------------------
-- partial slip -----------------------------------------------------
pscnf psl
0 0.0
---------------------------------------------------------------------
-- absorbing boundary condition -------------------------------------
bcl    bcr   gabc   a0   a1   b1   kh1   kh2~   alpha1   alpha2~
1      1     -2     0.0  0.0  0.0  0.0   0.0    0.0      0.0
---------------------------------------------------------------------
-- definition of numerical beach in positive x-direction ------------
numbch  dampto0       0       0.05    10
---------------------------------------------------------------------
-- physical parameters ----------------------------------------------
rho1    rho2    mu1     mu2     sigma   theta  patm   gamma
1.0e3   1.0     1.0e-3  1.71e-5 0.0     130.0  1.0e5  1.4
---------------------------------------------------------------------
```

```
-- grid parameters ------------------------------------------------
griddef
2
imax    jmax    kmax    xc      yc      zc      sx      sy      sz
<!-- grid is specified in grid.cfi -->
-------------------------------------------------------------------
-- numerical parameters -----------------------------------------
eps     omega   itmax   alpha   feab0  feab1  feab2   nrintp  fslinext
1.0E-5  1.0     100000  1.0     0.0    1.5    -0.5    3       1
-------------------------------------------------------------------
-- numerical parameters two-phase flow --------------------------------
solver extrap  restol  imptol  upwind  imprel  irhoav  itscr droptol~ droptolbc~
5      0       1.0E-7  1.0E-3  2       1.0     1       0 1e-3 1e-6
-------------------------------------------------------------------
-- time parameters/cfl number -----------------------------------------
dt      tmax    dtmax   cfl     cflmin  cflmax  divl
.01     4.3    0.1     1       0.2    0.5     0
-------------------------------------------------------------------
-- free surface methods -----------------------------------------------
vofmth   vofcor  divl recon~ advect~
2        2       0 1 2
-------------------------------------------------------------------
-- gravitation --------------------------------------------------------
gravx   gravy   gravz   ginrt   finrt
0.0     0.0     -9.81   0       0
-------------------------------------------------------------------
-- motion of coordinate system ----------------------------------------
motionframe
0
amplx   freqx   amply   freqy   amplz   freqz
0.0     0.0     0.0     0.0     0.0     0.0
-------------------------------------------------------------------
omex    omey    omez    x0      y0      z0
0.0     0.0     0.0     0.0     0.0     0.0
-------------------------------------------------------------------
-- autosave -----------------------------------------------------------
load    nsave
0       2
-------------------------------------------------------------------
-- post-processing: snapshots/screen print/center of mass --------------
npm2d   npm3d   compr   nprnt   ntcom
86      0       0       86     0
-------------------------------------------------------------------
npmslic nyz     nxz     nxy
0       0       0       0
planeyz
planexz
planexy
-------------------------------------------------------------------
-- directory name for snapshots ---------------------------------------
pathname snapshot data:
data/
-------------------------------------------------------------------
-- fill boxes, force boxes and flux boxes-------------------------------
nfillb  ntfill
1       2000
xl      xr      yl      yr      zl      zr
52.0    70.0    0.0     0.0     0.0    15.0
-------------------------------------------------------------------
```

```
nfrcb   ntfrc
1       2000
xl      xr      yl      yr      zl      zr      mv meth
42.0    52.0    0.0     0.0     -1.0    5.0     0  1
------------------------------------------------------------------------
nfluxb  ntflux
1       2000
xl      xr      yl      yr      zl      zr
54.0 55.0 0.0 0.0 0.0 7.0
------------------------------------------------------------------------
nrelwh  ntrelwh
0       0
xl      xr      yl      yr      zl      zr
------------------------------------------------------------------------
-- stream line/particle path ------------------------------------------
npartp  npartl  npartc  ntpart
0       0       0       100
xpt     ypt     zpt     tstrt                           <- points
xl      xr      yl      yr      zl      zr      tstrt   <- lines
xc      yc      zc      radius  orient  tstrt           <- circles
------------------------------------------------------------------------
-- monitor points -----------------------------------------------------
nmntrp  nmntrl  nmntrc  ntmntr
3       0       0       400
xpt     ypt     zpt     mvp                             <- points
44.0 0.0 0.25 0
47.0 0.0 1.75 0
50.5 0.0 3.25 0
xl      xr      yl      yr      zl      zr      mvl     <- lines
xc      yc      zc      radius  orient                  <- circles
------------------------------------------------------------------------
-- special boxes ------------------------------------------------------
nrboxes tstart sbuvw
0       0.0    0
xmin    xmax    ymin    ymax    zmin    zmax
------------------------------------------------------------------------
```

Appendix B

grid.cfi

```
<?xml version="1.0" encoding="utf-8"?>
<comflow version="3.9">

<!--============================================
==== Grid
============================================-->
   <grid>
      <dimension>1200 1 350</dimension>
       <stretch>1.0011 1.0 1.005</stretch>
      <center>50.0 0.0 1.5</center>

      <!-- refinement ratios -->
      <refinement>2 2 2</refinement>

      <!-- coarse base grid -->
      <subgrid level="0" everywhere="1"/>
      <subgrid level="1">  20.0 52.5 0.0 0.0 -5.0 13.5 </subgrid>
<subgrid level="2">  42.0 51.0 0.0 0.0 -1.0 7.0 </subgrid>

      </grid>

</comflow>
```

Appendix C

geometry.in

```
11  0  0
44.0    0.0
50.0    0.0
50.0    3.0
12 0 0
50.0 0.0
70.0 0.0
70.0 3.0
50.0 3.0
12  0  0
42.0   -20.0
70.0   -20.0
70.0    0.0
42.0    0.0
11  0  0
0.0 -10.0
42.0 -10.0
42.0 0.0
12  0  0
0.0 -20.0
42.0 -20.0
42.0 -10.0
0.0 -10.0
13  0  0
0.2 -9.2
4.32 1.7
13  0  0
1.1 -10.0
5.76 2.08
13  0  0
5.23 -9.5
7.3 1.43
13  0  0
12.21 -8.11
4.3 1.25
13  0  0
31.1 -4.23
2.8 1.67
13  0  0
22.6 -5.72
5.62 1.54
13  0  0
15.3 -7.4
2.6 1.38
13  0  0
12.73 -7.65
4.1 0.78
13  0  0
16.71 -6.3
2.03 1.23
13  0  0
27.8 -4.9
3.24 1.64
```

```
13  0  0
25.42 -5.2
7.64 0.91
13  0  0
7.23 -8.04
1.3 0.43
13  0  0
17.54 -6.64
1.6 0.7
13  0  0
25.6 -5.6
2.3 0.89
13  0  0
28.3 -3.65
1.23 0.54
13  0  0
0.0 -9.5
4.3 1.7
13  0  0
-5.0 -9.2
3.4 1.23
13  0  0
-8.6 -9.56
6.32 1.6
13  0  0
-11.1 -8.9
4.2 1.24
13  0  0
-15.7 -9.3
6.3 0.76
13  0  0
-21.7 -9.82
6.43 0.69
13  0  0
-27.3 -9.4
7.21 0.54
12  0  0
44.5 0.75
45.5 1.25
45.5 2.0
44.5 1.5
12  0  0
48.5 2.75
49.5 3.25
49.5 4.5
48.5 4.5
12  1  0
44.5 1.0
45.5 1.5
45.5 1.75
44.5 1.25
13  1  0
48.5 4.0
0.7 0.6
11  1  0
48.5 4.0
48.5 2.75
49.2 3.8
```